

# BSM Studies Using Long-baseline Neutrino Experiment

Barnali Brahma

A Thesis Submitted to  
Indian Institute of Technology Hyderabad  
In Partial Fulfillment of the Requirements for  
The Degree of Doctor of Philosophy



भारतीय प्रौद्योगिकी संस्थान हैदराबाद  
Indian Institute of Technology Hyderabad

Department of Physics

April 2024

© 2024 by Barnali Brahma

All rights reserved

# Declaration

I declare that this written submission represents my ideas in my own words, and where ideas or words of others have been included, I have adequately cited and referenced the original sources. I also declare that I have adhered to all principles of academic honesty and integrity and have not misrepresented or fabricated or falsified any idea/data/fact/source in my submission. I understand that any violation of the above will be a cause for disciplinary action by the Institute and can also evoke penal action from the sources that have thus not been properly cited, or from whom proper permission has not been taken when needed.



---

(Signature)

**Barnali Brahma**

---

(Name)

**PH19RESCH11001**

---

(Roll No.)

# Approval Sheet

This thesis entitled **BSM Studies Using Long-baseline Neutrino Experiment** by Barnali Brahma is approved for the degree of Doctor of Philosophy from IIT Hyderabad.

---

(Prof. External) Examiner  
Dept. of Some Eng  
IIT

---

(Prof. Internal) Internal Examiner  
Dept. Some Eng  
IIT

---

(Prof. Anjan Giri) Adviser  
Dept. of Physics

---

(Dr. Alexander I. Himmel) Co-Adviser  
Fermi National Accelerator Laboratory

---

(Prof. Examiner) Chairman  
Dept. of Some Eng  
IIT

# Acknowledgements

I want to express my heartfelt gratitude to all the people who played significant roles in my Ph.D journey, and this thesis would remain incomplete without acknowledging them. First and foremost, I thank my academic advisor, Professor Anjan K. Giri, for accepting me into his group and providing me with an opportunity to work in NOvA collaboration. During my tenure, he contributed to a rewarding research experience by giving me intellectual freedom in my work, engaging me in new ideas, and demanding a high quality of work in all of my endeavors. In order to achieve my goal, he has always inspired me and steered me in the right direction. It was a privilege to work under his guidance as his student.

I also extend my heartfelt gratitude to my Ph.D co-advisor, Dr. Alexander I. Himmel, Fermilab, USA, for his continuous guidance and dedicated efforts to significantly enhance the quality of my research work. I greatly appreciate the insightful discussions during our regular weekly meeting at Fermilab. His valuable suggestions and feedback have been instrumental in guiding me and propelling my progress further. I want to thank him for his persistent help, particularly when I encountered technical challenges. I am truly thankful for taking the time out of his hectic schedule to review and provide input on the progress of my analysis work. His expertise, assistance, and mentorship have been pivotal to successfully completing my analysis work and thesis.

I especially want to thank Dr. Jonathan M. Paley for his constant support and for being my point of contact here at Fermilab. I owe him a great deal for his unwavering assistance whenever I needed it, no matter what time of day it is.

Additionally, I would like to thank my doctoral committee members, Professor Kanchana Venkatakrishnan, Dr. Narendra Sahu, and Dr. Bhuvanesh Ramakrishna, for their interest in my work and thought-provoking questions during the progress meetings.

I want to thank the NOvA Exotic Conveners, Dr. Matthew Strait, Dr. Alec Habig, and Dr. Oleg Samyorov, for their valuable comments and feedback throughout the analysis procedure. I would also like to thank my analysis review committee members, Dr. Denver W. Whittington, Dr. Louise Suter, and Dr. Jeffrey Kleykamp, for their insightful remarks during the review process, which helped us to improve our analysis. Every result described in this thesis was accomplished with the help and support of fellow labmates and collaborators Dr. Wei Mu and Tyler G. Horoho. We worked together on several different phases of the light-dark matter project, and without their efforts, my job would have undoubtedly been more difficult. I greatly benefited

from their keen scientific insight, a knack for solving seemingly intractable practical difficulties, and their ability to put complex ideas into simple terms. I would also like to acknowledge all the NOvA collaborators for their comments and suggestions during the NOvA collaboration meetings. I want to thank Fermilab, DOE, and DST India for their support and invitation to visit Fermilab and experience working in a world-class laboratory.

I appreciate Tom Weiber and Josh Barrow for allowing me to work on the Near Detector refurbishment work. This gave me immense pleasure to have a closer look and hands-on work with the NOvA detector.

I want to thank some of my collaborators, Lipsa, Bhumika, Amit, Shivam, Dan, Ishwar, Prachi, Sayeed, and Prameet, for having meaningful conversations on physics analysis and making my stay at Fermilab enjoyable. I also want to thank some of my friends (Lopa, Rashmi, Anuroopa, Gopika, and Sushree) for our cherished time together at IIT Hyderabad. I thank my master's and bachelor's friends and teachers at Utkal University and the Regional Institute of Education for their inspiration and enthusiasm towards building a career in research.

Finally, I express my deepest gratitude to my family for their love, care, and support throughout my life. To my parents, for their understanding and patience and for inculcating a positive attitude toward life. Without their support, I could never have come so far. My brother and childhood friends for their love and care towards me.

I am always grateful to the omnipresent Lord Jagannath and Lord Shiva for their countless blessings at every step of my life.

# Dedication

*“To my parents, brother, and family”.*

# Abstract

The standard model of particle physics cannot account for the various physical phenomena present in nature. For instance, the visible matter constitutes only about 5% of the whole universe, and the remaining content is believed to be dark matter and dark energy. Unfortunately, the standard model does not provide us with a good candidate for dark matter. The leading dark matter candidate is weakly interacting massive particles (WIMPs) having a mass of less than 1 GeV. We will require a broad, fixed target neutrino experiment to probe the vast parameter space for the light-dark matter particle. NOvA is a high luminosity long-baseline fixed-target accelerator neutrino experiment at Fermilab. It can provide a potentially exciting probe in searching for signatures of DM scattering with electrons in its near detectors. We aim to search for the MeV-scale dark matter particles that might be generated within the NuMI beam and produce detectable electron scattering signals in the NOvA Near Detector.

Not only in the dark matter sector, the standard model cannot explain the neutrino mass and mixings. The neutrino propagation in matter can be affected by non-standard interactions (NSI), which is beyond the standard model phenomena. The constraints coming from the NSI sectors can affect the standard oscillation parameters like atmospheric mixing angle  $\theta_{23}$  and CP-phase  $\delta_{CP}$ .

# Contents

|  |           |
|--|-----------|
| List of Tables . . . . .                       | x         |
| List of Figures . . . . .                      | xi        |
| List of Algorithms . . . . .                   | xvi       |
| Listings . . . . .                             | xvi       |
| <b>1 Introduction</b>                          | <b>1</b>  |
| 1.1 The Standard Model . . . . .               | 1         |
| 1.1.1 Bosons . . . . .                         | 1         |
| 1.1.2 Fermions . . . . .                       | 2         |
| 1.2 Open Questions in Standard Model . . . . . | 3         |
| 1.3 Neutrino Physics . . . . .                 | 4         |
| 1.4 Properties of Neutrinos . . . . .          | 6         |
| 1.4.1 Neutrino Flavors . . . . .               | 6         |
| 1.4.2 Neutrino interactions . . . . .          | 8         |
| 1.4.3 Sources of Neutrinos . . . . .           | 9         |
| 1.4.4 Solar Neutrino Problem . . . . .         | 10        |
| <b>2 Neutrino Formalism</b>                    | <b>12</b> |
| 2.0.1 Neutrino Oscillation in Matter . . . . . | 15        |
| 2.0.2 Beyond the Standard Model . . . . .      | 18        |
| <b>3 NOvA Experiment</b>                       | <b>22</b> |
| 3.1 NuMI Beam . . . . .                        | 23        |
| 3.1.1 Fermilab Accelerator Complex . . . . .   | 23        |
| 3.1.2 NuMI Beamline . . . . .                  | 23        |
| 3.1.3 Off-Axis Detectors . . . . .             | 25        |
| 3.1.4 NOvA Detectors . . . . .                 | 26        |
| 3.2 NOvA Data Acquisition System . . . . .     | 30        |

|          |   |           |
|----------|---|-----------|
| <b>4</b> | <b>NOvA Simulation and Reconstruction</b>   | <b>33</b> |
| 4.0.1    | Neutrino Interactions . . . . .   | 34        |
| 4.0.2    | Particle Propagation . . . . .  | 35        |
| 4.0.3    | Reconstruction . . . . .  | 36        |
| <b>5</b> | <b>Light-Dark Matter Analysis in NOvA Near Detector</b>                             | <b>39</b> |
| 5.1      | Analysis Overview . . . . .   | 39        |
| 5.1.1    | Vector Portal Model . . . . .   | 40        |
| 5.1.2    | DM Production and Detection . . . . .   | 41        |
| 5.1.3    | Dark Matter Signal Identification . . . . .   | 43        |
| 5.1.4    | Data Analysis . . . . .   | 44        |
| 5.1.5    | Simulation of Signal Events . . . . .   | 47        |
| 5.1.6    | Single Electron Event Selections and Cuts . . . . .                                 | 53        |
| 5.1.7    | Systematic Uncertainties . . . . .  | 56        |
| 5.1.8    | Results . . . . .   | 61        |
| <b>6</b> | <b>Non-Standard Interactions in Long-baseline Neutrino Experiments</b>              | <b>65</b> |
| 6.1      | Analysis Overview . . . . .   | 65        |
| 6.1.1    | Parameterization of NSI . . . . .   | 66        |
| 6.1.2    | Formalism . . . . .   | 67        |
| 6.1.3    | Simulation Software . . . . .   | 68        |
| 6.1.4    | Analysis Details . . . . .  | 69        |
| 6.1.5    | CP Asymmetry and Mass Hierarchy . . . . .   | 75        |
| <b>7</b> | <b>Dual Non-Standard Interactions Effects in Long-baseline Neutrino Experiments</b> | <b>79</b> |
| 7.1      | Analysis Overview . . . . .   | 79        |
| 7.1.1    | Formalism . . . . .   | 79        |
| 7.2      | Analysis details and results: . . . . .   | 80        |
| 7.2.1    | Effect of dual NSI Parameters on Oscillation Probability . . . . .                  | 87        |
| 7.3      | CP Violation Sensitivity . . . . .  | 87        |
| 7.3.1    | CP Asymmetry . . . . .  | 88        |
| <b>8</b> | <b>Conclusion and Future Directions</b>   | <b>93</b> |
| 8.1      | Light-Dark Matter Analysis . . . . .  | 93        |
| 8.2      | Non-Standard Neutrino Interactions . . . . .  | 94        |
|          | <b>References</b>   | <b>97</b> |

# List of Tables

|     |   |    |
|-----|---|----|
| 1.1 | Fundamental Forces in Standard Model . . . . .  | 2  |
| 1.2 | The Fundamental Fermions . . . . .  | 3  |
| 3.1 | Composition of the liquid scintillator . . . . .  | 30 |
| 5.1 | Parameters used for light DM production simulation in BdNMC software.   | 49 |
| 5.2 | Cut flow for MC $\chi$ - $e$ signal, $\nu$ - $e$ background and nominal NuMI back-<br>ground events. . . . .  | 55 |
| 5.3 | Impacts of the systematic uncertainties on the 90% confidence level<br>sensitivity measurement (%) as a function of DM mass $m_\chi$ . Note<br>that this table shows that the impact from Flux and Cross Section<br>uncertainties are almost identical and indistinguishable. . . . . | 61 |
| 6.1 | From allowed region plots, the best-fit points are listed here. The<br>best-fit points are picked up corresponding to the minimum $\chi^2$ value.<br>These values are also included in the below table. . . . .   | 70 |
| 7.1 | From allowed region plots, the best-fit points are listed here. The<br>best-fit points are picked up corresponding to the minimum $\chi^2$ value.<br>These values are also included in the below table. . . . .   | 83 |
| 7.2 | The average CP asymmetry in the presence of vacuum, matter, and<br>dual NSI scenario for the DUNE energy window (2 GeV - 3 GeV) and<br>T2HK energy window (0.5 GeV - 1 GeV) are included in the table below.  | 90 |
| 8.1 | The best-fit points are listed here. The best-fit points are picked up<br>corresponding to the minimum $\chi^2$ value. . . . .  | 95 |
| 8.2 | The best-fit points are picked up corresponding to the minimum $\chi^2$<br>value for the simultaneous scanning of non-standard parameters: $\epsilon_{e\mu}$<br>and $\epsilon_{e\tau}$ . . . . .  | 95 |

# List of Figures

|      |  |    |
|------|--|----|
| 1.1  | A schematic Diagram of the Standard Model . . . . .  | 4  |
| 1.2  | Electron energy spectrum for beta decay of carbon-14 . . . . .   | 6  |
| 2.1  | A schematic representation of the composition of the Universe . . . . .  | 20 |
| 3.1  | The NOvA experiment layout shows that the near detector is located at Fermilab while the Far Detector is placed 810 km away at Ash River, Minnesota . . . . .  | 22 |
| 3.2  | The Schematics of Fermilab Accelerator Complex. . . . .  | 24 |
| 3.3  | A schematic view of the NuMI beamline . . . . .  | 25 |
| 3.4  | Near Detector on the left and Far Detector on the right . . . . .  | 26 |
| 3.5  | The Neutrino Flux and energy distribution with respect to pion of Energy $E_\pi$ for various angles ( $\theta$ ) of the detector placement from the beam axis. The red curve in the picture shows the off-axis angle chosen for both NOvA detectors to optimize the sensitivity for the oscillation of $\nu_\mu$ to an $\nu_e$ . . . . . | 27 |
| 3.6  | Neutrino energy spectra that the NOvA Far Detector would see for various off-axis angles. . . . .  | 27 |
| 3.7  | A schematic view of the Near Detector . . . . .  | 28 |
| 3.8  | A schematic view of the Far Detector . . . . .   | 29 |
| 3.9  | Wavelength-shifting fiber collects and transports light to Avalanche photodiode . . . . .  | 30 |
| 3.10 | NOvA DAQ System . . . . .  | 32 |
| 4.1  | The major component of neutrino flux at FD (top) and ND (bottom) for FHC (left) and RHC (right) mode. . . . .  | 35 |
| 4.2  | Neutrino interactions showing a $\nu_\mu$ CC interaction (top panel), $\nu_e$ CC interaction (middle panel), and NC interaction (bottom panel). . . . .  | 37 |
| 4.3  | A sample Event Display showing that color denotes deposited charges.]  | 38 |

|      |   |    |
|------|---|----|
| 5.1  | <b>Left:</b> direct production of vector mediator V and DM; <b>Right:</b> DM-matter interaction via the reversed process. . . . .   | 42 |
| 5.2  | Signal and background pattern in $E\theta^2$ space. Only the $\nu$ - $e$ background is plotted in this figure. In the high $E\theta^2$ region, other beam-related backgrounds start to dominate the total background, as shown in FIG. 5.3 . . . . .  | 44 |
| 5.3  | Fit sample. When producing the fake data, the parameters are configured as $a = 0, b = 1.05, c = 0.95$ . For the fit, the DM mass is fixed as $m_\chi = 8$ MeV. . . . .   | 46 |
| 5.4  | Beam related background: neutrino on nucleus. . . . .   | 47 |
| 5.5  | This figure shows the number of single electrons (on the left), the mean scattering energy, and angle (the two on the right) might be produced by DM particles with different masses. These plots are generated using parameters configured as: $\alpha_D = 0.5, \epsilon^4\alpha_D = 5 \times 10^{-13}, m_\chi/m_V = 1/3$ and POT = $1.0 \times 10^{21}$ . . . . .         | 50 |
| 5.6  | The figures show the recoil energy and scattering angle spectra of the electrons scattered by DM particles with mass 5, 10, 50, 100, and 450 MeV. . . . .   | 50 |
| 5.7  | The generic energy distribution of the single electrons scattered by DM particles (left) and the correlation between the electrons' recoil energy and the scattering angle (right). The green curve in the left figure is the so-called generic energy distribution. The small right figure shows the scattering angles' distribution at 1 GeV recoil energy slice. . . . . | 51 |
| 5.8  | The correlation between the recoil energy and the scattering angle does not depend on the mass of the DM particles. . . . .   | 51 |
| 5.9  | The bin-by-bin ratio between the the two histograms: the generic energy distribution (green curve in the left figure of FIG. 5.7) and the specific energy distribution for a specific DM mass (curve with corresponding color). . . . .   | 52 |
| 5.10 | A comparison of the $E\theta^2$ spectra between samples reweighted from the generic sample and the "true" distributions generated directly by BdNMC for four different DM mass points (5, 10, 20, 100 MeV). . . . .   | 52 |
| 5.11 | Sample distribution of the variables used for event selection for DM masses 5, 10, and 100 MeV along with $\nu$ -on- $e$ and Neutrino on the nucleus. . . . .   | 56 |

|      |  |    |
|------|--|----|
| 5.12 | Sample plot showing FOMs for generic samples (top 4) and specific samples (bottom 4). We have used these plots to show that similar cuts work for both generic and specific DM mass samples. . . . .   | 57 |
| 5.13 | Selection efficiency of angular distribution for all the sample DM masses.   | 58 |
| 5.14 | The $E\theta^2$ spectrum shifts due to the systematic uncertainties of near detector for beam-related background events. . . . .   | 60 |
| 5.15 | The $E\theta^2$ spectrum shifts due to the systematic uncertainties of near detector for $\nu$ -on-e events. . . . .   | 61 |
| 5.16 | The $E\theta^2$ spectrum shifts due to the systematic uncertainties of near detector for 10 MeV LDM signal (top left), 100 MeV LDM signal (top right), $\nu$ -e scattering background events (bottom left), and beam-related background events (bottom right). . . . .   | 62 |
| 5.17 | . . . . .  | 63 |
| 6.1  | Allowed regions for $\epsilon_{e\mu}$ and the CP phase (left); $\epsilon_{e\mu}$ and phase $\phi_{e\mu}$ (right) determined by the combination of T2K and NO $\nu$ A for NO (top panel) and IO (bottom panel). The contours are drawn at the 68% and 90% C.L. for 2 d.o.f. . . . .   | 70 |
| 6.2  | Allowed regions for coupling $\epsilon_{e\tau}$ and CP phase (left); $\epsilon_{e\tau}$ and phase $\phi_{e\tau}$ (right) determined by the combination of T2K and NO $\nu$ A for NO. The contours are drawn at the 68% and 90% C.L. for 2 d.o.f. . . . .   | 71 |
| 6.3  | Allowed regions determined separately by DUNE and T2HK for NO in the SM case (left panel) and with NSI in the $e - \mu$ sector (middle panel) and in the $e - \tau$ sector (right panel). In the middle panel, we have taken the NSI parameters at their best-fit values of NO $\nu$ A+T2K ( $ \epsilon_{e\mu}  = 0.1$ , $ \phi_{e\mu}  = 0.2\pi$ ). Similarly, in the right panel we have taken $ \epsilon_{e\tau}  = 0.1$ , $ \phi_{e\tau}  = 1.47\pi$ . The contours are drawn at the 90% and 95% C.L. for 2 d.o.f. . . . . | 72 |
| 6.4  | One-dimensional projections for the standard parameters $\theta_{23}$ (left) and $\delta_{CP}$ (right) for DUNE in the case of NO for SM (red dashed curves) and SM, along with NSI arising from the $e - \mu$ scenario (blue dashed curves). . . . .  | 73 |
| 6.5  | One-dimensional projections plots for the standard parameters $\theta_{23}$ (left) and $\delta_{CP}$ (right) for T2HK in the case of NO for SM (red dashed curves) and SM, along with NSI arising from the $e - \mu$ scenario (blue dashed curves). . . . .  | 73 |

|     |   |    |
|-----|---|----|
| 6.6 | Probability Plots for DUNE in SM (left) and SM+NSI scenario with NSI arising from $e - \mu$ sector (middle) and $e - \tau$ sector (right) for $\nu$ (top panel) and $\bar{\nu}$ (bottom panel) mode . . . . .   | 74 |
| 6.7 | Probability Plots for T2HK in SM (left) and SM+NSI scenario with NSI arising from $e - \mu$ sector (middle) and $e - \tau$ sector (right). . . . .  | 75 |
| 6.8 | CP discovery potential for DUNE (top panel) and T2HK (bottom panel) as a function of the true value of the leptonic CP phase for NO in SM scenario(left panel) and SM+NSI scenario (right panel). The bands represent the range in sensitivity obtained under the two different assumptions of $\theta_{23}$ value. . . . .   | 76 |
| 6.9 | CP asymmetry $A_{CP}$ versus energy [in GeV] in the presence of NSI arising from the $\epsilon_{e\mu}$ (top) and $\epsilon_{e\tau}$ (bottom) sector in case of DUNE (left) and T2HK (right) experimental setup. The colored yellow band indicates an energy band around 2.6 GeV for DUNE and 0.6 GeV for T2HK, which we use for illustration in this work. The star points at the obtained $A_{CP}$ value for the corresponding energy and is also mentioned within the brackets. . . . . | 78 |
| 7.1 | Allowed regions in the plane spanned by NSI coupling for $\epsilon_{e\mu}$ and $\epsilon_{e\tau}$ (left); $\phi_{e\mu}$ and phase $\phi_{e\tau}$ (right) determined by the combination of T2K and NO $\nu$ A for NO (top panel) and IO(bottom panel). The contours are drawn at the 68% and 90% C.L. for 2 d.o.f . . . . .  | 82 |
| 7.2 | Allowed regions determined separately by DUNE (top panel), T2HK (middle panel), and a combination of DUNE and T2HK (bottom panel) for NO in the SM case (left panel) and with dual NSI arising from $e - \mu$ and $e - \tau$ sector (right panel). The contours are drawn at the 90% and 95% C.L. for 2 d.o.f. . . . .  | 84 |
| 7.3 | One-dimensional projections of the standard parameters $\theta_{23}$ (left) and $\delta_{CP}$ (right) determined for DUNE in NO for SM (red dashed curves) and SM, along with the NSI scenario, arising simultaneously from the $e - \mu$ and $e - \tau$ sectors. (blue dashed curves). . . . .   | 85 |
| 7.4 | One-dimensional projections of the standard parameters $\delta_{CP}$ determined for T2HK in NO (left) and IO (right) scenario for SM (red dashed curves) and SM, along with the NSI scenario, arising simultaneously from the $e - \mu$ and $e - \tau$ sectors. (blue dashed curves). . . . .   | 85 |

|     |   |    |
|-----|---|----|
| 7.5 | One-dimensional projections of the standard parameters $\theta_{23}$ (left) and $\delta_{CP}$ (right) determined for DUNE+T2HK in NO for SM (red dashed curves) and SM, along with the NSI scenario, arising simultaneously from the $e - \mu$ and $e - \tau$ sectors. (blue dashed curves). . . . .  | 86 |
| 7.6 | Probability Plots for DUNE in SM (left) and SM+2NSI scenario with NSI arising from both $e - \mu$ sector and $e - \tau$ sector (right) for $\nu$ (top panel) and $\bar{\nu}$ (bottom panel) mode . . . . .  | 88 |
| 7.7 | Probability Plots for T2HK in SM (left) and SM+2NSI scenario with NSI arising from both $e - \mu$ sector and $e - \tau$ sector (right) for $\nu$ (top panel) and $\bar{\nu}$ (bottom panel) mode . . . . .  | 89 |
| 7.8 | CP discovery potential for DUNE (top panel), T2HK (middle panel), and DUNE+T2HK (bottom panel) as a function of the true value of the leptonic CP phase for NO in SM scenario(left panel) and SM+2NSI scenario (right panel). The bands represent the range in sensitivity obtained under the two different assumptions of $\theta_{23}$ value. . . . . | 91 |
| 7.9 | CP asymmetry $A_{CP}$ versus Energy [in GeV] plot for both NO and IO scenarios. In the above plots, we have included vacuum, SM with matter effects, and SM with the inclusion of NSI arising simultaneously from $\epsilon_{e\mu}$ and $\epsilon_{e\tau}$ in the T2HK and DUNE experimental setup . . . . .  | 92 |

# Listings

# Chapter 1

## Introduction

### 1.1 The Standard Model

Particle physics enhances our understanding of the ultimate constituents of matter and the laws governing their interactions. The standard model (SM) of particle physics [1, 2, 3, 4] establishes a theoretical framework that describes the elementary particle interaction at the most fundamental level. All the fundamental particles in nature can be divided into two categories: **bosons** and **fermions**. These fundamental particles can all be distinguished by their spin.

#### 1.1.1 Bosons

Bosons are the fundamental particles that have an integral spin in the units of Planck's constant. According to the standard model of particle physics, there are five elementary bosons:

- Four Vector gauge bosons with spin = 1. Photons ( $\gamma$ ), gluons (g),  $Z^0$  and  $W^\pm$  are the four-vector gauge bosons that act as force carriers. We have four fundamental forces present in our nature: strong force, electromagnetic force, weak force, and gravitational force.

Gluon: A bi-color massless vector boson responsible for the strong interactions of quarks and leptons inside the hadrons. Quantum electrodynamics (QED) can explain the electromagnetic interactions; the colorless and massless photons are the carriers of this interaction. The mediators for weak force are  $W^\pm$  and  $Z^0$  bosons. The Fermi constant represents the strength of weak interaction. Glashow, Salam, and Weinberg combine the electromagnetic and weak forces into the electroweak interaction, which in turn combines with the strong interaction to form a single unifying model called the Standard Model. The  $SU(3)_C \times SU(2)_L \times U(1)_Y$  gauge group represents the SM.

Here,  $SU(3)_C$  is for strong interaction where C stands for the color charge,  $SU(2)_L$  is for weak interaction, where L implies the coupling of  $W^\pm$ ,  $Z^0$  bosons with only left-handed fermions and  $U(1)_Y$  stands for the electromagnetic force with Y as the hypercharge.

- Tensor boson with spin = 2 called graviton. The weakest fundamental force is the gravitational force, which is believed to be Graviton. All attempts to incorporate this exceptional hypothetical gauge boson into the standard model have failed.
- Scalar Higgs boson with spin = 0. Higgs boson contributes to the phenomena of mass via the Higgs Mechanism, or in other words, it is responsible for the mass of the particles and interacts with them via the so-called Higgs mechanism.

Table 1.1: Fundamental Forces in Standard Model

| Forces          | Mediator     | Gauge Group | Range (in m)    | Coupling strength |
|-----------------|--------------|-------------|-----------------|-------------------|
| Strong          | gluons       | $SU(3)_C$   | $\leq 10^{-15}$ | $< 1$             |
| Weak            | $W^\pm, Z^0$ | $SU(2)_L$   | $10^{-18}$      | $10^{-6}$         |
| Electromagnetic | photons      | $U(1)_Y$    | $\infty$        | $1/137$           |
| Gravitational   | gravitons    |             | $\infty$        | $10^{-39}$        |

### 1.1.2 Fermions

Fermions are half-odd-integer spin particles that follow Fermi–Dirac statistics. These particles include all quarks and leptons, with no further substructure, and are composed of all the visible matter. Fermions differ from bosons as they obey Bose-Einstein statistics. As a result of the Pauli exclusion principle, only one Fermion can exist in a given quantum state at a given time. Suppose that the spatial probability distribution of several fermions is the same. In this case, at least one property of each Fermion, such as its spin, must be different.

The Standard Model recognizes two types of elementary fermions: quarks and leptons. There are six quarks (up, down, strange, charm, down, and up) and six leptons (electron, electron neutrino, muon, muon neutrino, tau, and tau neutrino) and their corresponding antiparticles.

Table 1.2: The Fundamental Fermions

| Particles | Flavors |           |            | Q/ e |
|-----------|---------|-----------|------------|------|
| leptons   | $e$     | $\mu$     | $\tau$     | -1   |
|           | $\nu_e$ | $\nu_\mu$ | $\nu_\tau$ | 0    |
| quarks    | u       | c         | t          | +2/3 |
|           | d       | s         | b          | -1/3 |

## Quarks

Quarks combine to form composite particles called hadrons, the most stable of which are protons and neutrons, the components of atomic nuclei. All commonly observed matter consists of up quarks, down quarks, and electrons. Due to a phenomenon known as color confinement, quarks can never be isolated. Quarks and gluons must clump together to form hadrons. The mesons (one quark, one antiquark) and the baryons (three quarks) are the two main types of hadrons. Quarks carry fractional charges of  $+\frac{2}{3}|e|$  or  $-\frac{1}{3}|e|$ . The quark type is denoted by a symbol:  $u$  for ‘up’,  $d$  for ‘down’,  $s$  for ‘strange’,  $c$  for ‘charm’,  $b$  for ‘bottom’, and  $t$  for ‘top’.

## Leptons

Similar to quarks, leptons may also be classified into six flavors. These flavors include charged leptons such as electron ( $e$ ), muon ( $\mu$ ), and tau ( $\tau$ ) and their equivalent neutral leptons, known as electron neutrino ( $\nu_e$ ), muon neutrino ( $\nu_\mu$ ), and tau neutrino ( $\nu_\tau$ ). Leptons have no color quantum number and are color singlets.

## 1.2 Open Questions in Standard Model

The standard model is not an ideal model. It has several open questions that are yet to be answered

- Baryonic Asymmetry of the Universe
- Nature of Dark Matter and Dark Energies
- Neutrino mass generation mechanism
- Violation of CP asymmetry in the leptonic sector
- Either Neutrino is Dirac or Majorana

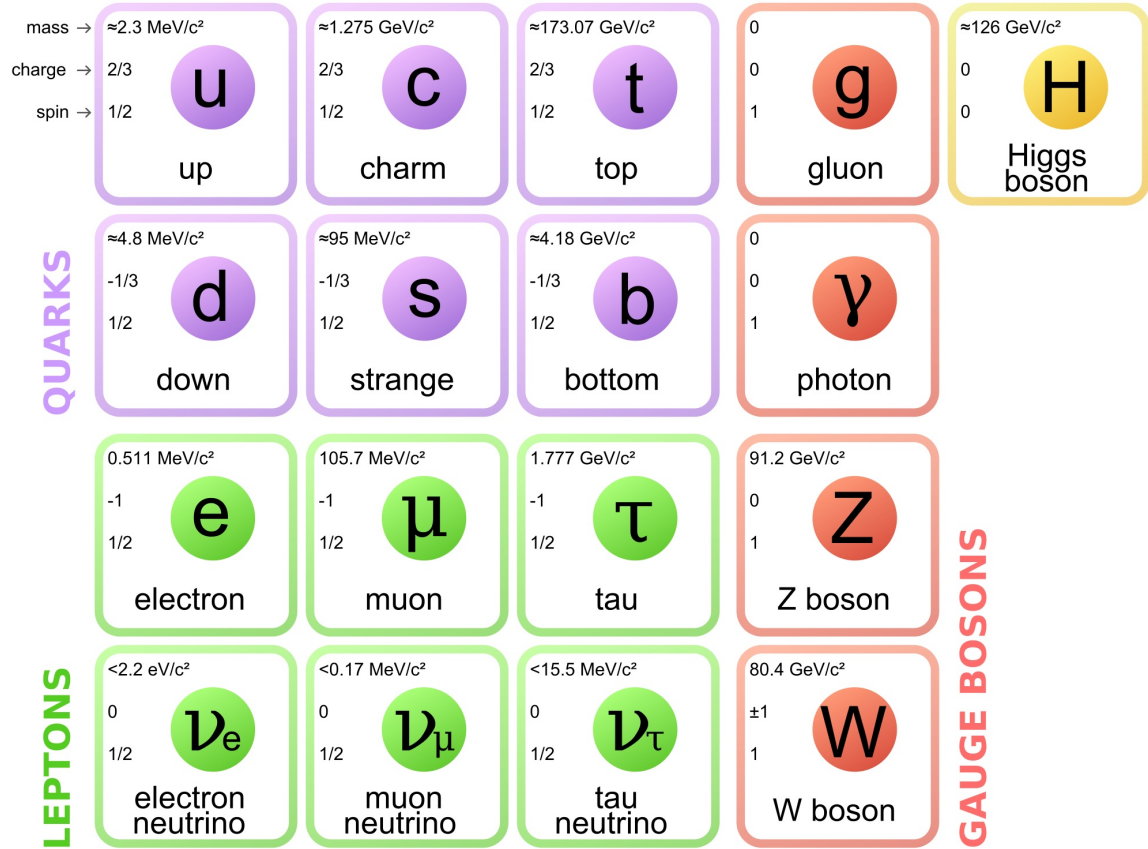


Figure 1.1: A schematic Diagram of the Standard Model

- The Neutrino mass hierarchy problem
- Proton Stability

The standard model extension was much needed at this hour to search for solutions to these open questions. Neutrinos, among all, possess most of the open questions and are an important motivation for exploring Physics beyond the Standard Model.

### 1.3 Neutrino Physics

Neutrinos are the most elusive and abundant particles to be present in the universe [5, 6, 7, 8, 9]. This elusive nature of neutrinos could be attributed to their negligible mass and weak interaction. Since the Pauli hypothesis, neutrinos have left us startled by behaving differently than the expectations of the current theory. Neutrinos are detected through a charged lepton produced via charged-current weak interactions [10]. Neutrinos also interact via weak neutral currents ( $Z^0$ ), which are flavor-independent. The standard model of particle physics assumes that there are three different flavors of neutrinos: electron neutrino

( $\nu_e$ ), muon neutrino ( $\nu_\mu$ ), and tau neutrino ( $\nu_\tau$ ). Many neutrino sources were used for the experimental study. Natural sources of neutrinos include the Sun ( $\nu_e$ ), supernova explosion (all flavors), cosmic phenomena, nuclear collisions of cosmic rays in the atmosphere ( $\nu_e$  and  $\nu_\mu$  and their antiparticles). Neutrino beams can also be produced at the proton accelerator facilities ( $\nu_\mu/\bar{\nu}_\mu$ ) and reactor facilities ( $\bar{\nu}_e$ )

## Brief History of Neutrinos

Three elementary particles were known around the 1920s: the positive particle proton, the neutral particle neutron, and the negative particle electron. Atoms were believed to be built out of these elementary particles. A nucleus inside the atoms having atomic number  $A$  and charge  $Z$  was considered to be made of  $A$  number of positive protons and  $A - Z$  number of negative electrons. However, a very severe problem came along with this model. The problems came into light with beta decay, a form of radioactive decay in which a nucleus of atomic number  $Z$  transforms to one of atomic number  $Z + 1$ , and an electron is emitted. Beta decay occurs because the daughter nucleus has less mass than the parent, so the decay is energetically favored. It was expected that the electron would carry off the difference in masses in the form of kinetic energy. However, it turned out that the electron always carried less energy than expected. Instead of all electrons having the same energy, there was a continuous distribution, as shown in Figure 1.2.

At that point in time, quantum mechanics was quite in its early stages of development. Initially, there were suggestions that energy conservation might not be possible at the atomic level. But the right direction was given by Wolfgang Pauli in December 1930 in his famous letter [11] as a *desperate remedy* to *Liebe Radioaktive Damen und herren*. He assumed that an unknown neutral particle exists inside the nucleus and is emitted together with the electrons in the beta decay [12, 13]. He proposed a light-neutral particle of spin 1/2 emitted alongside the electron in beta decay and proposed the name ‘neutron’. He wrote in his letter, “because of the ‘wrong’ statistics of the N- and Li-6 nuclei and the continuous beta spectrum, I have hit upon a desperate remedy to save the ‘exchange theorem’ of statistics and the law of conservation of energy. Namely, the possibility that in the nuclei there could exist electrically neutral particles, which I will call neutrons, that have spin 1/2 and obey the exclusion principle and that further differ from light quanta in that they do not travel with the velocity of light. The mass of the neutrons should be of the same order of magnitude as the electron mass and in any event not larger than 0.01 proton mass. - The continuous beta spectrum would then make sense with the assumption that in beta decay, in addition to the electron, a neutron is emitted such that the sum of the energies of neutron and electron is constant”. The proposed unknown particle could explain the continuous spectrum in the beta decay. In 1932, J. Chadwick discovered neutral particles [14] whose mass was similar

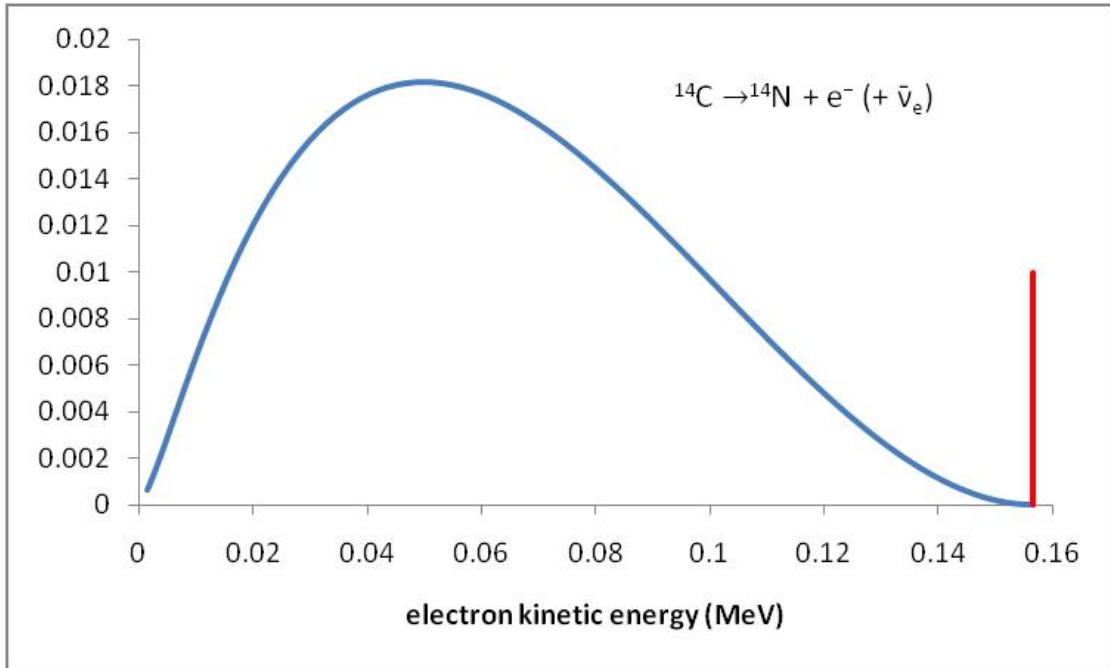


Figure 1.2: Electron energy spectrum for beta decay of carbon-14

to a proton. The name neutron was given to this particle, and Fermi, in 1934, renamed Pauli’s particle as neutrino. In 1956, 20 years after neutrino got its name, Frederick Reines and Clyde Cowan used the nuclear reactor by Davis. They succeeded in detecting neutrinos (to be more precise, the electron antineutrino) [15, 16, 17, 18]. The reaction was:

$$\bar{\nu}_e + p \rightarrow n + e^+$$

## 1.4 Properties of Neutrinos

### 1.4.1 Neutrino Flavors

The standard model of particle physics has three different neutrino flavors. Each neutrino completes a doublet with the corresponding charged leptons. A  $W^+$  gauge boson can couple to three different neutrino/charged-lepton pairs.

$$\begin{aligned}
W^+ &\rightarrow e^+ \nu_e, \\
&\rightarrow \mu^+ \nu_\mu, \\
&\rightarrow \tau^+ \nu_\tau.
\end{aligned}$$

Similarly, for the  $W^-$  gauge boson, we can have three different antineutrino/charged-lepton pairs.

$$\begin{aligned}
W^- &\rightarrow e^- \bar{\nu}_e, \\
&\rightarrow \mu^- \bar{\nu}_\mu, \\
&\rightarrow \tau^- \bar{\nu}_\tau.
\end{aligned}$$

## Electron Neutrinos

The unobserved neutral particle suggested by Pauli to resolve the beta decay problem had to be neutral to conserve electric charge, have a smaller mass, and spin 1/2 to conserve angular momentum.

$$n^0 \rightarrow p^+ + e^- + \bar{\nu}_e$$

Reines and Cowan utilized the nuclear reactor at Savannah River in South Carolina as an anti-neutrino source and a detector of water with dissolved cadmium chloride.

$$\bar{\nu}_e + n \rightarrow e^- + p$$

A positron was emitted in the reaction, and then the cadmium dissolved in the water deexcites with neutron capture and emission of a photon.

$$n + {}^{112}\text{Cd} \rightarrow {}^{113}\text{Cd} + \gamma$$

For the first time, the anti-electron neutrino ( $\bar{\nu}_e$ ) was detected in this experiment, and Reines and Cowan won the Nobel Prize in 1995.

## Muon Neutrinos

Pion and muon decay produced the muon type of neutrinos.

$$\pi^+ \rightarrow \mu^+ + \nu_\mu, \mu^+ \rightarrow e^+ + \nu_e + \bar{\nu}_\mu$$

The undetected particles produced in the pion and muon decay were considered to be identical to the neutrinos produced in the  $\beta$ -decay. L. Lederman, M. Schwarz, and J. Steinberger experimentally discovered the muon neutrino in 1962 using accelerator neutrinos.

## Tau Neutrinos

Discovered at Stanford in 1975, the third charged lepton  $\tau$  has a corresponding neutrino known as tau neutrino ( $\nu_\tau$ ). Along with the  $\tau$ , it forms the third generation of leptons. The tau neutrinos would be produced in  $\tau^\pm$  decays. The discovery of tau neutrino was announced in July 2000 by the DONUT collaboration from Fermilab [19]. The IceCube Neutrino Observatory published their findings on the seven astrophysical tau neutrino candidates in 2024 [20].

### 1.4.2 Neutrino interactions

Neutrinos have two important types of interactions:

- Neutrinos can couple with a  $Z^0$  boson. In this interaction, also known as neutral current interactions, neutrinos change their four-momentum but don't change the flavor. The  $Z^0$  interactions are elastic or quasi-elastic scattering processes:

$$Z^0 \rightarrow \nu_\alpha + \bar{\nu}_\alpha$$

- Neutrinos can couple to  $W^\pm$  boson, known as charged current interactions. In this interaction, a charged lepton transforms into a neutrino by emitting a  $W$  boson, or a  $W$  boson generates a neutrino-charged lepton pair.

$$W^+ \rightarrow l^+ + \nu_l, W^- \rightarrow l^- + \bar{\nu}_l$$

Where the label  $l = e, \mu, \tau$  are the neutrino flavors corresponding to the charged lepton type.

The  $Z^0$  decay helps us to determine the number of light neutrinos possible. The presence of neutrinos is evident from the difference between the total decay width of the  $Z^0$  boson and the width of the visible particle.

$$\Gamma_{inv} = \Gamma_{tot} - \Gamma_{vis} = 499.0 \pm 1.5 \text{MeV}$$

The partial width of  $Z^0 \rightarrow \nu_\alpha + \bar{\nu}_\alpha$  can be precisely calculated in the SM:

$$\Gamma_{\nu_\alpha \bar{\nu}_\alpha} = 166.9 \text{MeV}$$

The branching ratio for  $Z$  decaying into the invisible final state is given as:

$$\Gamma_{inv} = N_\nu \Gamma_{\nu_\alpha \bar{\nu}_\alpha}$$

The form in the above equation suggests that the branching ratio for  $Z$  is directly proportional to the number of neutrino species.

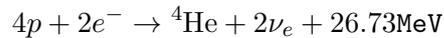
$$N_\nu = \frac{\Gamma_{inv}}{\Gamma_{\nu_\alpha \bar{\nu}_\alpha}} = 2.994 \pm 0.012$$

Thus, in the above equation, it became clear that there are three light neutrino flavors, which is also indicated by the standard model.

### 1.4.3 Sources of Neutrinos

The most abundant particle in the Universe are the Neutrinos. They play an important role in astrophysical and cosmological events. Neutrinos constitute a cosmic neutrino background radiation produced soon after the birth of the universe. Some neutrinos are continuously produced from particle accelerators and nuclear reactors, whereas some neutrinos have cosmological and astrophysical sources like supernova, sun, and stars. In brief:

- **Cosmological Neutrinos:** The neutrinos present from the early epochs of the evolution of the universe and have a number density of around  $56 \text{ cm}^{-3}$  for each of the  $\nu_e, \bar{\nu}_e, \nu_\mu, \bar{\nu}_\mu, \nu_\tau, \bar{\nu}_\tau$ .
- **Supernovae:** Neutrino emission from supernova explosions was confirmed back in February 1987, when the neutrinos from supernova SN1987A reached Earth. Kamiokande detected 11 events in Japan and 7 events by IMB in the US [21] at a time interval of 13 seconds.
- **Stars:** The thermonuclear reactions in the stellar interior (particularly in the sun) produce neutrinos.



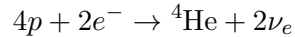
- **Natural Radioactivity Neutrinos:** The Earth emits energy from the radioactive nuclei decay. A radioactive nuclei like  ${}^{238}\text{U}$  can decay into a stable nucleus like  ${}^{206}\text{Pb}$  by emitting a cascade of  $\alpha$  and  $\beta$  particles. In each of these  $\beta$  decay induced at the surface of the Earth  $\nu_e$  is emitted.
- **Atmospheric Neutrinos:** The Earth receives constant and isotropic flux of cosmic rays. The primary cosmic rays, which are high-energy particles from outer space, interact with the upper atmosphere to produce a series of secondary particles, including charged pions and kaons, which in turn generate neutrinos.

$$\pi^+ \rightarrow \mu^+ + \nu_\mu, \quad \mu^+ \rightarrow e^+ + \nu_e + \bar{\nu}_\mu$$

- Astrophysical Neutrinos: Detecting very high energy neutrinos from the ‘Ultra High Energy’ cosmic rays sources like Active Galactic Nuclei or Gamma Ray Bursts.
- Accelerator and Reactor Neutrinos: These are the two important man-made sources of neutrinos.

#### 1.4.4 Solar Neutrino Problem

Among the many neutrino sources, the sun is of the utmost importance. The neutrinos from the sun, also known as solar neutrinos, are produced by nuclear fusion reactions in the central region of the Sun, where the density is very high. In this fusion reaction, the four protons and electrons together produce a helium-4 nucleus and two electron neutrinos.



Each fusion reaction releases a total energy of 26.73 MeV, which is shared as kinetic energy among all the final state particles. The neutrinos take only a small portion of the released energy, which then escapes from the sun and directly reaches the Earth without any absorption. The photons transport a large fraction of these energies. All the neutrinos produced in the sun are electron neutrinos. The flux of solar neutrinos is given by:

$$\Phi_{\nu_e} \simeq \frac{1}{4\pi d_\odot^2} \frac{2L_\odot}{(Q - \langle E_\nu \rangle)}$$

Where  $L_\odot$  is the solar luminosity, around  $3.842 \times 10^{33}$  erg/s,  $d_\odot$  is the distance between the Sun and the Earth and is  $1.495 \times 10^{13}$  cm,  $Q$  is the total energy of the fusion reaction and  $E_\nu$  is the average energy carried by the neutrinos in the fusion cycle. The total flux at Earth is  $6 \times 10^{14} \text{ m}^{-2} \text{ s}^{-1}$ . This is known as the ‘‘Solar Standard Model’’ due to the work of John Bahcall.

The radiochemical experiments did various measurements for solar neutrino flux: the chlorine [22, 23, 24, 25] and two Gallium experiments GALLEX in Italy [26, 27, 28, 29] and SAGE in Russia [30, 31, 32]. There was a statistical deficit of neutrino as observed by all measurements except the measurement that involved neutral currents. The Gallium experiments probed the lower-energy solar neutrinos and noticed the smallest deficit, whereas the chlorine experiment witnessed the largest deficit. This was the first evidence for the disappearance of  $\nu_e$  and became known as a solar neutrino puzzle.

A breakthrough came with an improved version of the Kamiokande experiment, Super-Kamiokande, around 1996, and the Sudbury Neutrino Observatory in Canada around 1999,

as they joined the effort to solve the puzzle corresponding to the solar neutrino deficit. Roughly two-thirds of the neutrinos coming from the sun are the electron neutrinos. They change their flavor with distance and arrive on the Earth as a muon or tau neutrinos. In Chapter 2, the detailed formalism of neutrino oscillation is discussed.

# Chapter 2

## Neutrino Formalism

The existence of neutrino “flavor oscillations” was first predicted by Bruno Pontecorvo [33, 34] back in 1957. He proposed that the state of neutrinos produced in the process of weak interactions is a superposition of states of two Majorana neutrinos with definite mass. At that time, only electron neutrino was known. The theory of  $\nu_e \rightleftharpoons \nu_\mu$  was developed by Maki and Sakata in 1962 [35]. In 2015, T. Kajita and Arthur B. McDonald were awarded the Nobel Prize for their contribution to discovering Neutrino oscillations. Analogous to the mixing of the mass eigenstates in the quark sector, a similar mixing phenomenon was possible in the leptonic sector. The neutrinos  $\nu_l$  ( $l = e, \mu, \tau$ ) produced in association with the charged lepton  $l^-$  do not have a definite mass but are a linear combination of the states that have a well-defined mass.

$$\begin{bmatrix} \nu_e \\ \nu_\mu \\ \nu_\tau \end{bmatrix} = U^{PMNS} \begin{bmatrix} \nu_1 \\ \nu_2 \\ \nu_3 \end{bmatrix}$$

where  $U^{PMNS}$  is the Pontecorvo-Maki-Nakagawa-Sakata matrix [36, 37], which is the leptonic [38] analogous of the Cabibbo-Kobayashi-Maskawa (CKM) matrix for quarks. Neutrinos can change their flavor as they travel from one place to another, irrespective of the medium. The neutrino flavor change is a quantum mechanical effect. The neutrinos produced in charged-current weak interactions in association with charged leptons are weak flavor eigenstates:  $\nu_e, \nu_\mu$ , and  $\nu_\tau$ . These flavor eigenstates can be written as a linear superposition of three mass eigenstates  $\nu_1, \nu_2$  and  $\nu_3$  having masses  $m_1, m_2$  and  $m_3$  as:

$$|\nu_\alpha\rangle = \sum_j U_{\alpha j}^* |\nu_j\rangle$$

where  $\nu_\alpha$  and  $\nu_j$  are the flavor and mass eigenstates respectively.  $U$  is the neutrino mixing or PMNS matrix.

At time  $t=0$ , the neutrino is produced as the flavor eigenstates  $|\nu_\alpha\rangle$ . At the later time  $t$ , we work out here to find the probability of neutrino being present in a different flavor eigenstate  $|\nu_\beta\rangle$ .

At  $t = 0$ ,

$$|\nu(0)\rangle = |\nu_\alpha\rangle = \sum_j U_{\alpha j}^* |\nu_j\rangle$$

At a later time  $t$ ,

$$|\nu_\alpha\rangle = \sum_j U_{\alpha j}^* e^{-iE_j t} |\nu_j\rangle$$

where the phase factor  $e^{-iE_j t}$  indicates the time evolution of the mass eigenstates. The probability amplitude of finding the neutrino at the time  $t$  in a flavor state  $|\nu_\beta\rangle$ :

$$\begin{aligned} A(\nu_\alpha \rightarrow \nu_\beta; t) &= \langle \nu_\beta | \nu(t) \rangle \\ &= U_{\beta k} \langle \nu_k | \{ e^{-iE_j t} U_{\alpha j}^* |\nu_j\rangle \} \\ &= U_{\beta k} U_{\alpha j}^* e^{-iE_j t} \langle \nu_k | \nu_j \rangle \end{aligned}$$

using  $\langle \nu_k | \nu_j \rangle = \delta_{jk}$

$$A(\nu_\alpha \rightarrow \nu_\beta; t) = U_{\beta j} U_{\alpha j}^* e^{-iE_j t}$$

Oscillation probability is:

$$\begin{aligned} P(\nu_\alpha \rightarrow \nu_\beta; t) &= |A(\nu_\alpha \rightarrow \nu_\beta; t)|^2 \\ &= |U_{\beta j} U_{\alpha j}^* e^{-iE_j t}|^2 \end{aligned}$$

## Two Flavor Case

In the mixing of two neutrino flavors (e.g.  $\nu_e$  and  $\nu_\mu$ ), we have two mass eigenstates ( $\nu_1$  and  $\nu_2$ ) and two mass eigenvalues ( $m_1$  and  $m_2$ ).

$$\begin{bmatrix} |\nu_e\rangle \\ |\nu_\mu\rangle \end{bmatrix} = \begin{bmatrix} \cos \theta & \sin \theta \\ -\sin \theta & \cos \theta \end{bmatrix} \begin{bmatrix} |\nu_1\rangle \\ |\nu_2\rangle \end{bmatrix}$$

where  $\theta$  is the mixing angle. At  $t = 0$ ,

$$|\nu(t = 0)\rangle = |\nu_e\rangle = \cos\theta|\nu_1\rangle + \sin\theta|\nu_2\rangle$$

Two neutrino mass eigenstates have energies  $E_1$  and  $E_2$  are given as:

$$E_i = \sqrt{p^2 + m_i^2} \simeq p + \frac{m_i^2}{2p} \simeq E + \frac{m_i^2}{2E}$$

At a later time,

$$|\nu(t)\rangle = \cos\theta e^{-iE_1 t}|\nu_1\rangle + \sin\theta e^{-iE_2 t}|\nu_2\rangle$$

For  $\nu_e \rightarrow \nu_\mu$

$$\begin{aligned} P(\nu_\alpha \rightarrow \nu_\beta; t) &= |\langle \nu_\mu | \nu(t) \rangle|^2 \\ &= |\{-\sin\theta\langle \nu_1 | + \cos\theta\langle \nu_2 | \} |\nu(t)\rangle|^2 \\ &= (\cos^2\theta \sin^2\theta) |e^{-iE_2 t} - e^{-iE_1 t}|^2 \\ &= 2\cos^2\theta \sin^2\theta \{1 - \cos(E_2 - E_1)t\} \\ &= \sin^2 2\theta \sin^2 \frac{(E_2 - E_1)t}{2} \\ &= \sin^2 2\theta \sin^2 \left( \frac{\Delta m^2 t}{4E} \right) \end{aligned}$$

As for relativistic neutrino  $L \simeq t$ ,

$$P(\nu_\alpha \rightarrow \nu_\beta; t) = \sin^2 2\theta \sin^2 \left( 1.27 \Delta m^2 \frac{L}{4E} \right)$$

## Three Flavor Case

Similarly, in the case of three flavors, the mixing matrix is parametrized by three mixing angles and one CP-violating phase ( $\delta$ ).

$$\begin{aligned}
U^{PMNS} &= \begin{bmatrix} 1 & 0 & 0 \\ 0 & c_{23} & s_{23} \\ 0 & -s_{23} & c_{23} \end{bmatrix} \begin{bmatrix} c_{13} & 0 & s_{13}e^{-i\delta} \\ 0 & 1 & 0 \\ -s_{13}e^{i\delta} & 0 & c_{13} \end{bmatrix} \begin{bmatrix} c_{12} & s_{12} & 0 \\ -s_{12} & c_{12} & 0 \\ 0 & 0 & 1 \end{bmatrix} \\
&= \begin{bmatrix} c_{12}c_{13} & s_{12}c_{13} & s_{13}e^{-i\delta} \\ -s_{12}c_{23} - c_{12}s_{13}s_{23}e^{i\delta} & c_{12}c_{23} - s_{12}s_{13}s_{23}e^{i\delta} & c_{13}s_{23} \\ s_{12}s_{23} - c_{12}s_{13}c_{23}e^{i\delta} & -c_{12}s_{23} - s_{12}s_{13}c_{23}e^{i\delta} & c_{13}c_{23} \end{bmatrix}
\end{aligned}$$

where  $\theta_{12}$ ,  $\theta_{13}$  and  $\theta_{23}$  are the neutrino mixing angles and  $\delta$  is the CP violating phase.

The oscillation probability:

$$\begin{aligned}
P(\nu_\alpha \rightarrow \nu_\beta) &= \left| \sum_j U_{\beta j} U_{\alpha j}^* e^{-\frac{im_j^2 L}{2E\nu}} \right|^2 \\
&= \delta_{\alpha\beta} - 2 \sum_{k>j} \Im[U_{\beta j} U_{\beta k}^* U_{\alpha j}^* U_{\alpha k}] \sin \frac{\Delta m_{jk}^2 L}{2E} + 4 \sum_{k>j} R[U_{\beta j} U_{\beta k}^* U_{\alpha j}^* U_{\alpha k}] \sin^2 \frac{\Delta m_{jk}^2 L}{4E}
\end{aligned}$$

## 2.0.1 Neutrino Oscillation in Matter

Neutrinos not only propagate in a vacuum, but they also propagate in a medium-filled material. The solar neutrinos produced in the center of the sun have to travel across a lot of solar material to reach Earth. Similarly, atmospheric or cosmic neutrinos have to travel the bulk material of the Earth before being detected by the detectors placed on the surface of the Earth. The presence of matter affects neutrino propagation through the coherent effect of forward scattering. Neutrinos can undergo forward scattering while interacting with ordinary matter composed of electrons, protons, and neutrons, giving rise to an effective potential coming from all the target particles.

The effective potential for  $\nu_e$  can proceed with  $W$  and  $Z^0$  exchange.

$$V_{\nu_e e} = V_{\nu_e e}^W + V_{\nu_e e}^Z = \sqrt{2}G_F N_e - \frac{\sqrt{2}}{2}G_F N_e$$

Similarly  $\nu_\mu$  and  $\nu_{\tau}$  can proceed with  $Z^0$  exchange.

$$V_{\nu_\mu e} = V_{\nu_\tau e} = -\frac{\sqrt{2}}{2}G_F N_e$$

$$V_{\nu_e p} = V_{\nu_\mu p} = V_{\nu_\tau p} = \frac{\sqrt{2}}{2}G_F N_p$$

$$V_{\nu en} = V_{\nu \mu n} = V_{\nu \tau n} = \frac{-\sqrt{2}}{2} G_F N_e$$

where  $G_F$  indicates the Fermi Coupling Constant and  $N_e$  the electron number density. The potential difference is proportional to the electron density  $N_e$ .

$$V = V_{\nu e} - V_{\nu \mu} = \sqrt{2} G_F N_e \quad (2.1)$$

The effective potential due to matter effect is known as the Wolfenstein potential, also popularly known as the Mikheyev-Smirnov-Wolfenstein (MSW) effect [39].

The Schrodinger equation for a neutrino traveling through matter is given as:

$$i \frac{\partial}{\partial t} |\nu(t)\rangle = \mathcal{H} |\nu(t)\rangle$$

The effective mixing matrix in matter:

$$U_M = \begin{bmatrix} \cos \theta_M & \sin \theta_M \\ -\sin \theta_M & \cos \theta_M \end{bmatrix}$$

and the Hamiltonian can be recasted after adding the matter's potential contribution:

$$\begin{aligned} \mathcal{H} &= \mathcal{H}_\nu + \mathcal{H}_M \\ &= \frac{\Delta m^2}{4E_\nu} \begin{bmatrix} -\cos 2\theta + x & \sin 2\theta \\ -\sin 2\theta & \cos 2\theta - x \end{bmatrix} \end{aligned}$$

where  $x = \frac{2\sqrt{2}G_F N_e E}{\Delta m^2}$ . By dividing and multiplying the above equation by  $\sqrt{\sin^2 2\theta + (\cos 2\theta - x)^2}$ , we get:

$$\mathcal{H} = \frac{(\Delta m^2)_{eff}}{4E_\nu} \begin{bmatrix} \cos \theta_M & \sin \theta_M \\ -\sin \theta_M & \cos \theta_M \end{bmatrix}$$

where  $\sin^2 2\theta_M = \frac{\sin^2 2\theta}{\sin^2 2\theta + (\cos 2\theta - x)^2}$  and  $(\Delta m^2)_{eff} = \Delta m^2 \times \sqrt{\sin^2 2\theta + (\cos 2\theta - x)^2}$ .

In the two-flavor neutrino case,

$$|\nu_e\rangle = |\nu_1\rangle \cos \theta_M + |\nu_2\rangle \sin \theta_M$$

$$|\nu_\mu\rangle = -|\nu_1\rangle \sin \theta_M + |\nu_2\rangle \cos \theta_M$$

The eigen values of  $\mathcal{H}_M$  are:

$$\lambda_1 = \frac{(\Delta m^2)_{eff}}{4E_\nu}, \lambda_2 = \frac{-(\Delta m^2)_{eff}}{4E_\nu},$$

Thus solving  $i\frac{\partial}{\partial t}|\nu(t)\rangle = \mathcal{H}|\nu(t)\rangle$  with  $|\nu(0)\rangle = |\nu_e\rangle$ , we get

$$|\nu(t)\rangle = -|\nu_1\rangle e^{-i\frac{\Delta m_{eff}^2}{4E_\nu}t} \cos \theta_M + |\nu_2\rangle e^{+i\frac{\Delta m_{eff}^2}{4E_\nu}t} \sin \theta_M$$

The oscillation probability is given by:

$$\begin{aligned} P(\nu_e \rightarrow \nu_\mu) &= |\langle \nu_\mu | \nu(t) \rangle|^2 \\ &= | -\sin \theta_M e^{-i\frac{\Delta m_{eff}^2}{4E_\nu}t} \cos \theta_M + \cos \theta_M e^{i\frac{\Delta m_{eff}^2}{4E_\nu}t} \sin \theta_M |^2 \\ &= | \sin \theta_M \cos \theta_M (e^{i\frac{\Delta m_{eff}^2}{4E_\nu}t} - e^{-i\frac{\Delta m_{eff}^2}{4E_\nu}t}) |^2 \\ &= | \sin \theta_M \cos \theta_M (2i \sin \frac{\Delta m_{eff}^2}{4E_\nu}t) |^2 \\ &= \sin^2 2\theta_M \sin^2(\frac{\Delta m_{eff}^2}{4E_\nu}t) \end{aligned}$$

The final expression for oscillation probability in the presence of matter effect is given as:

$$P(\nu_e \rightarrow \nu_\mu) = \sin^2 2\theta_M \sin^2(\frac{\Delta m_{eff}^2}{4E_\nu}L) \quad (2.2)$$

The oscillation parameters modify the matter effect based on the density of the material medium and neutrino energy. From  $(\Delta m^2)_{eff} = \Delta m^2 \times \sqrt{\sin^2 2\theta + (\cos 2\theta - x)^2}$ , we can see that when  $\cos 2\theta = x$ , then  $(\Delta m^2)_{eff} = \Delta m^2$ . This leads us to the MSW resonance. At resonance, the effective mixing angle becomes  $45^\circ$ , which amplifies the oscillation probabilities. The neutrino oscillation program has recently entered a new era where the known parameters are being measured with an ever-increasing accuracy.

## 2.0.2 Beyond the Standard Model

Along with the Higgs boson, Neutrinos are the least understood particles in the standard model framework. Physics beyond the standard model helps us to explain its shortcomings. The standard model of particle physics does not adequately explain many fundamental physical phenomena in nature.

- The Standard Model (SM) does not explain gravity.
- According to SM, neutrinos do not oscillate. However, the evidence of neutrino oscillation has accumulated from observing solar and atmospheric neutrinos over many years. Neutrinos do not have mass in the standard model, and adding mass terms to the standard model will lead us to new theoretical physics beyond the standard model.
- The matter-antimatter asymmetry present in the universe. SM predicts that matter and antimatter are created equally and does not explain this asymmetry.
- Dark Matter and Dark Energy: The SM explains about 5% of the mass energy present in the universe. Dark matter constitutes about 26% , and the remaining 69% of the universe consists of dark energy. SM does not provide any good dark matter candidates.

Among these many issues beyond the standard model, we will consider two important topics in our thesis. First, we will discuss topics beyond the standard model, including lightweight (sub-GeV) dark matter candidates.

### Light-Dark Matter

The visible matter in our universe constitutes only about 5% , whereas the dark matter constitutes about 85% of the universe. Even though dark matter accounts for about five times ordinary matter, we still have very little knowledge about it. The Swiss American astronomer Fritz Zwicky is considered to be a pioneer in the field of dark matter. He coined the term dark matter in 1933 in order to describe the invisible matter associated with the Coma Cluster. He studied the redshifts of various galaxies and visualized that few of the galaxies within the Coma Cluster are exhibiting large velocities dispersion with respect to other clusters. In order to explain the difference noticed in the apparent velocities, Zwicky estimated the mass-to-light ratio of the Coma Cluster by combining Hubble's and Van Maaen's results. If we consider that both results are correct, then there is an apparent mismatch between the theoretical and observed total mass density. After this study, Zwicky concluded:

*“If this would be confirmed, we would get the surprising result that dark matter is present in much greater amount than the luminous matter.”*

In literature, it is cited as the first usage of the phrase “dark matter”. [40, 41]. In the 1970s, Vera Rubina and Kent Ford measured the speed of the galaxy rotation and found evidence that dark matter is hindering the galaxies from flying apart. The rotation curves of galaxies as a function of their distance from the galactic center played a vital role in discovering dark matter.

Despite numerous efforts, there has not been much success in identifying the dark matter candidate particle. The evidence of dark matter’s presence comes from astronomical sources like Bullet Clusters, Cosmic Microwave Background, and Gravitational Lensing. Dark matter includes all types of astrophysical objects that appear to be so faint that they can not be detected with the available telescope. The inability of dark matter to interact with the visible matter in the universe has kept the real nature of dark matter as a mystery. The elusive nature of DM to any interaction with the electromagnetic field means it does not absorb, reflect, or emit appreciable electromagnetic radiation in any known waveband and is, therefore, difficult to detect. All the visible matter that we know of, like atoms, neutrinos, photons, antimatter, and all the other particles present in the Standard Model, interact through at least one known quantum force, but dark matter appears to interact through gravity alone. In 2006, Zurek and colleagues proposed that the dark matter could be part of a hidden sector, having its own way of interaction properties and independent constituents of the Standard Model. Unlike normal matter, the hidden-sector particles would live in a dark universe of their own. Proposed dark matter candidates in literature span over vast orders of magnitude in mass, and the range varies from elementary particles infinitesimally lighter than electrons to sizable primordial black holes.

Regarding detection efforts, the most important dark matter classes are neutrinos, WIMPs [42], MACHOs, and axions. In the case of neutrinos, we know that they are weakly interacting particles, and due to their elusive nature, they aren’t easy to detect. Even though they were created in large amounts during the Big Bang and still today are in abundance, they are impossible to detect. This nature of neutrinos can be attributed to the fact that they interact only via electroweak interactions. Due to various obvious reasons, it is quite unlikely that neutrinos discovered in particle accelerators and nuclear reactors on Earth will be responsible for much of the dark matter. However, it is still possible that some undiscovered weakly interactive particles formed during the Big Bang still remain abundant to make the dark matter. The typical mass required for these candidate particles is less than that of 1 GeV. Thus, it is rightly named as light-dark matter. The concept of light-dark matter was developed to explain the 511 keV  $\gamma$  ray from the galactic bulge as observed by the INTEGRAL satellite. These light-dark matter particles are produced via a vector mediator particle coupling with the SM particles. Masses of dark matter, dark

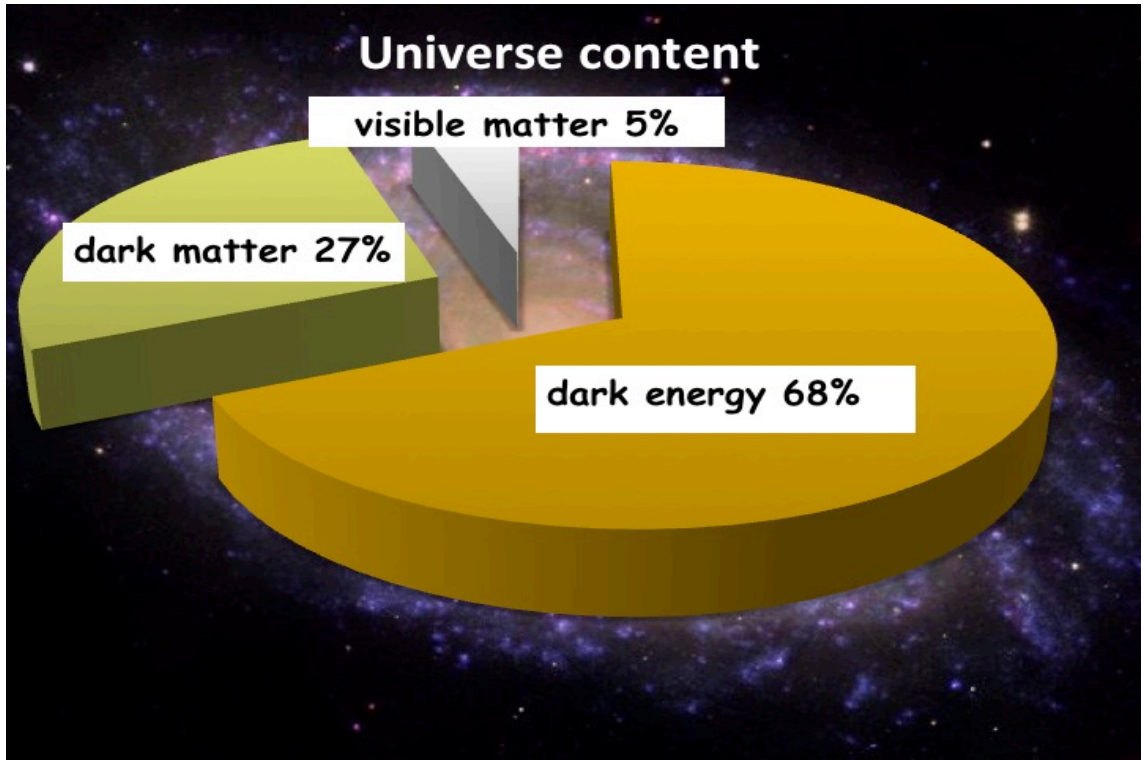


Figure 2.1: A schematic representation of the composition of the Universe

photons, the kinetic mixing parameter, and the gauge coupling parameter characterize the vector portal model. The details of the light-dark matter analysis are discussed in chapter 5

## Non-Standard Interactions

The standard model was one of the most successful models in the particle physics realm until various loopholes in the form of solar and atmospheric anomalies emerged. The standard model dictates neutrinos as massless particles, which contradicts the neutrino oscillation measurements [5, 43, 44, 45]. There is a requirement for the standard model to be revised to introduce neutrino masses and mixings, which indicates new physics beyond the standard model. To answer the origin of neutrino masses [46] and mixing, the search for new physics became more relevant. Including neutrino mass generation in most models demands extra interactions in the form of non-standard interactions (NSI). Currently, there is no experimental evidence related to non-standard interactions of neutrinos, which is impossible to include in the Standard model of physics. Non-standard interactions [47, 48, 49, 50, 51, 52, 53, 54] are quite interesting from a phenomenological point of view as their presence will hint at some new physics beyond the standard model.

To explain the solar [55, 22, 56, 57] and atmospheric anomalies [58], new interactions

apart from the standard interactions are required. The presence of possible NSI was first pointed out by Wolfenstein [59] in the early stage, much before the experimental discovery of neutrino oscillation. We discuss the phenomenological analysis of NSI in chapters 6 and 7 for long baseline Neutrino experiments.

## Chapter 3

# NOvA Experiment



Figure 3.1: The NOvA experiment layout shows that the near detector is located at Fermilab while the Far Detector is placed 810 km away at Ash River, Minnesota

The NuMI off-axis  $\nu_e$  Appearance (NOvA) experiment is a long baseline neutrino oscillation experiment located at Fermilab, USA [60]. NOvA experiment uses two detectors: Near Detector (ND), which is onsite at Fermilab at a baseline of 1 km, and Far Detector (FD), which is 810 km away at Ash River, Minnesota. The Near Detector is a 300 metric-ton detector, whereas the Far Detector is a much larger 14 metric-kiloton detector comprising 344,000 cells of highly reflective plastic filled with a liquid scintillator. Nova utilizes a beam of high intensity, which is composed of primary muon (anti)neutrinos coming from the Neutrinos at the Main Injector (NuMI) beam at Fermilab. The ND is placed 1km

downstream from the neutrino source and is mainly used to measure the energy spectra of  $\nu_\mu$  and  $\nu_e$  events after oscillations at the Far Detector (FD). The primary goal of the NOvA experiment is to observe and study  $\nu_\mu \rightarrow \nu_e$  oscillations. In addition to that, NOvA aids in the study of the mass hierarchy by comparing the oscillations of a beam of muon neutrinos to that of muon antineutrinos. Also, it can help us in the search for the effects of the CP-violating phase.

## 3.1 NuMI Beam

### 3.1.1 Fermilab Accelerator Complex

Fermilab’s particle accelerator enhances the study of fundamental physics and helps advance accelerator-based applications. The Fermilab accelerator complex consists of four important parts spanning a total of 16 km of accelerator and beamlines: a 400 MeV Linear accelerator (LINAC), an 8 GeV Booster synchrotron, a 120 GeV Main Injector, and an 8 GeV anti-proton Recycler storage ring in the Main Injector tunnel [61, 62]. The Main Injector at Fermilab produces one of the world’s most powerful proton beams for various generations of experiments. For instance, proton beams are produced for past experiments like MINERvA, MINOS, and MiniBooNE, ongoing experiments like NOvA and ICARUS, and one of the upcoming world-class experiments like DUNE. The accelerator complex will receive a powerful upgrade with the PIP-II project, which includes the construction of a 215-meter-long linear particle accelerator. The potential and pliability that are included in the design of PIP-II will enable multiple simultaneous upcoming experiments.

Fig 3.2 gives a schematic view of the accelerator complex. The beam originates from an H-ion source followed by a 750 keV Radio Frequency Quadrupole (RFQ) to accelerate a continuous beam of charged particles with high efficiency and preserve the emittance along with a 400 MeV pulsed linac that injects into an 8 GeV synchrotron booster. The Recycler is then stacked with high-intensity protons to be loaded into the 120 GeV Main Injector. The accelerator complex has delivered the neutrino beam with an average uptime of 85% over the last five years. The proton output from the accelerator complex after the 2014-2018 upgrade delivers 700 kW of 120 GeV beam power from the Main Injector (MI). The modification in the Recycler slip-stacking RF system and the Main Injector ramp changed the cycle time to 1.1s in the MI. The total protons per hour achieved from the booster is around  $2.1 \times 10^{17}$ .

### 3.1.2 NuMI Beamline

The neutrino beam produced at the Fermilab accelerator complex is used in NOvA, along with several neutrino experiments like MINOS and MINERvA at Fermilab. The NuMI

## Fermilab Accelerator Complex

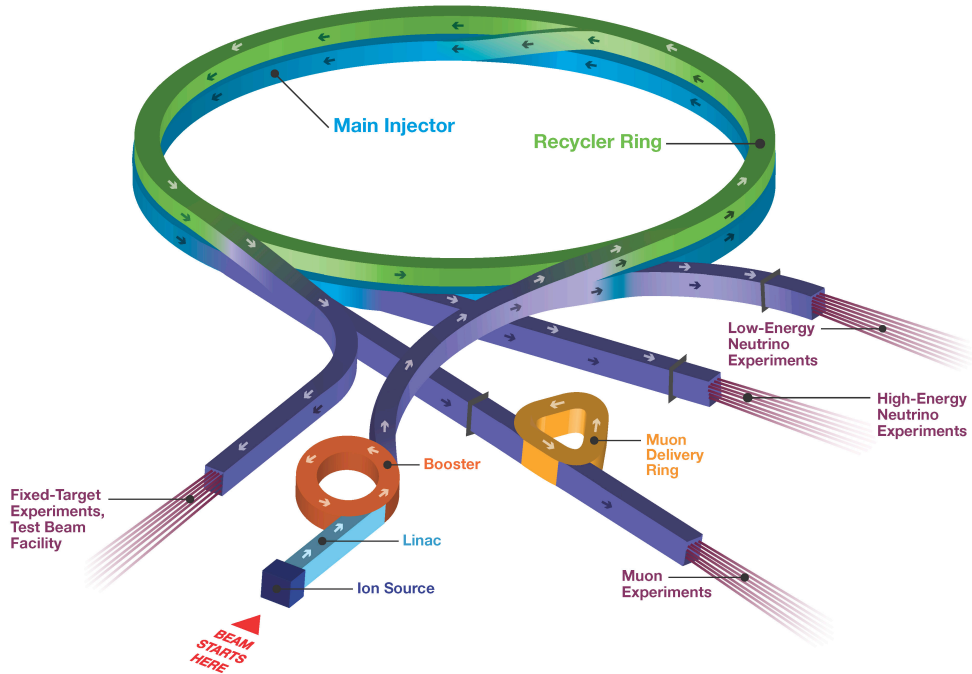
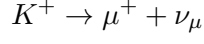
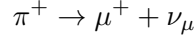


Figure 3.2: The Schematics of Fermilab Accelerator Complex.

beam facility produces high-energy neutrinos by steering a 120 GeV proton beam extracted from the Fermilab's Main Injector. These proton beams are then focused onto a narrow graphite target of 0.95 m long and 350 m away from the extraction point. The graphite target has 47 segmented rectangular pieces stacked together. The rectangular pieces are 20.0 mm long and separated with a space of 0.3 mm, making a total length of 95.4 cm and a density of  $1.78\text{g/cm}^3$ . Charged mesons are produced when protons interact with the target material. A two parabolic magnetic horns focus produced secondary charged particles. This magnetic horn is made up of aluminum and is a bi-layered coaxial conductor sheet and filled with low-density gas. Through the horn, 200 kA current is passed to create a  $1/R$  magnetic field, which focuses the charged particles of a particular sign and deflects the opposite sign. We can change our current according to our need for neutrino or anti-neutrino beam. Pion and Kaon decay to produce neutrinos when they travel through a decay pipe, which is 675m long. The primary sources of neutrinos in the decay pipe are pion and kaon decays. Kaon decay also produces a minimal amount of  $\nu_e$ , which leads to an inherent amount of  $\nu_e$  in

the background.



An additional dolomite muon shield, which is 240m long is also present to remove any remaining muons present in the beam before reaching the ND.

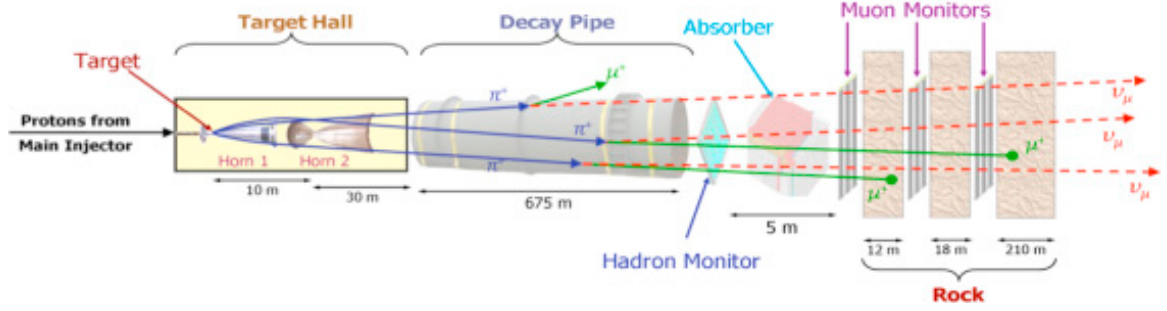


Figure 3.3: A schematic view of the NuMI beamline

### 3.1.3 Off-Axis Detectors

The NOvA detectors were placed 14.6 mrad off the center of the NuMI beam axis, in contrast to the MINOS detectors placed on the center of the NuMI beam. This is known as the “off-axis” placement of the NOvA detectors. For a given lab of the frame, the flux and energy of the neutrinos produced during the decay of  $\pi \rightarrow \mu + \nu$  detected by a detector of area ‘a’ and distance ‘x’:

$$F = \left( \frac{2\gamma}{1 + \gamma^2\theta^2} \right)^2 \frac{a}{4\pi x^2}$$

$$E_\nu = \frac{0.43E_\pi}{1 + \gamma^2\theta^2}$$

where  $\gamma = E_\pi/m_\pi$ ,  $E_\pi$  is the energy of the parent pion,  $m_\pi$  is the mass of the pion, and  $\theta$  is the angle between the pion direction and the neutrino direction. Similarly, for the kaon decay:

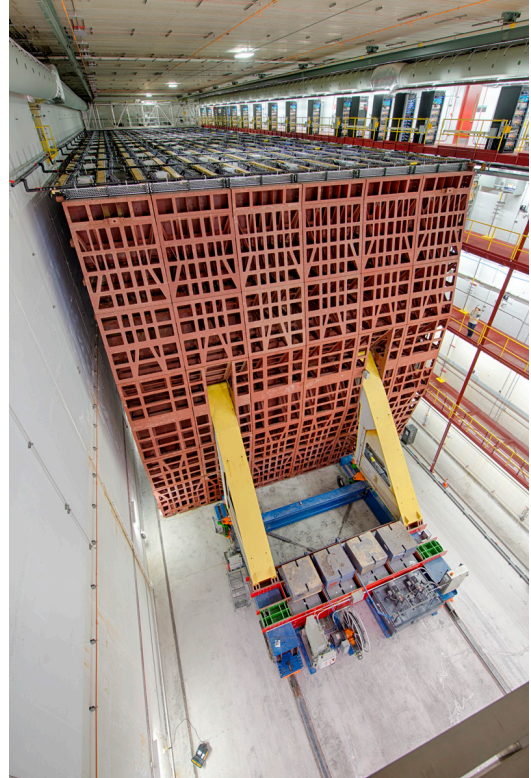
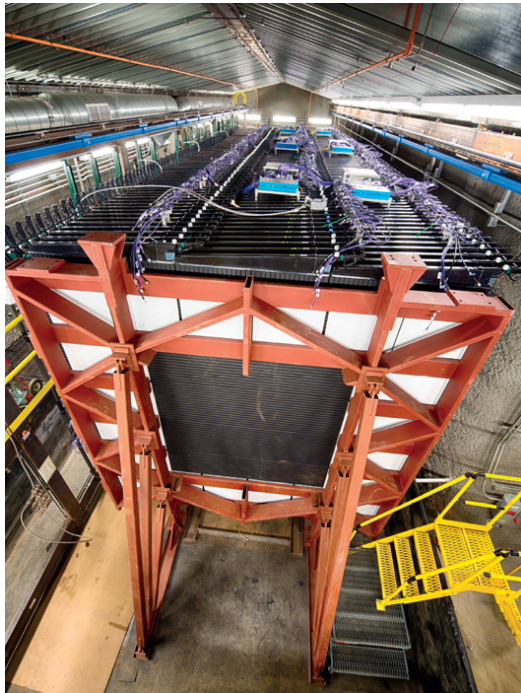


Figure 3.4: Near Detector on the left and Far Detector on the right

$$E_\nu = \frac{0.96E_K}{1 + \gamma^2\theta^2}$$

In Fig 3.5, we visualize the neutrino flux and energy distribution as a function of pion energy for various pion directions.

As shown in Fig 3.5 taken from [63], at 14.6 milliradians off-axis, NuMI beams generate a narrow band of neutrino energy spectra. For the baseline corresponding to the NOvA experiment of 810 km, the first oscillation maximum occurs around 2 GeV. At an off-axis angle of 14.6 mrad, a larger amount of 2 GeV neutrinos were seen at NOvA than if it were on-axis. In addition to enhanced flux, the narrow off-axis spectra also help reduce background events from higher energy-neutral current (NC), which can mimic the detectors'  $\nu_e$  events.

### 3.1.4 NOvA Detectors

#### Near Detector

The NOvA Near Detector (ND) is situated 1 km away from the NuMI target and 100 m underground at Fermilab adjacent to the MINOS access tunnel. The detector has an active

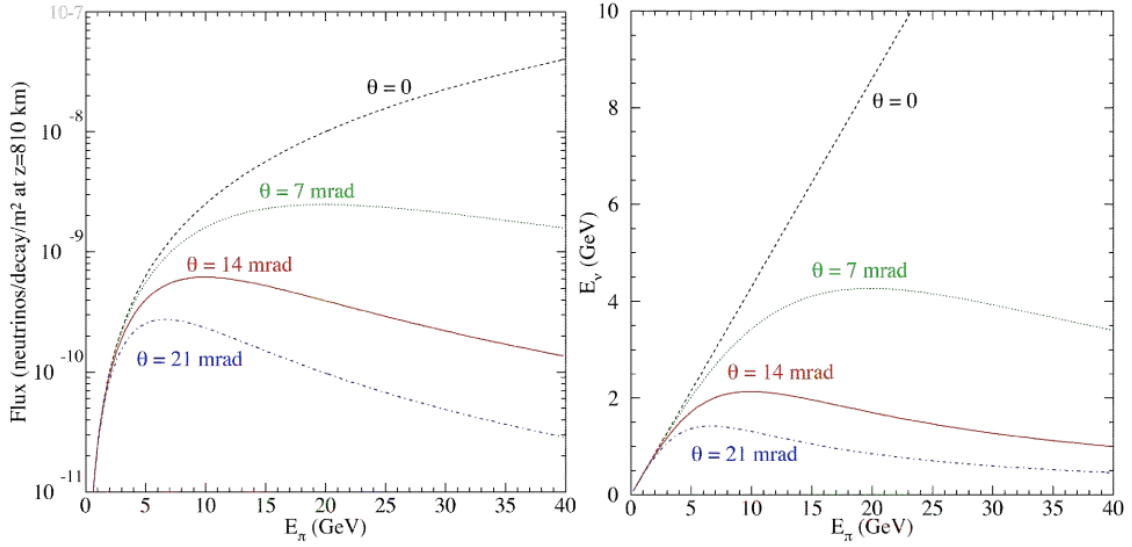


Figure 3.5: The Neutrino Flux and energy distribution with respect to pion of Energy  $E_\pi$  for various angles ( $\theta$ ) of the detector placement from the beam axis. The red curve in the picture shows the off-axis angle chosen for both NOvA detectors to optimize the sensitivity for the oscillation of  $\nu_\mu$  to an  $\nu_e$

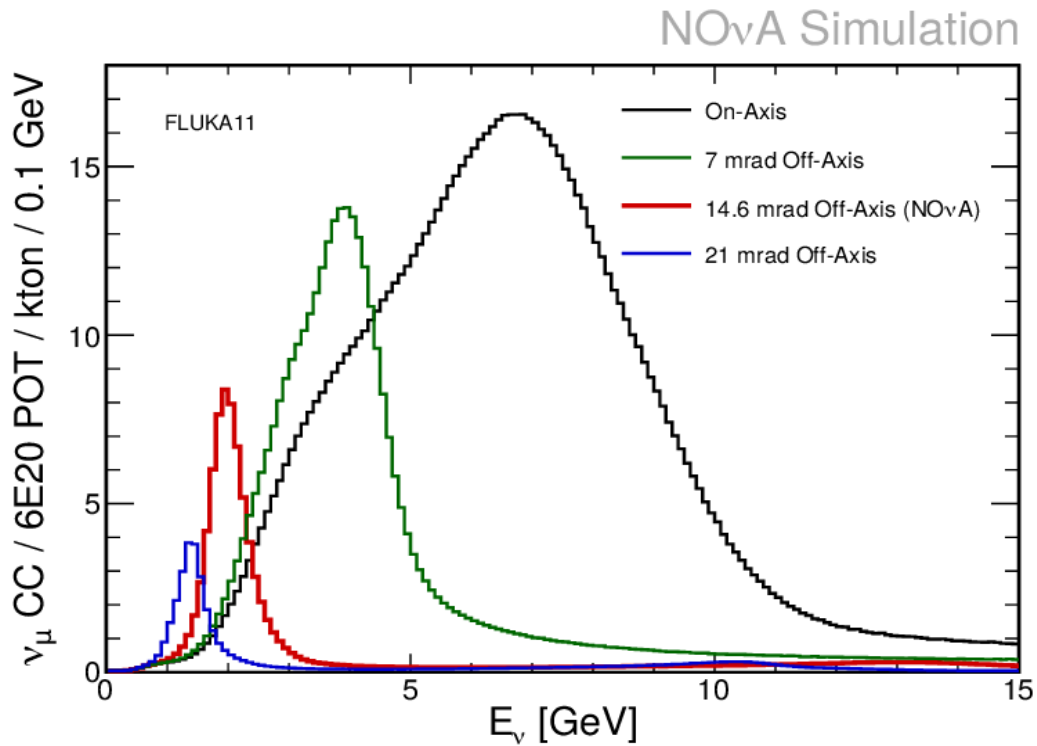


Figure 3.6: Neutrino energy spectra that the NOvA Far Detector would see for various off-axis angles.

detector mass of 125 metric tons and a total mass of 215 metric tons. In Fig 3.6, we can see that the detector is split into four logical regions: an upstream veto red region to hold the detector in place, the fiducial volume of the detector indicated by green, the yellow shower containment region and the shower containment region is followed by the muon catcher with ten steel planes, each having a thickness of 0.1 m and a plane of liquid scintillator. The Near Detector is 2.8 m wide, 4.1 m high, and 14.5 m long. The muon catcher is 4.85 m long and aims to completely contain the electron showers coming from the charged current  $\nu_e$  interactions. The muon catcher and containment region will obstruct the few GeV muons produced from the charged current  $\nu_\mu$  interactions.

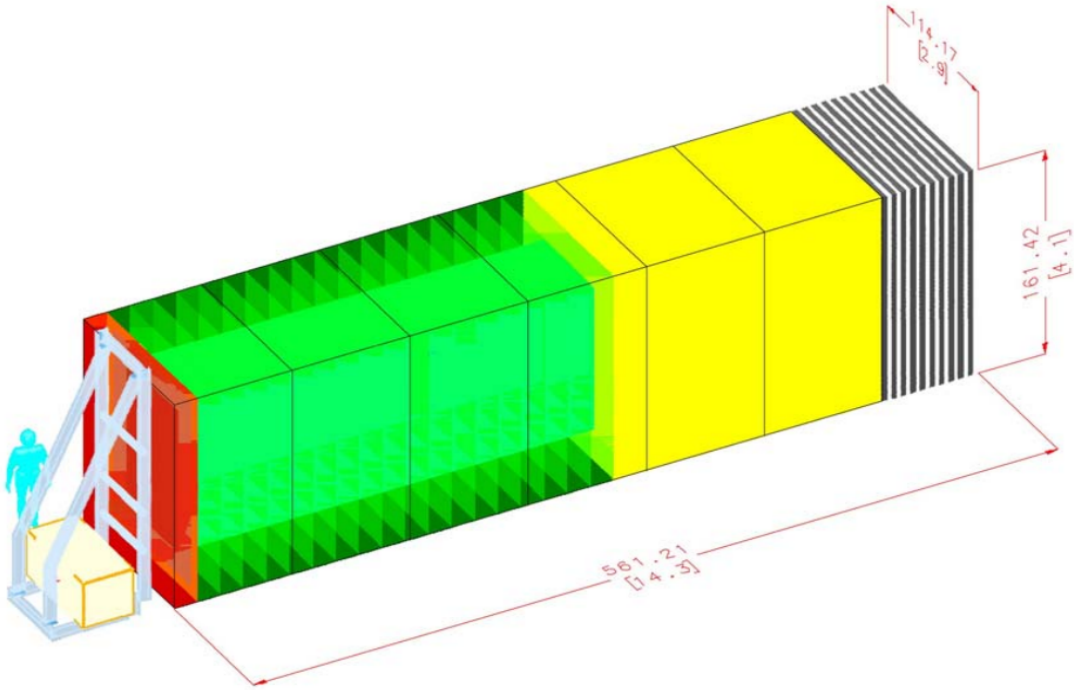


Figure 3.7: A schematic view of the Near Detector

## Far Detector

Far Detector (FD) is not underground and is located about 810 km away from the NuMI target at Ash River, Minnesota. It is a much larger detector with 14 kilo-ton active detector mass and has dimensions of 15 m wide, 15 m high, and 60 m long. Two pairs of 32-plane blocks are glued together to form 14 di-blocks. Each of these di-blocks has 12 DCMs, with each comprising 64 FEBs. The primary goal of FD is to measure the energy spectra for our neutrino beam, separating muon and electron neutrino charged-current (CC) interactions from neutral-current (NC) interactions.



Figure 3.8: A schematic view of the Far Detector

## Detector Materials and Cells

Both the Near and Far Detector comprise extruded polyvinyl chloride (PVC) cells. The cells are  $4\text{ cm} \times 6\text{ cm} \times$  the height or width of the detector. The grouping of the cells alternates horizontal and vertical orientations perpendicular to the detector's length. The PVC plastic cell contains a liquid scintillator and wavelength-shifting fiber. The fiber is twice the cell's length and looped at one PVC end. This provides the effectiveness of two fibers in the cell, with a nearly perfect mirror at the bottom capturing nearly four times the light of a single non-reflecting fiber. The charged particles travel along the cell's depth, and scintillator light is produced in the liquid. Both ends of the fiber are directed toward the Avalanche Photodiode (APD), and the captured light is then converted into an electronic signal.

The cells of NOvA are made up of titanium dioxide, which is a highly reflective material. The cells are rigid with 2 to 4.5 mm thick walls. The liquid scintillator inside the NOvA cells constitutes about 75% of the NOvA detector mass, about 10.5 kilotons. The main composition of the scintillator liquid is mineral oil with 4.1% of 1,2,4-Trimethylbenzene as the scintillant. The liquid also contains chemical additives like 2,5-diphenyloxazole and 1,4-di(methylstyryl)benzene. An anti-static agent is also added to the liquid to prevent the charge build-up inside the cells. In addition, an anti-oxidant (tocopherol (Vitamin E)) is used to

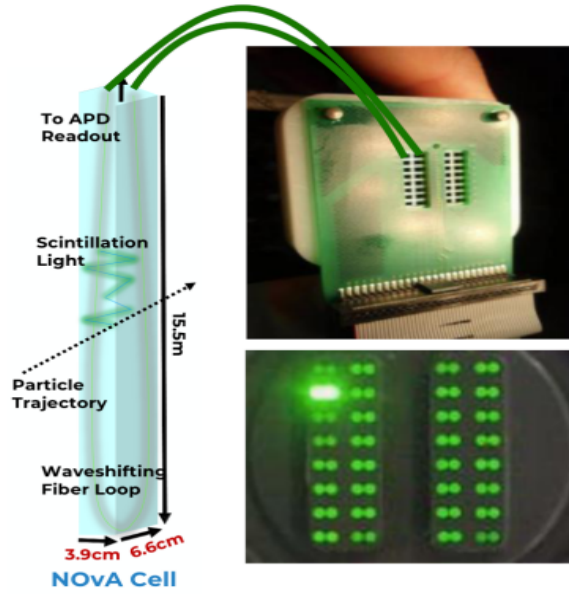


Figure 3.9: Wavelength-shifting fiber collects and transports light to Avalanche photodiode

prevent the change of color of the scintillator, which would break down its transparency over time.

Table 3.1: Composition of the liquid scintillator

| Component    | Purpose           | Mass Fraction |
|--------------|-------------------|---------------|
| Mineral Oil  | Solvent           | 95.8          |
| Pseudocumene | Scintillant       | 4.1           |
| PPO          | Wave shifter      | 0.091         |
| bis-MSB      | Wave shifter      | 0.0013        |
| Stadis-425   | Anti-static agent | 0.0003        |
| Vitamin E    | Antioxidant       | 0.0010        |
| Total        |                   | 100           |

## 3.2 NOvA Data Acquisition System

NOvA DAQ system comprises four main components: a timing distribution system, an array of Data Concentrator modules (DCM), an Ethernet network, and a buffer farm.

The avalanche photodiode (APD) is the photodetector at NOvA. Each of these APDs is packed with arrays of 32 pixels. Each of these 32 pixels maps to the 32 cells of a single PVC extrusion module. Light is absorbed, and electron-hole pairs are produced and then propagate to the p-n junction under the influence of the applied electric field. As we have an Avalanche Photodiode, the multiplication of electrons occurs when a sufficiently high electric field is applied. Compared to photomultipliers, APDs have high quantum and uniform spectral quantum efficiency. These lights from the APDs are digitized by the Front End Board (FEB). The FEBs continuously read out the signal from the detector cells with a time interval of 500  $\mu$ s. After digitization of the signal by FEBs from the APDs, it is sent to a Data Concentrator Module (DCM). Data Concentrator Modules (DCMs) collect data from all of the 64 FEBs and send data packets to the computing farm for further processing.

DCM consists of a field-programmable gate array (FPGA) that aggregates the hits packets into 50  $\mu$ s long “microslices”. Those microslices are regrouped into 5ms “millislices” that are sent to the server farm, which then decides as to save the data to disk or discard it. Accurate, precise, and synchronized timing is critical for recording rapid spills and crucial for large detectors that are more than 800 kilometers away. The ND timer receives a signal from the throttle distribution when a beam spill happens. That signal is then sent to the FD timing system, which corrects the flight time between the detectors (approximately 2.7 ms). The timing system comprises GPS receivers and timing distribution units (TDUs). Each detector’s primary TDU receives a clock signal from the GPS system, ensuring that both detectors are synchronized to the same global reference clock. That signal is transmitted to a set of secondary TDUs that are connected to the DCM. The secondary TDUs are arranged in a loop where the last TDU in the row has a loop that delivers the signal back into the loop. Each secondary TDU is then connected to a chain of DCMs; the final DCM also has feedback. These loops are used to allow TDUs to account for delays due to cable length by the time difference between the original signal and the echo signal traveling back up the loop. The primary TDU sends a signal indicating the incoming timestamp to synchronize the timing chains. A sync signal is then sent down the line, and each component begins counting its delay times. When the countdown ends, each component starts counting down from the sent timestamp, and all components are now synchronized.

The last step in the DAQ system is buffer nodes. Each buffer node receives a 5ms snapshot of the entire detector from the DCM. When all nodes have one millicut, the next millicut returns to the first node, and the cycle repeats until all nodes are full. This means that the time to look at the buffer space depends on the data transmission rate coming from the detector and the number of buffer nodes in the space. A typical lookback time is about 20 minutes for each detector. Buffer nodes decide whether to keep the “interesting” data or to discard it. Data are recorded in 50  $\mu$ s microslice time windows. Each NuMI beam spill is recorded. To generate data-driven triggers (DDTs), DAQ also sometimes stores clock-based

triggers and performs minimal data reconstruction. Those DDT generations are based on detector-specific criteria. DDTs also capture other interesting physics phenomena, such as supernovae and magnetic monopoles, and search for dark matter. We have shown a schematic map of the NOvA DAQ system in Fig 3.10 taken from [cite 10.1007/978-3-031-43583-6\_3]

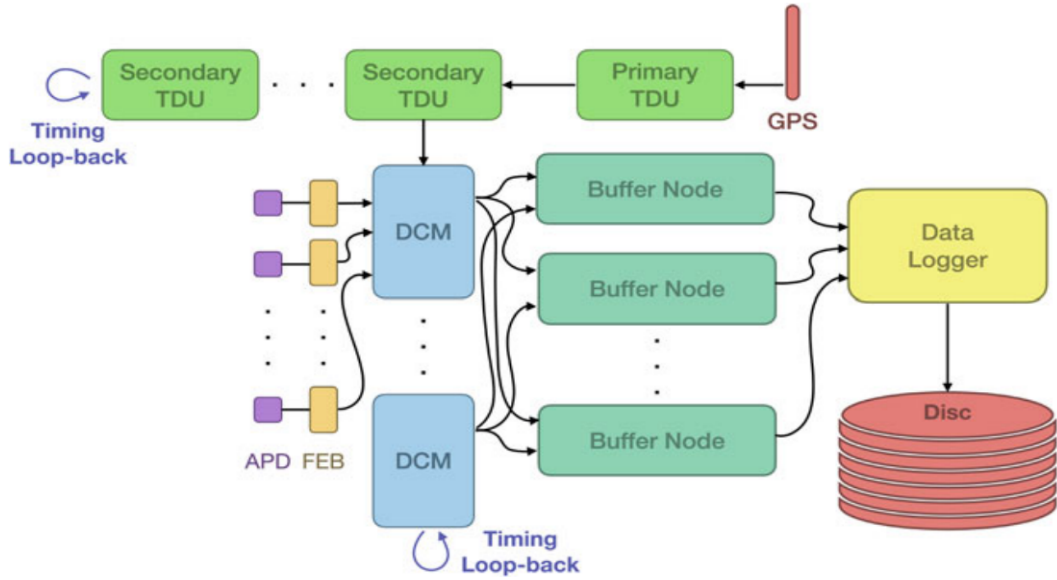


Figure 3.10: NOvA DAQ System

# Chapter 4

## NOvA Simulation and Reconstruction

Simulation plays an important role in every high-energy physics analysis that we perform. There are several steps in the simulation, such as measurement, creating an independent data set to practice particle detection and tuning the analysis to the desired configuration, asserting the selection efficiency, and estimating neutrino energy and the related background components for signals. NOvA experiment uses various sets of tools to simulate datasets for several physical processes. The simulation corresponding to the NOvA experiment consists of three crucial stages: beam, GENIE, and detector simulation. This chapter will explore the robust modeling and analysis techniques of NOvA simulation.

The primary source of beam for the NOvA experiment is the NuMI beam, which is predominantly a  $\nu_\mu$  and  $\bar{\nu}_\mu$  beam. The source of neutrino flux in the experimental setup is an energetic 120 GeV proton beam from the Main Injector that interacts with the graphite target. For the analysis study, the starting point of the simulation is the production of the flux after the interaction of the proton beam with the target. The flux comprises neutrino flavor, directions, energy, and momentum of the simulated neutrino. The flux expected from the NuMI beam is simulated using a GEANT4 [64] based simulation which accurately describes the beamline geometry and material composition, known as G4NuMI. G4NuMI is utilized in the simulations to optimize the NuMI target and horn system. G4NuMI also facilitates the simulation of hadron production at the NuMI target and the downstream hadron monitors' absorption of muons and hadrons. The flux files store the information related to the parent particles as they are required for event reweighting based on the hadronic model studies.

Constraints from the hadron production experiments improve the simulation of hadron production and initialize correction to the nominal neutrino flux. The corrections are applied as weights by the Package to Predict the Flux (PPFX) developed by the MINERvA

collaboration at Fermilab [65]. Fig 4.1 taken from [66] shows a flux neutrino composition after applying PPFX corrections. The mismodeling of hadron production is a more severe issue. Such mismodelling can lead to differences in data and simulation for the analysis carried out in NOvA. The PPFX derives an uncertainty by using the multi-universe technique. In this technique, nearly 100 scenarios are generated; each of them is random and represents a world with different proton target cross-sections. Corresponding to each of these universes, a set of weights is introduced that are derived based on the hadronic interaction history, i.e., the kinematics detail of all interactions and the amount of material transversed by each individual neutrino. A covariance matrix is constructed for each of these 100 universes using these interaction weights. These covariance matrices are summed into a mean covariance matrix, which can be summarized using principal component analysis (PCA). The PCA enables the storage of hadron production uncertainty as principle component. Factors like target position, the magnetic field in the decay pipe, and the amount of current in the horns are also included in the PCA.

### 4.0.1 Neutrino Interactions

The Monte Carlo neutrino generators simulate the neutrino interactions with the detector and their surrounding materials. NOvA utilizes the GENIE generator to model the neutrino beam interactions. The GENIE generator inputs flux files to process detector volumes' interactions. It also simulates different types of neutrino interactions like Quasi-elastic (QE), Resonance Pion Production (RES), Deep Inelastic Scattering (DIS), Coherent (COH), and Meson Exchange Current (MEC) interactions.

- Quasi-elastic Interactions: The neutrino scatters elastically off the nucleon, exchanging  $W$  boson and ejecting from the a nucleon and a charged lepton in the final state.
- Resonance Pion Production: In this process, mesons are produced in the final state by exciting the nucleon into a resonant state. Due to the unstable nature of the resonant states, there is further decay into mesons and nucleons.
- Deep-inelastic Scattering: Here, the neutrino scatters off a quark present inside the nucleon and produces a chaotic hadronic state. The neutrino has sufficient energy at the quark level to interact within the nucleons, which is termed “deep”.
- Coherent Scattering: In this process, neutrino interacts with the nucleus and coherently scatters off the target nucleus with a small amount of energy exchange between them with the final states consisting of pions, kaons, and rho.
- Meson Exchange Current: In this process, when neutrino communicates with nucleons through  $W$  boson, it gets absorbed by nucleons and knocks out two-nucleon and two-hole pairs (2p-2h) via an exchange of a meson

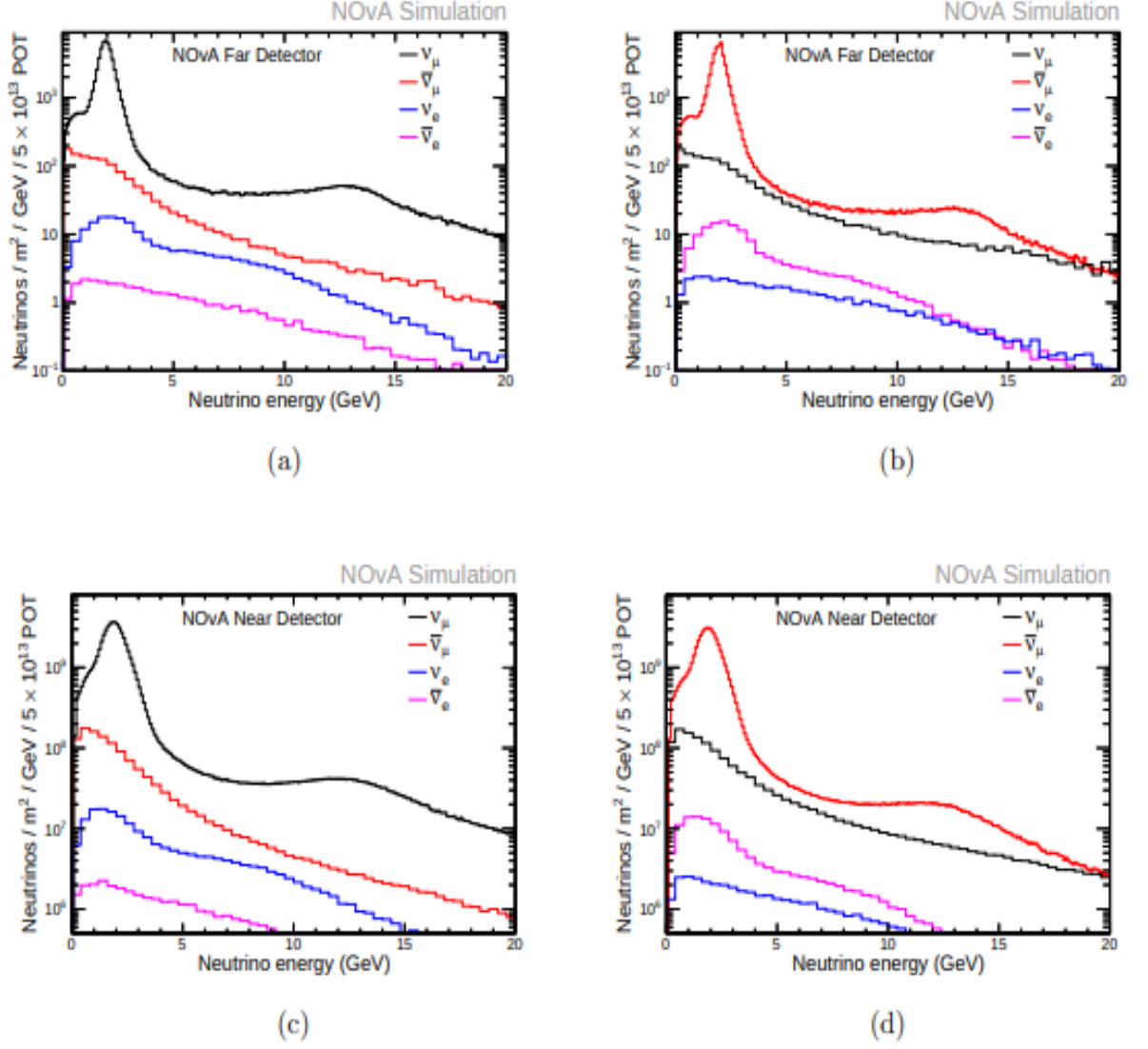


Figure 4.1: The major component of neutrino flux at FD (top) and ND (bottom) for FHC (left) and RHC (right) mode.

The final stage interactions are simulated in GENIE using Intranuke. Along with the cross-section prediction, GENIE also provides simulation related to systematic uncertainty for various parameters involved in the modeling of neutrino cross-sections. The simulation of the detector volume and surrounding materials in the detector hall is enabled by GENIE.

## 4.0.2 Particle Propagation

The GENIE [67] output is fed into GEANT4 [64] for particle propagation. For the simulation of particle propagation, the information corresponding to detector geometry is crucial. The NOvA detectors, detector halls, and surrounding rocks are encoded in the Geome-

try Description Markup Language (GDML) files. GEANT4 simulates particle propagation to save the relevant information regarding energy depositions of particles having energy less than 100 eV. Various physical processes are modeled via different physics lists. Among them is the QGSP BERT HP, which is a standard physics list for electromagnetic processes, Bertini-style cascade (BERT) modeled up to 9.5 GeV, Quark Gluon String (QGSP) model for protons, neutrons, pions, kaons, and nuclei falling into high energy range. The individual particle energy deposits are the output from GEANT4 required in the next simulation stages.

The main task of GEANT4 is determining how much energy is deposited in the detector cells. The higher the amount of energy deposited in the cell, the higher is the scintillation light produced. The wavelength-shifting fiber transfers the scintillation light as a signal to the APDs.

### 4.0.3 Reconstruction

The reconstruction of neutrino interactions is of utmost importance to achieve the analysis goal in the NOvA experiment. Their difference in event topology can distinguish each event interaction. In Fig 4.2, we have one detector view for each event, and the cell hits are colored corresponding to their charge deposition as in Fig 4.3. The  $\nu_e$  charged current interaction produces an electromagnetic electron shower. The  $\nu_\mu$  charged current interactions produce a muon as a narrow track along its trajectory rather than a shower.

The NOvA detector collects raw data from the readout. These readouts are generally the energy deposition in the detector cells and are called cell hits. The plane, cell, time, and charge of the hits contain the required information. We also have “slices,” which are the space and time correlations between the hits that are clustered together. For each cluster of hits, reconstruction algorithms determine the most likely location of an interaction vertex. These hits are then divided further into groups pointing away from the vertex in ‘prongs’. Prongs are produced by the “fuzzy-k-means” algorithm. A modified Hough transform algorithm [68] identifies lines in each of these slices. Using the Elastic Arms algorithm, these Hough lines reconstruct a global 3D neutrino. Another tracking algorithm, the Kalman algorithm, is extremely useful in identifying particles that do not create large electromagnetic or hadronic showers.

The data collection in NOvA is in the form of packets of hits within a 550-microsecond readout window for both detectors. All of these collected hits can be grouped into two categories, signal and noise. NOvA has some quality cuts corresponding to the beam and detector for efficient reconstruction purposes. Beam quality cuts check the quality of the beam for each event using variables such as beam width and position, horn current, and POT (Proton on Target) per beam spill. Along with beam quality cuts, we have detector quality cuts, which ensure that both detectors are working without any issues and are

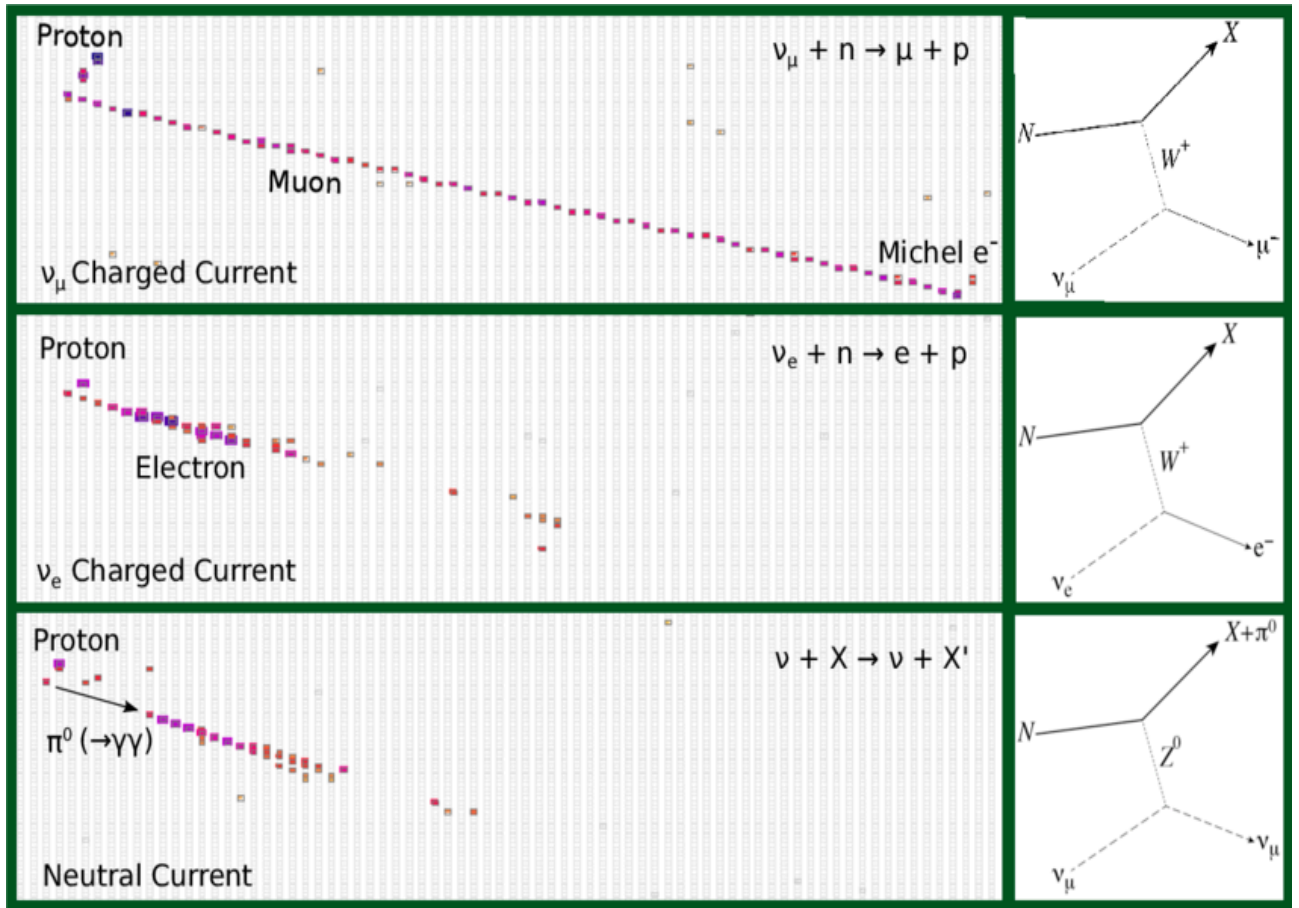


Figure 4.2: Neutrino interactions showing a  $\nu_\mu$  CC interaction (top panel),  $\nu_e$  CC interaction (middle panel), and NC interaction (bottom panel).

reporting in accordance with each other. One of the important criteria is the containment cut, which requires that the vertex be far enough from all the edges of the detector so that the outgoing particles' energies are well-contained within the detector.

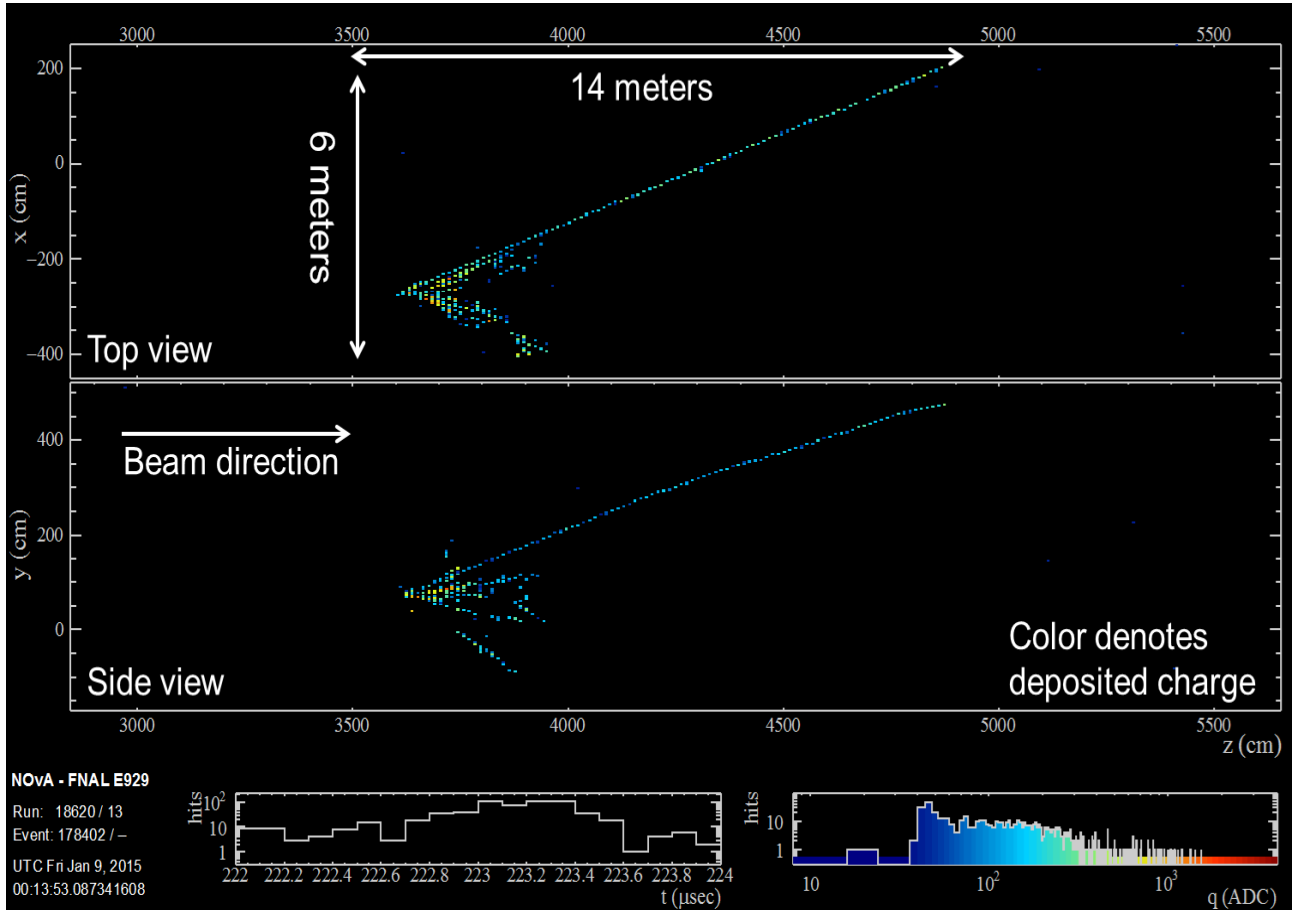


Figure 4.3: A sample Event Display showing that color denotes deposited charges.]

# Chapter 5

## Light-Dark Matter Analysis in NOvA Near Detector

Dark matter (DM) [69, 70, 71, 72, 73, 74] is believed to account for 85% of the matter content of the Universe. The leading dark matter candidate is the WIMP (weakly interacting massive particles). Light dark matter (LDM) refers to WIMP candidates with a mass of less than 1 GeV. The concept of LDM has been developed to explain the 511 keV  $\gamma$ -rays from the galactic bulge, as observed by the INTEGRAL satellite. There are a lot of candidates for light DM, and these candidates span a wider range of potential masses that can couple to the visible sector. Probing the huge parameter space of light-dark matter requires a correspondingly broad experimental program that can include neutrino-fixed target experiments. In this aspect, NOvA could be an ideal candidate to explore a sizeable new region of parameter space for light-dark matter. We aim to search for the MeV-scale dark matter particles that might be generated within the NuMI beam and produce detectable electron scattering signals in the NOvA Near Detector.

### 5.1 Analysis Overview

NOvA, one of the high-luminosity fixed-target neutrino experiments, can provide a potentially interesting probe of MeV-scale DM interaction in its near detector [75, 76, 77, 78, 79]. The main advantage of NOvA lies in its high luminosity. The near detector has accumulated more than  $2.5 \times 10^{21}$  POT since 2013, which can aid in producing a sizeable relativistic DM beam. The underground direct detection experiments offer the possibility of probing a wide range of possible DM masses and couplings to the visible sector.

This work aims to search for light DM signals from  $\sim 2.5 \times 10^{21}$  POT data recorded by the NOvA near detector through their non-gravitational interactions with the detector media. For this analysis, we choose the Vector Portal as the benchmark model and look for

the single forward scattering electrons produced by light DM. To search for the light DM signature signals, we perform a **raster scan** over a wide range of possible light DM mass in the concerned parameter space and determine the detector sensitivity using **template fit** considering the neutrino background and the systematic uncertainties. We produce light DM samples, nominal and with systematic shifts, to generate the signal templates and build neutrino background templates from existing official NOvA simulation samples. Figure 5.16 illustrates the background templates and some signal templates. In this analysis, we make use of existing neutrino-electron analysis tools/conclusions, such as the well-defined cuts for single forward scattering electron selection, and develop new analysis tools for single-electron events analysis, which can be incorporated into the NOvA CAFAna framework and can be used for other single-electron analysis projects as well. CAFAna name is derived from CAFs – Common Analysis Files – the standard analysis-level file format used throughout NOvA. In this work, we show the sensitivity of the NOvA experiment derived from the simulated samples.

### 5.1.1 Vector Portal Model

Vector Portal is the benchmark model via which the Hidden Sector particles couple with the Standard Model (SM) particles. This benchmark model includes a dark photon (DP)  $V_\mu$ , a new dark  $U(1)_D$  gauge boson that kinetically mixes with the ordinary photon, and a complex scalar  $\chi$  charged under  $U(1)_D$  that acts as DM candidates [80].

$$\mathcal{L}_{\text{DM}} = \mathcal{L}_V + \mathcal{L}_\chi. \quad (5.1)$$

The  $\mathcal{L}_V$  can be written as:

$$\mathcal{L}_V = -\frac{1}{4}F'_{\mu\nu}F'^{\mu\nu} + \frac{1}{2}m_V^2 V^\mu V_\mu - \frac{1}{2}\epsilon F'_{\mu\nu}F^{\mu\nu}, \quad (5.2)$$

where the DP-photon kinetic mixing is given by  $\epsilon$ , while:

$$\mathcal{L}_\chi = \frac{1}{2}ig_D V_\mu J_\mu^\chi + \frac{1}{2}\partial_\mu \chi^\dagger \partial^\mu \chi - m_\chi^2 \chi^\dagger \chi, \quad (5.3)$$

where  $J_\mu^\chi = [(\partial_\mu \chi^\dagger - \chi^\dagger \partial_\mu \chi)]$  and  $g_D$  is the  $U(1)_D$  gauge coupling. The Vector Portal model predicts the production of  $V$  mediators at the high luminosity proton beam dumps via indirect neutral meson decay or proton bremsstrahlung process and the decay of  $V$  to a pair of DM particles. Four unknown parameters control the DM study:

- DM Mass  $m_\chi$
- DP Mass  $m_V$

- Kinetic Mixing  $\epsilon$
- Dark Gauge Coupling  $g_D$

The parameter space reachable by NOvA ND is  $m_V > 2m_\chi$  and  $g_D \gg \epsilon e$ , which implies the DP decays into a  $\chi\chi^\dagger$  pair. For  $m_V > 2m_\chi$ , the annihilation cross section can be written as [70]:

$$\langle\sigma_{\text{ann}}v\rangle(\chi^\dagger\chi \rightarrow f\bar{f}) \sim \frac{8\pi v^2 Y}{m_\chi^2}, \quad (5.4)$$

where the relative DM velocity is given by  $v$ , and the so-called self-annihilation parameter  $Y$  is a dimensionless parameter that controls the DM annihilation cross-section and, in turn, the thermal relic abundance, which is defined as:

$$Y \equiv \epsilon^2 \alpha_D \left(\frac{m_\chi}{m_V}\right)^4, \quad (5.5)$$

where  $\alpha_D \equiv g_D^2/4\pi$ .  $Y$  captures the essential parameter scaling of the annihilation and scattering cross-sections and assists the comparison with direct detection sensitivity. The  $U(1)_D$  gauge coupling  $\alpha_D$  has a constraint on DM self-scattering cross section coming from halo shape and bullet clusters observations. The limit  $\alpha_D \leq 0.5$  is applied, where this upper bound is suggested by the running of  $\alpha_D$  [80].

If assumed to be a thermal relic, Light DM requires annihilation channels through light mediators to avoid over-production in the early universe. In this work, we try to explore the region where  $\chi$  is a thermal relic compatible with the observed DM relic energy density and present the sensitivity of NOvA experiment on light DM search in the  $(Y, m_\chi)$  space by considering as the benchmark point:  $\alpha_D = 0.5$  with  $m_V = 3m_\chi$ , which is the region of the parameter space where the correct thermal abundance is obtained [81]. The mass ratio  $m_V/m_\chi$  can also be changed within the condition of  $m_V > 2m_\chi$  with kinematics staying reasonably similar within a few percent. The choice of  $m_V = 3m_\chi$  is not completely random but allows us to compare with findings from various other measurements.

### 5.1.2 DM Production and Detection

The 120 GeV proton beam from the Main Injector is available for use by the Fermilab NuMI facility, which also provides neutrinos to the MINOS, NOvA, and MINERvA detectors, which are located nearby. The beam of protons from Fermilab's Main Injector is directed onto a carbon target. In the interaction of the proton beam with the target, DPs could be produced by rare decays of neutral mesons, such as  $\pi^0$  and  $\eta$ , or for heavier masses, via the proton bremsstrahlung process. The DPs decay promptly into DM particles, producing a "DM beam" along the neutrino beam. The NuMI facility could serve as a DM factory [79], and the NOvA near detector could be a DM detector [78].

For the smaller values of mediator particle mass ( $m_V$ ), the neutral meson decay provides the dominant production channel for light DM particles  $\chi$ :

$$\phi \rightarrow \gamma + V \rightarrow \gamma + \chi\chi^\dagger. \quad (5.6)$$

And the total number of DM particles from decays of such mesons can be written as

$$N_\chi = 2N_{\text{POT}}N_{\phi/\text{POT}}\text{Br}(\phi \rightarrow \chi\chi^\dagger\gamma). \quad (5.7)$$

where the two factor considers the production of the  $\chi\chi^\dagger$  pair.  $N_{\text{POT}}$  is the number of POT and the number of mesons per POT,  $N_{\phi/\text{POT}}$ , for  $\pi^0$  is  $\sim 1$  and for  $\eta$  is around 1/30 of that for  $\pi^0$ .

For higher mass of DP or DM ( $m_V > 120\text{MeV}$ ), an additional production channel, through proton bremsstrahlung, becomes important:

$$p + N \rightarrow p + N + V \rightarrow p + N + \chi\chi^\dagger, \quad (5.8)$$

with  $N = p$  or  $n$ . This channel could provide a significant DM source with very little angular spread:

$$N_\chi = 2\frac{N_{\text{POT}}}{\sigma(pN)}\sigma(pN \rightarrow pN\chi\chi^\dagger), \quad (5.9)$$

where  $\sigma(pN) \sim 40\text{mb}$  is the overall cross section between protons and neutrons in a 120 GeV beam.

A fraction of this DM beam can enter into the near detector. Some of them might interact with SM particles through a reverse process, elastically scattered on a nucleon or electron of a neutrino detector, as shown in Fig. 5.1.

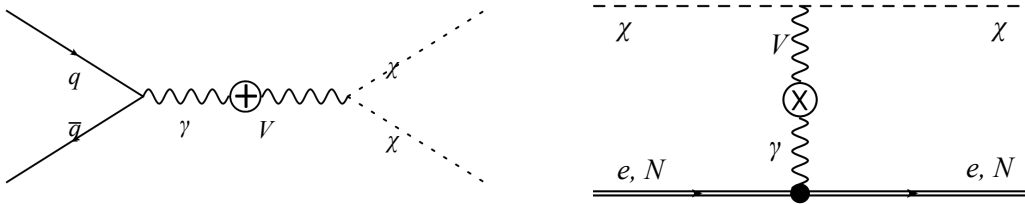


Figure 5.1: **Left:** direct production of vector mediator  $V$  and DM; **Right:** DM-matter interaction via the reversed process.

Unlike neutrinos, for which the ratio of scattering cross sections on the nucleus and the electron is  $O(10^4)$  [82], DM-electron scattering is a more dominant process. Depending on the mass of DM particles (still assuming  $Y \sim 10^{-9}$ ), the DM beam might leave  $O(10^8)$  to

$O(10^4)$  detectable signals inside the NOvA near detector through DM-electron interactions per year.

The DM particles production via neutral meson ( $\pi^0$  or  $\eta$ ) decay and proton bremsstrahlung processes are considered. The DM-electron interaction is basically the elastic scattering of light DM on atomic electrons. This channel is relatively weak compared to the scattering on nucleons, but it is a clear and well-understood leptonic process with easily identifiable signals.

### 5.1.3 Dark Matter Signal Identification

The DM beam interacts with SM particles by elastically scattering off on a nucleon or electron inside the neutrino detector. The DM-electron elastic scattering is a purely leptonic process, and two body elastic collisions give the kinematics. The scattering angle  $\theta_e$  of the outgoing electron with respect to the DM beam can be written as:

$$\cos\theta_e = \frac{E_\chi + m_e}{E_\chi} \sqrt{\frac{E_e}{E_e + 2m_e}}, \quad (5.10)$$

where  $m_e$  is electron mass,  $E_e$  is the kinetic energy of the scattered electron, and  $E_\chi$  is the DM energy. For high incoming particle energies of several GeV and small angle limit,  $E_e\theta_e^2$  is small. This kinematic property of the scattered electron with small  $E_e\theta_e^2$  shows the "forwardness" in the beam direction and can be used as an important signal selection criterion in this analysis. Therefore, the signal we are looking for is the single forward-going electromagnetic (EM) showers.

The main background, consisting of true EM showers, coming from neutrino-electron elastic scatterings (denoted as  $\nu$ - $e$ ), mainly from the muon-neutrino neutral current ( $\nu_\mu$ -NC), electron-neutrino neutral current ( $\nu_e$ -NC), and electron-neutrino charged current ( $\nu_e$ -CC) processes. Because of similar two-body collision kinematics, the  $\nu$ - $e$  processes also leave single, very forward-going electron shower but with  $E\theta^2$  peaking around zero. In  $\nu$ - $e$  analysis, the typical region of interest is  $E\theta^2 < 0.005$ .

DM particles have higher mass than electrons. The typical energy of DM particle distributes from few GeV up to several tens of GeV and peaks around 10 GeV, whereas the maximum energy of neutrino is around 2 GeV. Thus, the recoil energy of electrons scattering off the DM particles of higher energy will be more than that of electrons energy scattering off the neutrinos. We have extended our interested energy region to incorporate higher  $E_e\theta_e^2$  values than in  $\nu - e$  analysis. FIG. 5.2 shows a sample of comparison between the background and the signal patterns in the  $E\theta^2$  space.

Besides the main background, there are also background consisting of other beam-related events, such  $\nu_\mu$ -CC events or meson exchange current (MEC) events. Those backgrounds can be significantly suppressed with well-defined event selection criteria.

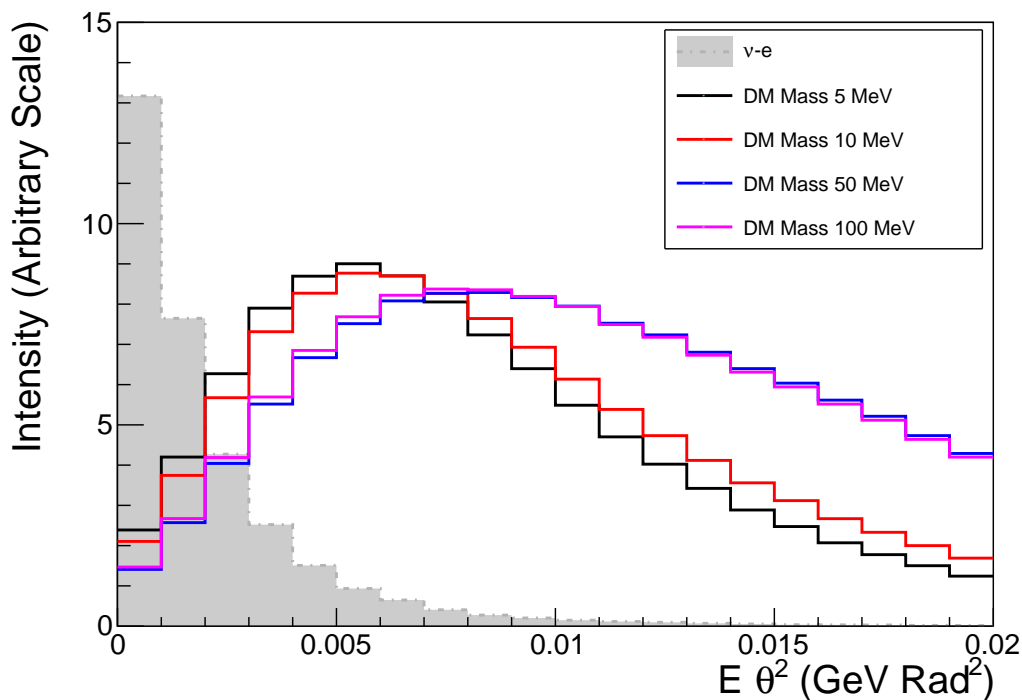


Figure 5.2: Signal and background pattern in  $E\theta^2$  space. Only the  $\nu$ - $e$  background is plotted in this figure. In the high  $E\theta^2$  region, other beam-related backgrounds start to dominate the total background, as shown in FIG. 5.3

### 5.1.4 Data Analysis

A **raster scan** is performed to search for light DM signal in the  $(Y, m_\chi)$  space [83]. In the 2D parameter space, we search over the physically interesting range of DM masses  $m_\chi$  from 5 to 200 MeV. At each possible DM mass, we make separate decisions based on **template fits**.

The binned template consists of three components:

- $\chi$ - $e$  signal template, denoted as  $\mathcal{S}_{\chi-e}$ ,
- $\nu$ - $e$  background template, denoted as  $\mathcal{B}_{\nu-e}$ , and
- other beam-related background template, denoted as  $\mathcal{B}_{\text{other}}$ .

The linear combination of the three components with three free parameters (scale factors) constitutes the prediction  $\mathcal{P}_{m_\chi}$ :

$$\mathcal{P}_{m_\chi}(a, b, c) = a \cdot \mathcal{S}_{\chi-e} \otimes \mathcal{R}_{m_\chi} + b \cdot \mathcal{B}_{\nu-e} + c \cdot \mathcal{B}_{\nu_\mu}, \quad (5.11)$$

where the parameter  $a$ ,  $b$ , and  $c$ , accounting for the number of the signal or background events, can be obtained by fitting the template  $\mathcal{P}_{m_\chi}(a, b, c)$  to data.

For each value of  $m_\chi$ , a best-fit value is determined for  $a$  by minimizing the likelihood value  $\chi^2$  for the fit, which is calculated as a function of  $a$ . **Pull terms** are added to  $\chi^2$  for nuisance parameters addressing the systematic uncertainties. The final  $\chi_{\min}^2$  is obtained after minimization over all nuisance parameters included in the fit. The fit estimates the yield (number of events) that originate from each component.

The  $\Delta\chi^2$  for a DM mass  $m_\chi$  is calculated using the minimum value of each point and not the global minimum as:

$$\Delta\chi^2 \equiv \chi^2 - \chi_{\min}^2 = 2.71, 3.84, \text{ and } 6.63, \quad (5.12)$$

at 90% , 95% , and 99% confidence levels, respectively, for one degree of freedom. The 1D confidence interval in  $Y$  at that  $m_\chi$  is all points with a  $\Delta\chi^2$  within **2.71**. The confidence region in the  $(Y, m_\chi)$  plane is then the union of all these intervals.

We show a fit sample in FIG. 5.3, where  $m_\chi = 8$  MeV. The red dot represents the fake (Asimov) data while the backgrounds, the  $\nu$ - $e$  background, and the other beam-related background are stacked and filled with light and dark gray. The fit results are presented as a solid black line, while the minimum log-likelihood ratio for this fit is  $9.62 \times 10^{-6}$ . The magenta filled region shows the 90% confidence-limit solution as  $m_\chi = 8$  MeV,  $m_V = 24$  MeV, with  $Y = 7.94 \times 10^{-12}$ .

This analysis is performed on the near detector FHC data samples consisting of  $\sim 2.5 \times 10^{21}$  POT exposure. The data were recorded by the near detector from 2014 to 2020.

MC simulation is used to study the signal and background. The signal events in this analysis are the single EM showers from the single electrons scattered by DM particles. The background events include the irreducible background from the single EM showers produced by the neutrino-electron scattering and the reducible background from other beam-related interactions.

We use  $5.55 \times 10^{21}$  POT inclusive NOvA official near detector MC samples to produce the background pattern for the beam-related background events.

The beam-related background can be broken down by different channels contributing to neutrino on the nucleus background. The breakdown plots are shown in FIG. 5.4

We use  $1.48 \times 10^{23}$  POT NOvA official  $\nu$ - $e$  single MC samples to study the neutrino-electron scattering feature.

We generate the signal samples, i.e. single forward-going EM showers from  $\chi$ - $e$  process, in two steps:

1. Simulate the production of DM particles and DM-electron scattering signals using the BdNMC software [84] and
2. Simulate the NOvA detector response to the single electrons scattered by DM particles using `NOvASoft`. `NOvASoft` is a NOvA software written in C++ and built on

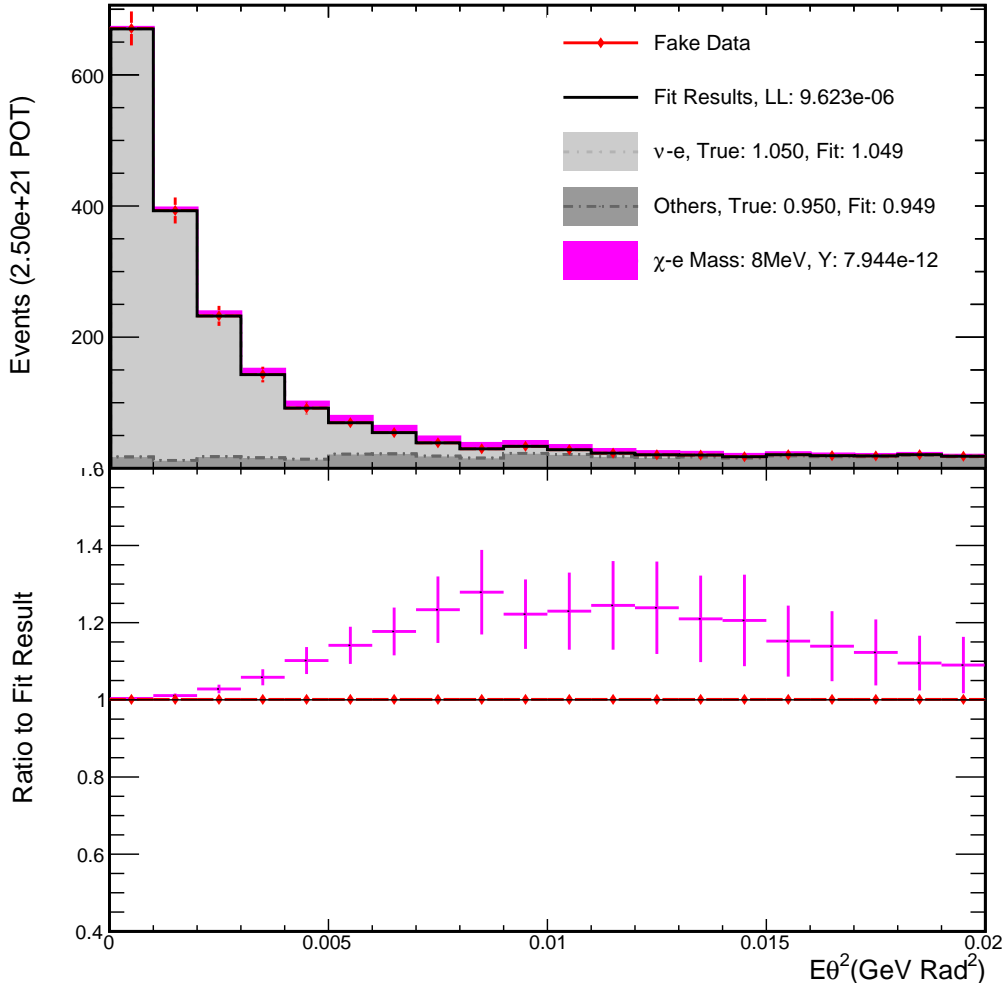


Figure 5.3: Fit sample. When producing the fake data, the parameters are configured as  $a = 0, b = 1.05, c = 0.95$ . For the fit, the DM mass is fixed as  $m_\chi = 8$  MeV.

ROOT analysis software.

The scattering single electrons produced by DM particles with different masses have different scattering energy and angle distributions. It will be inefficient to produce signal samples for each DM mass point. In this analysis, we do not make samples for individual DM masses in step 2, instead, we produce generic signal samples with `NOvASoft` and generate specific signal patterns for a DM mass point in two steps:

1. Generate single electrons samples following a “generic” energy distribution, denoted as Generic samples, and
2. Reweight the Generic samples according to a pre-trained ratio-histogram when filling signal histograms for specific DM mass points.

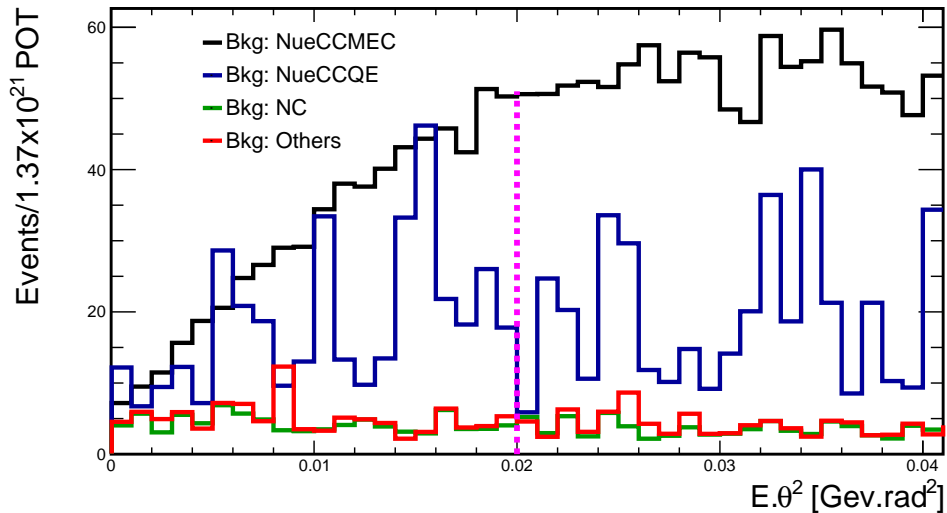


Figure 5.4: Beam related background: neutrino on nucleus.

The Generic samples are produced following the standard NOvA data simulation and reconstruction chain [85], and a signal template was built for the DM mass  $m_\chi$  by reweighting Generic samples.

### 5.1.5 Simulation of Signal Events

We simulate the Dark Matter (DM) particle production using the BdNMC software. The software is designed to simulate light-dark matter generation and downstream scattering at various fixed target experiments, and the BdNMC program is adaptable to different proton beam energy, production targets, and detector geometries. In addition, it supports four possible scattering interactions between Hidden Sector DM and the material in fixed-target neutrino detectors. The code in the software complies by taking the experimental setup provided in the **parameter.dat** file. For this analysis, the parameter file contains a list of parameters describing the desired run configuration specific to the NOvA experiment. Here, we have a sample of the parameter.dat file for the setup of the production and propagation of DM particles of a mass of 5 Mev.

```
#####
#Parameter specification for NOvA
model Dark_Photon
epsilon 1e-05
dark_matter_mass 0.005
dark_photon_mass 0.015
alpha_D 0.5
POT 1e21
pi0_per_POT 0.9
```

```

samplesize 5000000
burn_max 1000
burn_timeout 20000
beam_energy 120
n_num_target 6
p_num_target 6
output_mode comprehensive
production_channel pi0_decay
production_distribution bmpt
signal_channel NCE_electron
efficiency 1
min_scatter_energy 0
max_scatter_energy 120
min_scatter_angle 0.0
max_scatter_angle 6.29
detector cuboid
x-position 13.8
y-position -4.19
z-position 989.89
width 4.1
length 14.3
height 4.1
det-theta 0
det-phi 0
det-psi 0
material Liquid_Scintillator
number_density 5.16e22
proton_number 8
neutron_number 6
electron_number 8
mass 14.011
output_file Events/events-5.dat
summary_file Events/summary-5.dat
output_mode comprehensive
#####

```

Fixed target neutrino experiments produce neutrino beams when high-intensity proton beams collide with thick targets. Various secondary particles, including charged pions and kaons, are produced when protons interact with the nuclear material of the target. An extended decay volume facilitates these productions. The interactions of these neutrinos are detected due to the scattering of these neutrinos off nucleons and electrons. Additionally, this configuration offers the chance to look for light-dark matter particles, which can be created by neutral meson decay and have similar scattering signatures to neutrinos in the detector.

The target and proton beam interactions can produce  $\pi^0$ , which then radiatively decay to produce the intermediate particle  $V$ 's that rapidly decay to a pair of dark matter particles. The sequence of decays happens inside the target, and since this happens on a short enough time scale, we may presume that the initial pi and, fre-

quently, the intermediate  $V$  do not spread very far before decaying. After that, the dark matter particles travel in straight lines. Some particles collide and scatter inside the neutrino detector, creating a detectable signal. The number of scattered electrons is linearly correlated to the number DM particles and is scaled by parameter  $Y$ . Based on the parameters defined in the configuration, the MC simulation predicts the total number of scattered electrons, scattering angle, recoil energy, vertex, and time of the scattered electron generation in the detector.

This analysis has considered and simulated the light DM production via  $\pi^0$ -decay,  $\eta$ -decay, and proton bremsstrahlung processes. The values of the key parameters used for light DM production simulation, such as  $Y$ , beam (proton) energy, POT,  $\pi_0$  per POT, and the NOvA near detector parameters, are listed in TABLE 5.1. We use the value  $1/30$  for meson per  $\pi_0$  to account for other non- $\pi_0$  mesons, such that  $N_{\pi_0} \approx 30N_\eta$ .

Table 5.1: Parameters used for light DM production simulation in **BdNMC** software.

|                                       |            |              |             |                      |                 |
|---------------------------------------|------------|--------------|-------------|----------------------|-----------------|
| $\epsilon$                            | $\alpha_D$ | $m_\chi/m_V$ | Beam Energy | POT                  | $\pi_0$ per POT |
| $1 \times 10^{-3}$                    | 0.5        | 1/3          | 120 GeV     | $1.0 \times 10^{21}$ | 0.9             |
| NOvA Near Detector Parameters (meter) |            |              |             |                      |                 |
| Position to Beam (x, y, z)            |            |              | Width       | Length               | Height          |
| (13.8, -4.19, 989.89)                 |            |              | 4.1         | 14.3                 | 4.1             |

Approximately 496 DM mass points starting from 5 to 500 MeV were simulated with **BdNMC** software to forecast the mean energy, mean scattering angle, and the probable number of electrons produced by DM particles for various DM mass  $m_\chi$  in the NOvA near detector. The distributions of the above-predicted values are shown in FIG. 5.5. The predicted signal events from **BdNMC** estimate the total number of signal events that the experiment would observe, given a specific amount of POT. The total signal number is required to determine an experiment’s discovery potential for a novel physics scenario.

The electrons scattered by DM particles with different masses have different distributions of recoil energy and scattering angles, indicating that DM particles with different masses have different patterns of electron- $E\theta^2$  distribution patterns. In FIG 5.6, samples of the electron recoil energy and scattering angle distributions are shown. The “generic” distributions of the recoil energy and scattering angle of the electrons are used as the input of **NOvASoft** to produce single electron events and then simulate the detector response to those events.

A “generic” energy distribution was plotted to draw an envelope over all the energy

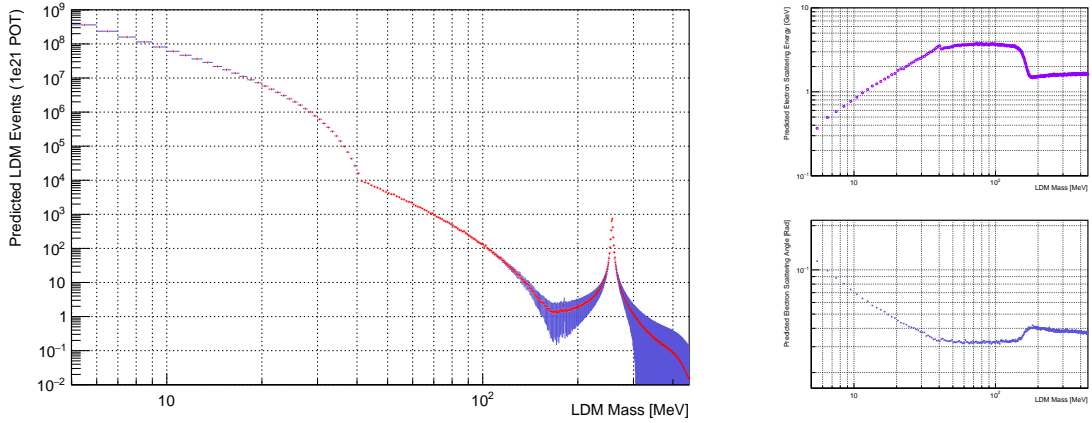


Figure 5.5: This figure shows the number of single electrons (on the left), the mean scattering energy, and angle (the two on the right) might be produced by DM particles with different masses. These plots are generated using parameters configured as:  $\alpha_D = 0.5$ ,  $\epsilon^4 \alpha_D = 5 \times 10^{-13}$ ,  $m_\chi/m_V = 1/3$  and  $\text{POT} = 1.0 \times 10^{21}$ .

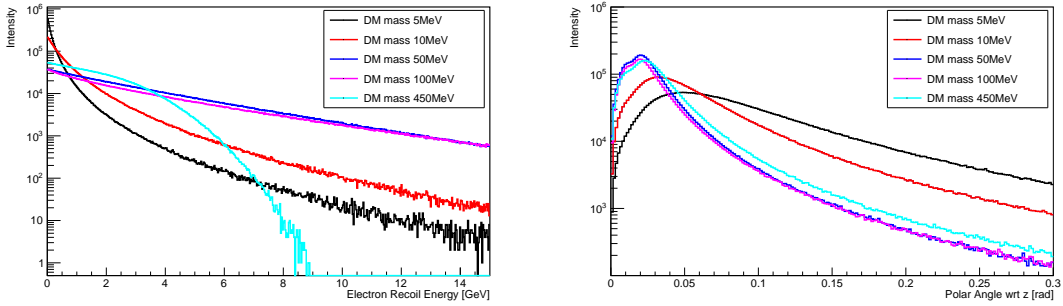


Figure 5.6: The figures show the recoil energy and scattering angle spectra of the electrons scattered by DM particles with mass 5, 10, 50, 100, and 450 MeV.

distributions. A generic energy distribution for 5 specific mass points is shown on the left of FIG. 5.7. At a given electron scattering energy, the scattering angle follows a similar correlation regardless of the DM mass. The comparison is shown clearly in FIG. 5.8. In the low energy region, the scattering angles show a double-peak feature in the distribution, which is caused by the off-axis nature of the NOvA near detector breaking the symmetry between the scattering of the electron closer to the beam direction than the electron away from the beam direction.

To simulate single electron events, a NOvASoft module (`SingleElectronGen_module`) was generated. The standard simulation and reconstruction chain of the NOvA experiment was followed to simulate the detector response and reconstruction of the single EM showers to produce the “Generic” signal samples. We have produced  $1.25524 \times 10^6$

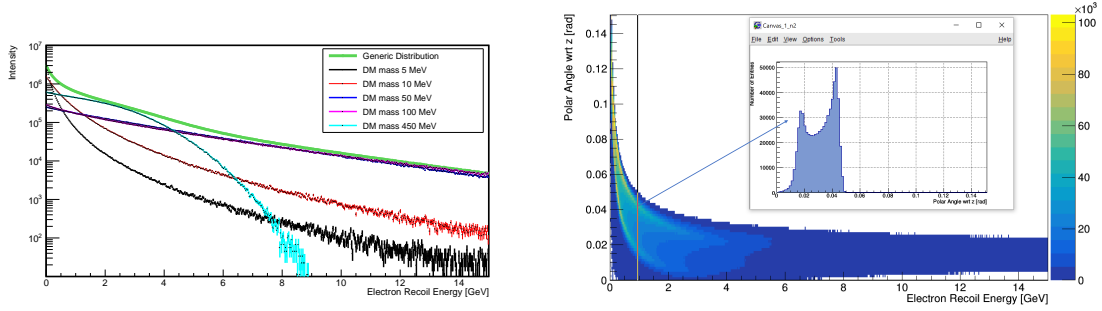


Figure 5.7: The generic energy distribution of the single electrons scattered by DM particles (left) and the correlation between the electrons’ recoil energy and the scattering angle (right). The green curve in the left figure is the so-called generic energy distribution. The small right figure shows the scattering angles’ distribution at 1 GeV recoil energy slice.

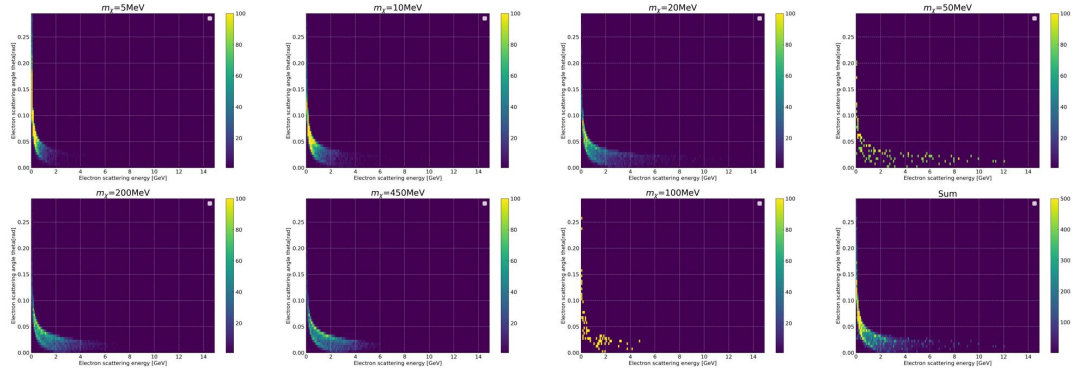


Figure 5.8: The correlation between the recoil energy and the scattering angle does not depend on the mass of the DM particles.

Generic signal samples.

For the generic samples to produce a specific signal pattern for a particular dark matter mass of  $m_\chi$ , a weight is assigned to each event from the corresponding ratio histogram. This assignment is solely dependent on its shower energy. A sample ratio histogram for DM mass points 5, 10, 50, 100, and 450 MeV are shown in FIG. 5.9

In Fig. 5.10, comparisons between the reweighted distributions and the “true” distributions are shown for four different DM mass points (5, 10, 20, 100 MeV). The plot indicates that the reweighting procedure accurately reproduces the single electron energy and angle distributions.

The number of single electron events linearly correlates to the POT or the parameter  $\epsilon^2 Y$ . In this work, we produce distinct DM signals without blending them with other neutrino interactions or interactions with rock.

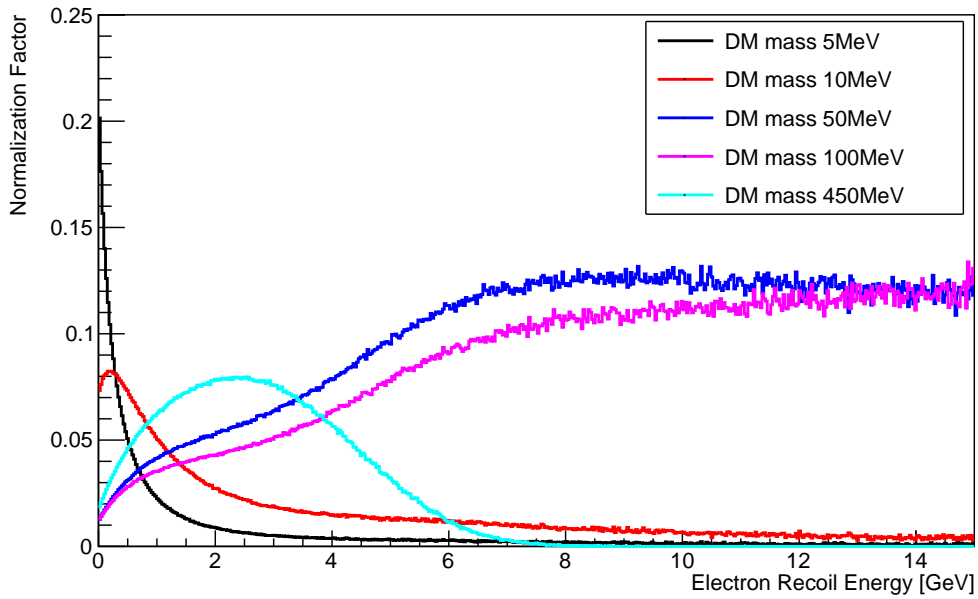


Figure 5.9: The bin-by-bin ratio between the the two histograms: the generic energy distribution (green curve in the left figure of FIG. 5.7) and the specific energy distribution for a specific DM mass (curve with corresponding color).

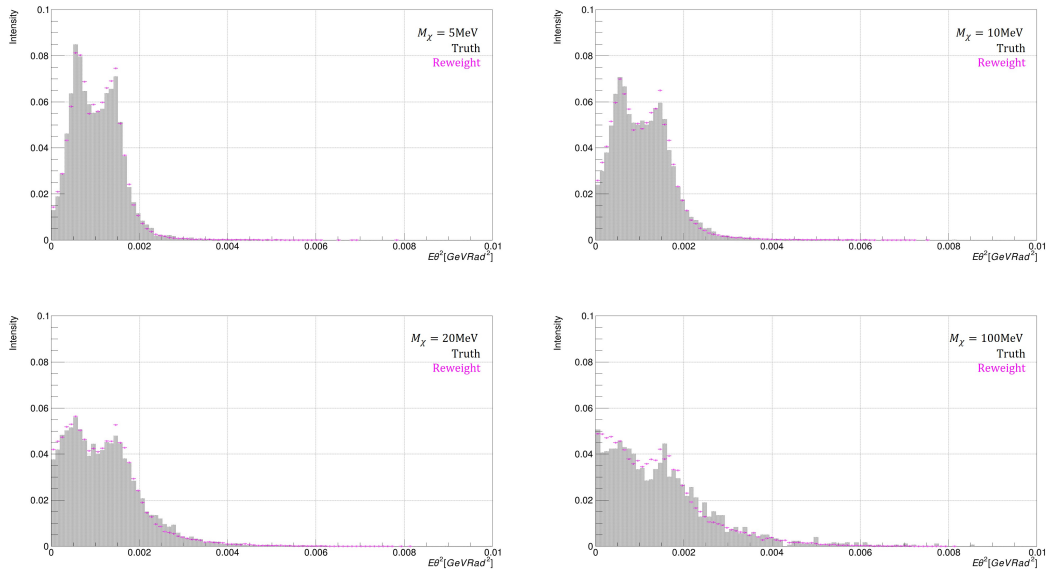


Figure 5.10: A comparison of the  $E\theta^2$  spectra between samples reweighted from the generic sample and the “true” distributions generated directly by BdMNC for four different DM mass points (5, 10, 20, 100 MeV).

### 5.1.6 Single Electron Event Selections and Cuts

In this section, our objective is to identify individual electron occurrences from the NOvA near detector data. Light DM particles have the capability to undergo elastic scattering off electrons, resulting in a single electromagnetic shower aligned along the beam direction. The signal signature resembles those of single electrons generated by the  $\nu$ - $e$  process. We fine-tune the cuts from  $\nu$ - $e$  analysis to retain a maximum number of single electron events while minimizing the presence of background originating from the beam. We treat the single electrons originating from the  $\nu$ - $e$  interaction during this optimization process as the “signal”.

The **preselection** criteria, aimed at eliminating obvious  $\nu_\mu$ -CC interactions within the detector, are as follows:

- $L < 800$  cm, where  $L$  represents the length of the longest prong.
- $N_{\text{plane}} < 120$ , where  $N_{\text{plane}}$  indicates the number of planes of the longest prong.
- $N_{\text{cell}} < 600$ , where  $N_{\text{cell}}$  denotes the total number of cells in a slice.

The **fiducialization and containment** constraints, designed to reduce backgrounds induced by neutrino interactions with the rock and ensure event interactions occur within the internal volume of the NOvA near detector, are defined by:

- Fiducial Cuts
  - Minimum  $X > -190$  and Maximum  $X < 180$
  - Minimum  $Y > -180$  and Maximum  $Y < 190$
  - Minimum  $Z > 105$  and Maximum  $Z < 1275$
- Containment Cuts
  - $-185 < X < 175$
  - $-175 < Y < 175$
  - $-90 < Z < 1095$

These constraints are applied to the  $X$ ,  $Y$ , and  $Z$  positions of hits on prongs within a slice.

The **single particle requirement** criteria, ensuring that the selected events involve a single particle, consist of:

- A requirement that the ratio of cell energies contained by the primary shower  $E_{\text{shower}}/E_{\text{total}} > 0.8$ , where  $E_{\text{shower}}$  represents the most energetic shower energy and  $E_{\text{total}}$  signifies the total energy of the slice.
- A condition that the Vertex Energy  $< 0.02$  GeV, where the Vertex Energy is the sum of cell energies above thresholds, excluding the leading shower, within  $\pm 8$  planes of the event vertex.
- A stipulation that the Shower Gap  $< 20$  cm, where the Shower Gap denotes the distance between the start point of the primary shower and the event vertex.

A **primary shower energy** requirement, targeting electron candidates with specific shower energy, is set as:

- $0.5 < E_{\text{shower}}/\text{GeV} < 5$ .

Two **particle ID** thresholds are employed to select single electrons and further reject background. The optimized values from  $\nu$ - $e$  analysis are:

- NuoneID  $> 0.73$
- Epi0ID  $> 0.92$

These classifiers are based on convolutional neural networks trained to identify  $\nu$ - $e$  elastic scattering events (NuoneID) and background with  $\pi^0$  in the final state (Epi0ID).

In event selection for signal and background analysis, a “cut flow” is a systematic presentation of how the selection criteria are applied sequentially to the data sample. This is often done to illustrate the impact of each cut on the number of remaining events. The efficiency of each cut, denoted as  $\epsilon^{N-1}$ , represents the fraction of events passing that particular cut among events that passed all previous cuts. The cumulative efficiency of each cut, denoted as  $\epsilon$ , represents the fraction of events passing that cut and all previous cuts among the initial number of events.

In data analysis, particularly in experimental physics, one aims to optimize the selection criteria (cuts) to enhance the experiment’s sensitivity to the phenomenon of interest. Maximizing the figure of merit (FOM) for each cut with other cuts applied, often called the “N-1 distribution,” is a systematic method for achieving this optimization. The figure of merit (FOM) improves each cut during  $\nu$ - $e$  analysis. In the  $\nu$ - $e$  analysis,  $S/\sqrt{S+B+\delta B^2}$  is the FOM utilized, where S and B are the numbers of signal (single EM shower), and background (beam-related) events, respectively,

Table 5.2: Cut flow for MC  $\chi$ - $e$  signal,  $\nu$ - $e$  background and nominal NuMI background events.

| Cut                         | $N_{\chi-e}$ | $\epsilon_{\chi-e}^{N-1}$ (%) | $\epsilon_{\chi-e}$ (%) | $N_{\nu-e}$ | $\epsilon_{\nu-e}$ (%) | $N_{\text{NuMI}}$ | $\epsilon_{\text{NuMI}}$ (%) |
|-----------------------------|--------------|-------------------------------|-------------------------|-------------|------------------------|-------------------|------------------------------|
| No Cut                      | 2386232      | 100                           | 100                     | 1979833     | 100                    | 1189874           | 100                          |
| Preselection                | 2385603      | 99.97                         | 99.97                   | 1979635     | 99.99                  | 997828            | 83.86                        |
| Fiducial and Containment    | 1685102      | 70.64                         | 70.62                   | 1118605     | 56.50                  | 272124            | 22.87                        |
| Single Particle Requirement | 1427833      | 84.73                         | 59.83                   | 908149      | 45.87                  | 65324             | 5.49                         |
| Primary Shower Energy       | 958348       | 67.12                         | 40.15                   | 600879      | 30.35                  | 17134             | 1.44                         |
| Particle ID                 | 643035       | 67.10                         | 16.11                   | 296974      | 15.00                  | 3212              | 0.27                         |

and  $\delta B^2$  is the systematic uncertainty in the background. In LDM analysis, we are required to consider DM particles with different masses. In this condition, the FOM for each variable is drawn using the generic  $\chi$ - $e$  samples to verify that the cuts defined in  $\nu$ - $e$  analysis are even though not optimum for each of the DM samples but are still making sense for  $\chi$ - $e$  analysis. The maxima of the FOMs are not utilized in this analysis to optimize the cuts. We have also plotted the distribution of FOMs for generic DM samples and also for specific DM particles of masses 5, 10, 50, and 100 MeV. We have compared the distribution of FOMs for DM particles with different masses to prove that similar cuts work for both generic and specific DM mass samples.

In FIG. 5.11, we show the distributions of some variables used for the event selection. The plots prove that the cuts defined using generic samples still work with specific samples, event though the spectra shifted a little when the DM particle mass varies.

We show some sample distributions in FIG. 5.12. Those figures are plotted with the FOMs for cuts used in preselection and particle ID and show the performance of the cut for  $\chi$ - $e$  event selection. The top 4 figures are plotted using the generic samples, while the bottom 4 figures are plotted using reweighted samples for DM particles with mass 5, 10, 50, and 100 MeV. It indicates that the cuts optimized based on generic samples also work reasonably for individual DM mass point. Note, here we consider the single electrons from  $\nu$ - $e$  process, together with the event from  $\chi$ - $e$  process, as signals.

By visualizing the angular distribution for different mass samples as in FIG. 5.13, we can effectively assess the selection efficiency of our cuts and gain insights into their impact:

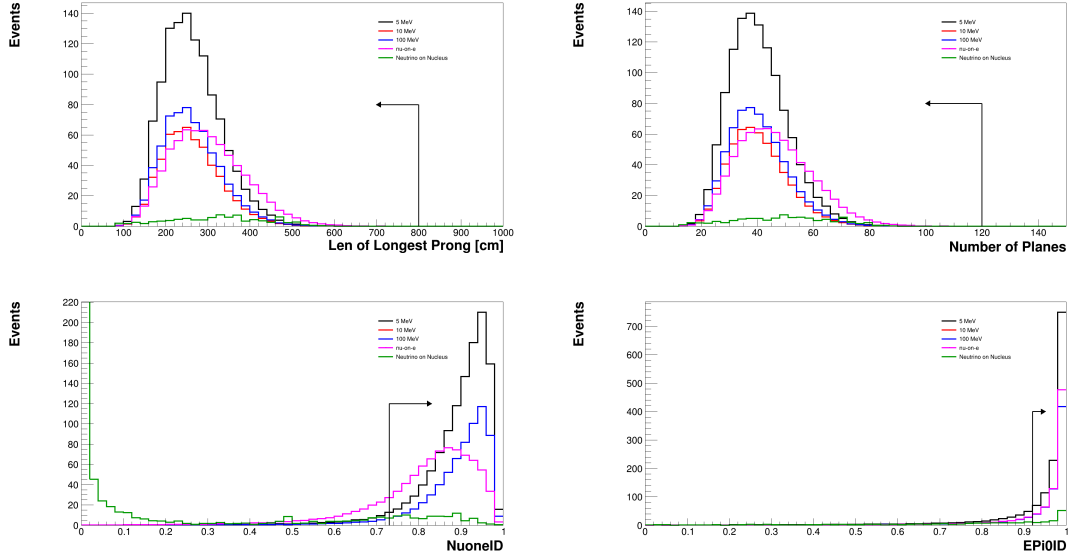


Figure 5.11: Sample distribution of the variables used for event selection for DM masses 5, 10, and 100 MeV along with  $\nu$ -on-e and Neutrino on the nucleus.

### 5.1.7 Systematic Uncertainties

The variation in the final results indicates potential mismodeling within the simulation. These differences in the final results could be due to the uncertainties associated with the beam flux, neutrino interactions, detector geometry and response, calibration, and reconstruction. Uncertainties associated with detector response and calibration require re-simulation with shifts being applied to various parameters that could have been mismodeled. Beam flux and neutrino interaction uncertainties can be accounted for by reweighting the final prediction without redoing the simulation. The largest uncertainty is related to the detector calibration. Calibration uncertainty arises due to imperfect modeling of our energy response at the end of cells in comparison to the center of the cells. Due to the aging of the detector scintillator, we also have detector response uncertainties, which can lower the average number of total hits in the cells over time and the response of the detector cells to the light. The statistical error related to the NOvA will reduce as the accumulation of data advances. In the LDM analysis, we come across various systematic uncertainties in the form of:

- Detector systematic uncertainties refer to uncertainties in the performance and calibration of the detector used in an experiment or measurement. These uncertainties can arise from various sources, including imperfect understanding of the detector response, calibration errors, and environmental effects. We have three

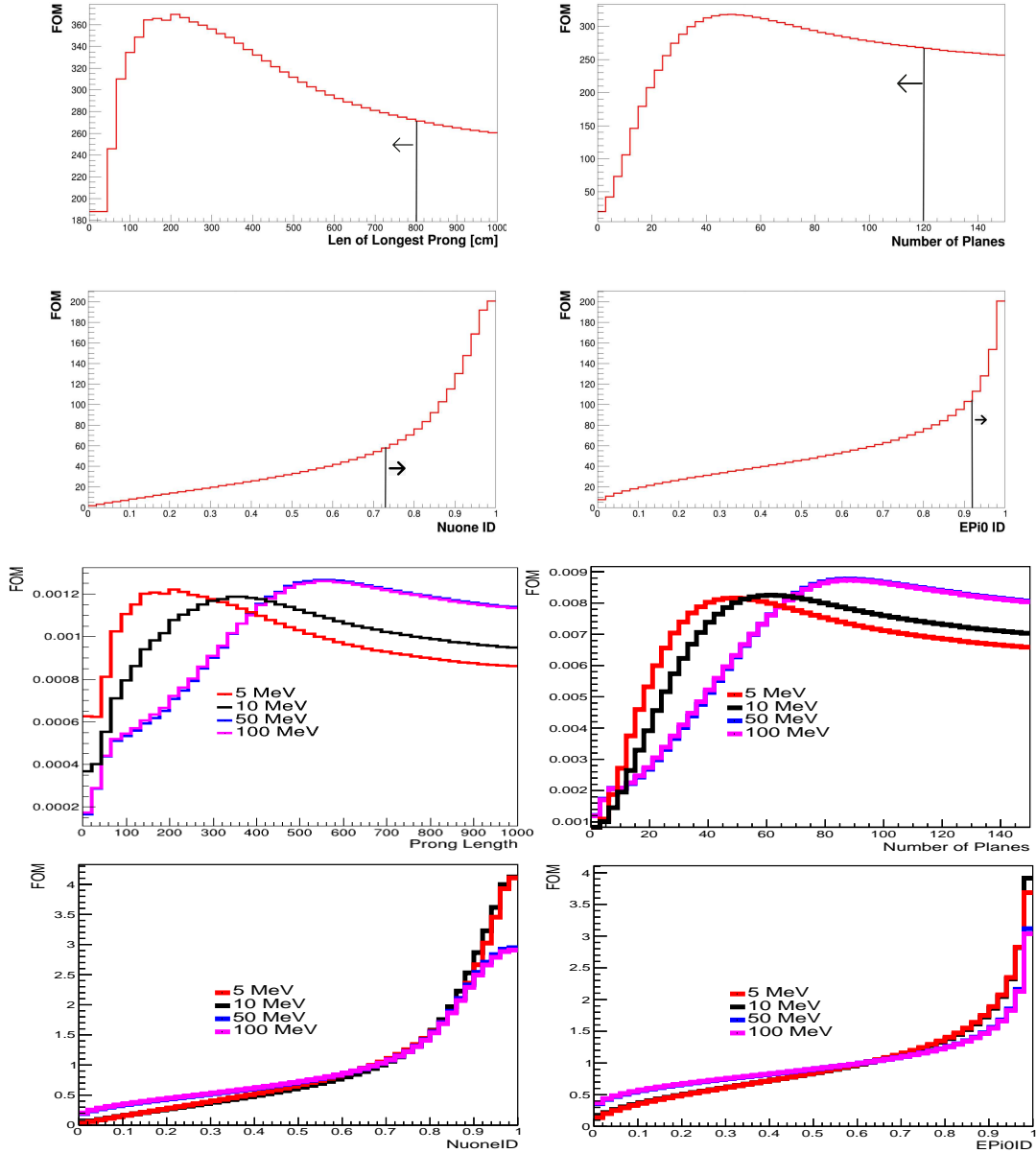


Figure 5.12: Sample plot showing FOMs for generic samples (top 4) and specific samples (bottom 4). We have used these plots to show that similar cuts work for both generic and specific DM mass samples.

template components for the detector’s systematic uncertainties, considering the NOvA near detector calibration, light level, and Cherenkov effects.

- Beam flux systematic uncertainties refer to uncertainties associated with the intensity and energy distribution of the particle beam in accelerator experiments. These uncertainties can arise due to factors such as beam intensity fluctuations, beam energy variations, and inaccuracies in beam monitoring systems. Beam

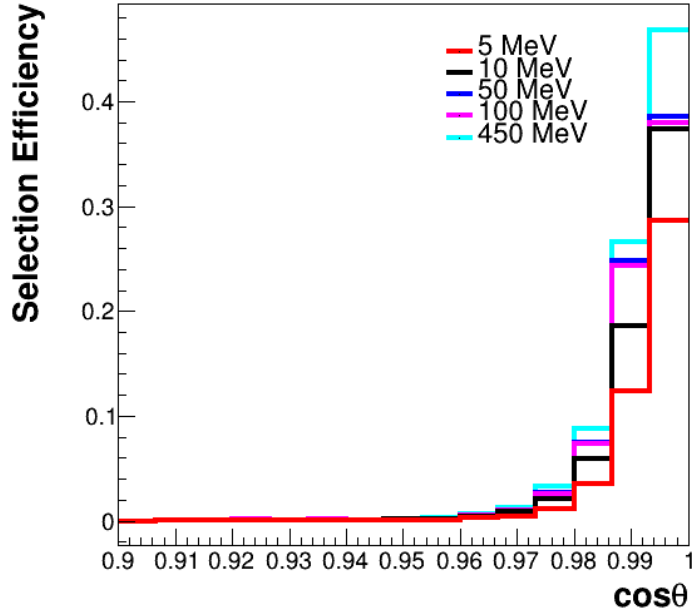


Figure 5.13: Selection efficiency of angular distribution for all the sample DM masses.

flux uncertainties are essential to consider because they directly impact the event rates and distributions observed in detectors, affecting the interpretation of experimental results. In NOvA, we have (`FluxPrincipalsND2020`), which are the PCA systematic uncertainties on the hadron production and beam focusing using a near detector-only covariance matrix. We use 7 PCs to cover the total flux error.

- Absolute normalization systematic uncertainties refer to uncertainties associated with the overall normalization of data or simulation in an experiment. These uncertainties can arise from factors such as uncertainties in the detector efficiency, trigger efficiency, or flux. In NOvA, We use (`NormSyst`), which is used to address the overall normalization and the ignorance of the overlay procedure when producing signal samples.
- Cross-section systematic uncertainties refer to uncertainties associated with measuring of a particle interaction cross-section in an experiment. We have retrieved the function `getAllXsecSysts_2020_GSF()` to count for all the latest NOvA cross-section-related systematic uncertainties.

We utilize the established NOvA systematic uncertainties framework to address

the systematic uncertainties. As for absolute normalization systematic uncertainties, we introduce a novel approach by implementing a new class called `NDPileupEffectSyst`. This new class is designed to adjust the spectrum by 10.6% for a  $1\sigma$  deviation.

Regarding the near detector systematic uncertainties, we predict the  $E\theta^2$  spectra shift due to the near detector systematics using the NOvA official detector systematics samples:

```
prod_flatsumdecaf_R20-11-25-prod5.1reco.a_nd_genie_N1810j0211a_nonswap_
fhc_NOvA_v08_full_v1_filematchedSystematics_nominal_v1,
```

```
prod_flatsumdecaf_R20-11-25-prod5.1reco.e_nd_genie_N1810j0211a_nonswap_
fhc_NOvA_v08_full_calibdown_v1_batch2_filematchedSystematics_calibdown_v1,
```

```
prod_flatsumdecaf_R20-11-25-prod5.1reco.e_nd_genie_N1810j0211a_nonswap_
fhc_NOvA_v08_full_calibup_v1_batch2_filematchedSystematics_calibup_v1.
```

```
prod_flatsumdecaf_R20-11-25-prod5.1reco.g_nd_genie_N1810j0211a_nonswap_fhc_
NOvA_v08_full_lightleveldown_v1_batch2_filematchedSystematics_
lightleveldown_v1,
```

```
prod_flatsumdecaf_R20-11-25-prod5.1reco.g_nd_genie_N1810j0211a_nonswap_fhc_
NOvA_v08_full_lightlevelup_v1_batch2_filematchedSystematics_
lightlevelup_v1.
```

and  $\nu$ -e detector systematics samples:

```
prod_caf_nd_genie_N1810j0211a_nonswap_fhc_NOvA_v08_full_v1_nuone_
overlay_filematch,
```

```
prod_caf_nd_genie_N1810j0211a_nonswap_fhc_NOvA_v08_full_v1_nuone_
overlay_filematch_calibdown,
```

```
prod_caf_nd_genie_N1810j0211a_nonswap_fhc_NOvA_v08_full_v1_nuone_
overlay_filematch_calibup.
```

```
prod_caf_nd_genie_N1810j0211a_nonswap_fhc_NOvA_v08_full_v1_nuone_
overlay_filematch_cvkdown,
```

```
prod_caf_nd_genie_N1810j0211a_nonswap_fhc_NOvA_v08_full_v1_nuone_
overlay_filematch_cvkup,
```

```
prod_caf_nd_genie_N1810j0211a_nonswap_fhc_NOvA_v08_full_v1_nuone_
overlay_filematch_lightleveldown,
```

```
prod_caf_nd_genie_N1810j0211a_nonswap_fhc_NOvA_v08_full_v1_nuone_
overlay_filematch_lightlevelup.
```

FIG. 5.14 shows the  $1\sigma$ -shifted  $\nu_\mu$ - $E\theta^2$  spectra due to the near detector systematics on the right plot and the ratio between the shifted spectra and the nominal spectrum is shown on the left. Similarly, FIG. 5.15 shows the  $1\sigma$ -shifted  $\nu$ -on- $e$   $E\theta^2$  spectra due to near detector systematics on the right and the ratio between the shifted and nominal spectra is shown on the left.

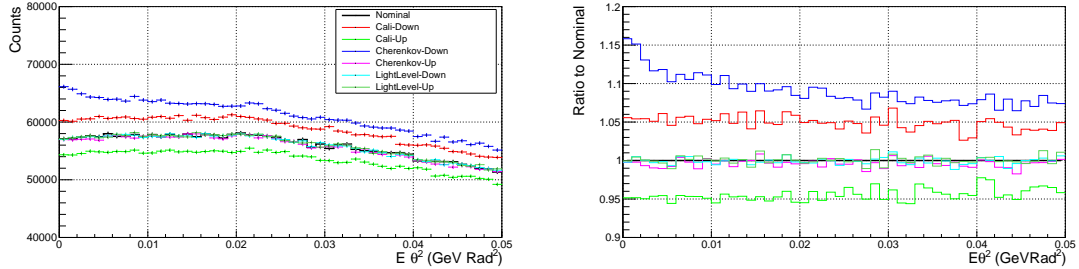


Figure 5.14: The  $E\theta^2$  spectrum shifts due to the systematic uncertainties of near detector for beam-related background events.

To predict the spectrum shifts for  $\chi$ - $e$  events, we produce  $\chi$ - $e$  detector systematics samples using the `fcls` similar to those for the  $\nu$ - $e$  systematics samples production. The ratios between the shifted and nominal spectra have been saved in the root files, which are then used for the fitting.

TABLE. 5.3 breaks down the statistical and systematic uncertainties on the confidence interval prediction for the measured DM mass points. The total uncertainty is the quadratic sum of the statistical and systematic uncertainties.

Figure 5.16 shows the impact on the  $E\theta^2$  templates due to near detector systematic uncertainties after selection cuts have been applied to the samples. Other system-

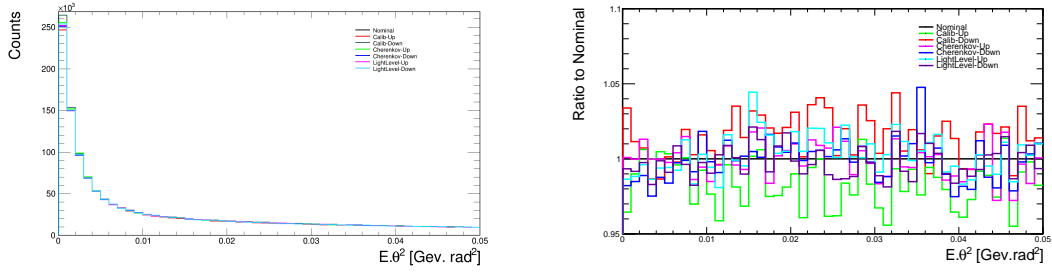


Figure 5.15: The  $E\theta^2$  spectrum shifts due to the systematic uncertainties of near detector for  $\nu$ -on-e events.

Table 5.3: Impacts of the systematic uncertainties on the 90% confidence level sensitivity measurement (%) as a function of DM mass  $m_\chi$ . Note that this table shows that the impact from Flux and Cross Section uncertainties are almost identical and indistinguishable.

| $m_\chi$ (MeV) | Systematic |      |                |               |          | total |
|----------------|------------|------|----------------|---------------|----------|-------|
|                | Detector   | Flux | Overlay Effect | Cross Section | Quad Sum |       |
| 5              | 11.52      | 7.08 | 8.95           | 7.08          | 17.69    | 14.63 |
| 6              | 11.66      | 7.26 | 9.49           | 7.26          | 18.20    | 15.09 |
| 7              | 11.83      | 7.34 | 9.90           | 7.34          | 18.60    | 15.58 |
| 8              | 12.02      | 7.52 | 10.44          | 7.52          | 19.15    | 16.19 |
| 9              | 12.22      | 7.66 | 10.92          | 7.66          | 19.65    | 16.75 |
| 10             | 12.40      | 7.77 | 11.30          | 7.77          | 20.05    | 17.37 |
| 20             | 14.17      | 8.81 | 13.82          | 8.81          | 23.38    | 22.23 |
| 30             | 14.95      | 9.14 | 14.65          | 9.14          | 24.60    | 23.23 |
| 40             | 14.51      | 9.15 | 14.89          | 9.15          | 24.48    | 23.45 |
| 50             | 14.27      | 9.09 | 14.87          | 9.09          | 24.29    | 23.43 |
| 60             | 14.38      | 9.05 | 14.85          | 9.05          | 24.31    | 23.44 |
| 70             | 14.41      | 9.10 | 14.89          | 9.10          | 24.33    | 23.46 |
| 80             | 14.42      | 9.04 | 14.86          | 9.04          | 24.33    | 23.45 |
| 90             | 14.49      | 9.12 | 14.89          | 9.12          | 24.46    | 23.47 |
| 100            | 14.49      | 9.12 | 14.88          | 9.12          | 24.45    | 23.45 |
| 200            | 13.84      | 8.84 | 13.89          | 8.84          | 23.26    | 22.22 |
| 300            | 14.06      | 8.94 | 14.15          | 8.94          | 23.62    | 22.61 |

atic uncertainties (beam flux, absolute normalization, and cross-section systematic uncertainties) have little impact on the shape of the spectra.

### 5.1.8 Results

After the systematic uncertainty study and inclusion, we scan the DM mass parameter space to validate the sensitivity of the NOvA experiment. This analysis has scanned

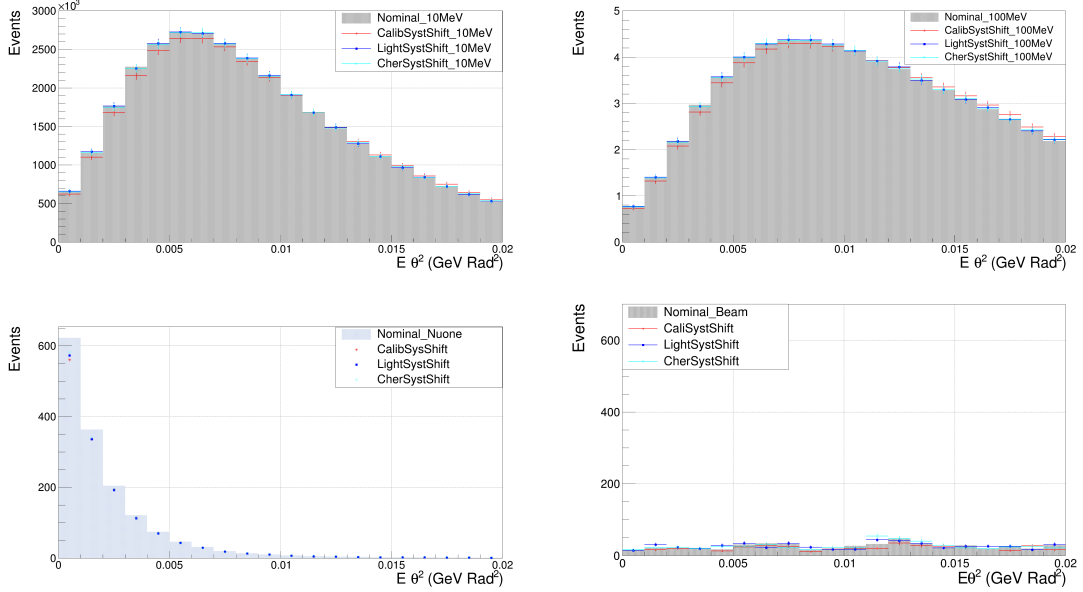


Figure 5.16: The  $E\theta^2$  spectrum shifts due to the systematic uncertainties of near detector for 10 MeV LDM signal (top left), 100 MeV LDM signal (top right),  $\nu$ - $e$  scattering background events (bottom left), and beam-related background events (bottom right).

the DM mass parameter space for  $5 < m_\chi < 200$  MeV window to generate 2D confidence limits.

The cut flow, has been applied to the MC samples to create fit templates. The  $\nu$ - $e$  background samples are weighted by `kPPFXFluxCVWgt` and radiative correction `kRadWt` and beam-related background samples are weighted by `kPPFXFluxCVWgt` and `kXSecCVWgt2020GSFProd51`.

As discussed in the analysis overview section, a raster scan is performed over the concerned DM mass window and template fits are performed separately for each concerned DM mass point. The template fit gives the best fit value of  $a_{\text{fit}}$  of  $\chi$ - $e$  signal components. The parameter  $Y_{\text{fit}}$  from the template fit can be derived as:

$$Y_{\text{fit}} = \sqrt{a_{\text{fit}} \times \epsilon_{\text{ref}}^4 \times \alpha_D \left( \frac{m_\chi}{m_V} \right)^4}. \quad (5.13)$$

In this work, we proposed to estimate the sensitivity [86] assuming we will have data with near detector exposure of  $2.5 \times 10^{21}$  POT. If we don't have so much data due to production or data quality, we perform fit with less data ( $1.25 \times 10^{21}$  POT) to estimate the NOvA sensitivity to light dark matter mass. In addition, after we got the NOvA measurement on meson per POT and the precise detector material

composition, we updated the detector sensitivity. For the DM parameter slice  $m_V = 3m_\chi$  and  $\alpha_D = 1/2$ , the limit (sensitivity) set by NOvA experiment, illustrated in FIG. 5.17, has been compared to the DM annihilation cross section and in turn the thermal relic abundance, and the confidence level results from other experiments: Babar [72], LSND [87, 88], E137 [89], NA64 [90], MiniBooNE [91], and COHERENT [92] as well.

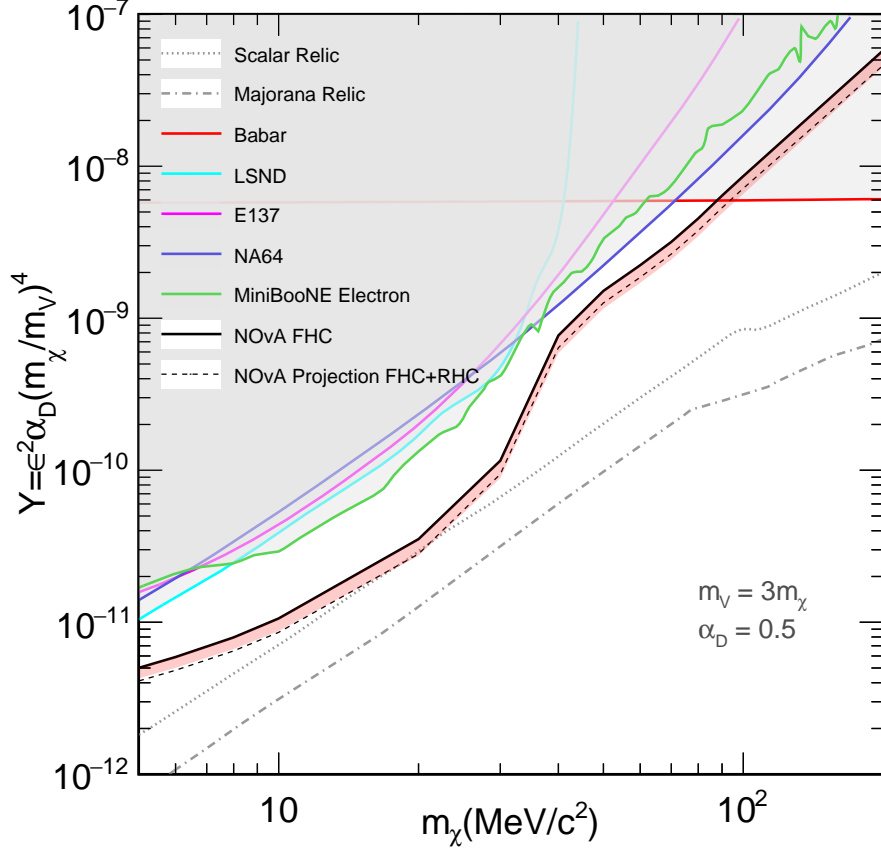


Figure 5.17:

Comparison of NOvA sensitivity to other experiments for  $Y$  as a function of  $m_\chi$ , assuming  $\alpha_D = 0.5$  and  $m_V = 3m_\chi$ . The solid line is the sensitivity drawn from the analysis of neutrino data. The dashed line shows the estimated projection if we combine the neutrino and anti-neutrino in the analysis. The region filled with light red covers the systematic uncertainty of this measurement

We also try to estimate the NOvA sensitivity if we can do an analysis using both neutrino and anti-neutrino data. As we don't have available anti-neutrino MC samples for  $\nu$ - $e$  background, we build fake data using FHC  $\nu$ - $e$  background samples

with a smaller scale factor (0.90) and RHC other beam-related background samples with a bigger scale factor (1.05), and then we use the FHC  $\nu$ - $e$  background samples to construct the  $\nu$ - $e$  template. It will improve the NOvA sensitivity by  $\sim 20\%$ .

# Chapter 6

## Non-Standard Interactions in Long-baseline Neutrino Experiments

Accelerator-based neutrino experiments provide exciting opportunities to delve into the mysteries of neutrino physics. These long-baseline neutrino experiments enable the study of neutrinos. These studies shed light on the fundamental aspects of particle physics and potentially uncover new physics beyond the standard model (BSM). Neutrinos travel a few hundred kilometers and are detected far away from the source. They also change their flavor while going from one place to another and mixing among the various mass eigenstates. Neutrino oscillations offer a compelling indirect signature of physics beyond the standard model. This phenomenon has led to extensive research and speculation about the nature of neutrinos and the possibility of new physics phenomena. When neutrinos traverse through the Earth's atmosphere, the Wolfenstein matter effect significantly influences neutrinos. Wolfenstein introduced non-standard interactions (NSI) [59] to explore potential new physics beyond the standard model. These NSIs can modify neutrino interactions with matter and produce observable effects in neutrino experiments. The extensive study of NSI from a phenomenological perspective can open many windows into the BSM realm. Extensive studies in neutrino oscillation phenomenology [25, 93, 94, 95, 96, 97, 98, 99, 100] including NSI, have contributed to our understanding of these intriguing particles.

### 6.1 Analysis Overview

NSI affects standard neutrino oscillation in matter [101, 102, 103, 104, 105, 106, 107]. This work assumes that new physics arises only from the NSI and is responsible for any deviation from the standard physics model. NSI generally affects neutrino propagation in

matter through neutral-current and charged-current interactions. The standard model (SM) CP phase promises to help us understand the baryon asymmetry of the universe and is the most sought-after observable in the currently running and future neutrino experiments. The most recent results from the two long-baseline accelerator experiments, NO $\nu$ A [108, 109] and T2K [110, 111], show some tension in the standard 3-flavor scenario. The CP phase preferred by NO $\nu$ A is close to  $\delta_{CP} \approx 0.8\pi$  whereas T2K hints at a value of  $\delta_{CP}$  around  $1.5\pi$  in the case of normal ordering (NO). In the case of inverted ordering (IO), there appears to be no disagreement. Once the NSI from the  $e - \mu$  sector is considered, the tension concerning the  $\delta_{CP}$  parameter for NO $\nu$ A and T2K becomes placid [112, 113], but one can see a difference for  $\theta_{23}$ . NO $\nu$ A prefers a lower octant, whereas T2K prefers a higher octant. We extracted datasets of NO $\nu$ A and T2K from the recent data release to find the constraints on NSI contributions. We use the same coefficients to see if we can get any discernible result in future long-baseline (LBL) neutrino experiments, such as the DUNE and T2HK. The objective here is to determine whether or not the degeneracy for the standard model parameter  $\theta_{23}$  persists in the presence of NSI arising from both  $e - \mu$  and  $e - \tau$  sectors for DUNE and T2HK.

### 6.1.1 Parameterization of NSI

A four-fermion effective lagrangian describes the Standard model interactions involving neutrinos as:

$$\mathcal{L}_{eff} = -2\sqrt{2}G_F([\bar{\nu}_\alpha\gamma_\rho Ll_\alpha][\bar{f}\gamma^\rho Lf'] + h.c.) - 2\sqrt{2}G_F \sum_{P,f,\alpha} g_P^f [\bar{\nu}_\alpha\gamma_\rho L\nu_\alpha][\bar{f}\gamma^\rho Pf], \quad (6.1)$$

where  $G_F$  is the Fermi coupling constant,  $P = L, R$  indicates the chirality operator,  $L, R = (1 - \gamma^5)/2$ ,  $l_\alpha$  denotes the charged lepton of flavor  $\alpha(e, \nu, \tau)$ ,  $f, f'$  corresponds to the matter fermions and  $g_P^f$  is the weak neutral current couplings. The first term, as given in eq. 6.1 corresponds to charged-current weak interaction, which is mediated by  $W$  boson; the second term is for neutral current weak interactions that are mediated by  $Z$  boson. When Non-standard interactions are introduced, these extra interactions are parametrized by new couplings  $\epsilon$ . For Charged-current weak interactions, the lagrangian is given by:

$$\mathcal{L}_{eff} = -2\sqrt{2}G_F \sum_{f,f',P} \epsilon_{\alpha\beta}^{CC,f,f',P} [\bar{\nu}_\alpha\gamma_\rho Ll_\beta][\bar{f}\gamma^\rho Pf'], \quad (6.2)$$

And the neutral-current weak interactions by:

$$\mathcal{L}_{eff} = -2\sqrt{2}G_F \sum_{P,f} \epsilon_{\alpha\beta}^{f,P} [\bar{\nu}_\alpha\gamma_\rho L\nu_\beta][\bar{f}\gamma^\rho Pf], \quad (6.3)$$

where  $f = u, d, e$  denotes the matter fermions.

### 6.1.2 Formalism

The NSI can be characterized by six-dimensional four-fermion ( $ff$ ) operators of the form:

$$\mathcal{L}_{NSI} = 2\sqrt{2}G_F\epsilon_{\alpha\beta}^{fC}[\bar{\nu}_\alpha\gamma^\rho P_L\nu_\beta][\bar{f}\gamma_\rho P_C f] + h.c. \quad (6.4)$$

Where  $\alpha, \beta = e, \mu, \tau$  indicate the neutrino flavor, superscript  $C = L, R$  refers to the chirality of  $ff$  current,  $f = u, d, e$  denotes the matter fermions and  $\epsilon_{\alpha\beta}^{fC}$  are dimensionless parameters that measure the new interaction's strength concerning the SM.

When the neutrinos travel through the Earth, the propagating neutrinos undergo coherent forward scattering due to NSI. The effective Hamiltonian in the presence of matter, NSI, can be expressed with the addition of a new term to the standard oscillation Hamiltonian:

$$H_{Eff} = \frac{1}{2E} \left[ U_{PMNS} \begin{bmatrix} 0 & 0 & 0 \\ 0 & \Delta m_{21}^2 & 0 \\ 0 & 0 & \Delta m_{31}^2 \end{bmatrix} U_{PMNS}^\dagger + V \right] \quad (6.5)$$

where  $H_{Eff} \equiv H_{mat+NSI}$ .

$$H_{mat+NSI} = \frac{1}{2E} \left[ U_{PMNS} \begin{bmatrix} 0 & 0 & 0 \\ 0 & \Delta m_{21}^2 & 0 \\ 0 & 0 & \Delta m_{31}^2 \end{bmatrix} U_{PMNS}^\dagger + \sum_f V_f \left( \begin{bmatrix} \delta_{ef} + \epsilon_{ee}^f & \epsilon_{e\mu}^f & \epsilon_{e\tau}^f \\ \epsilon_{e\mu}^{f*} & \epsilon_{\mu\mu}^f & \epsilon_{\mu\tau}^f \\ \epsilon_{e\tau}^{f*} & \epsilon_{\mu\tau}^{f*} & \epsilon_{\tau\tau}^f \end{bmatrix} \right) \right] \quad (6.6)$$

$U_{PMNS}$  is the unitary Potecorvo-Maki-Nakagawa-Sakata mixing matrix (lepton mixing matrix),  $E$  is the neutrino energy and  $\Delta m_{21}^2 \equiv m_2^2 - m_1^2$ ,  $\Delta m_{31}^2 \equiv m_3^2 - m_1^2$ .  $m_1, m_2$  and  $m_3$  are the different mass eigenstates.  $V_f$  is written as:

$$V_f = 2\sqrt{2}G_F N_e E$$

$N_e$  is the number density of electrons, and for neutrino propagation in the Earth,  $\epsilon_{\alpha\beta} e^{i\phi_{\alpha\beta}} \equiv \sum_{f,C} \epsilon_{\alpha\beta}^{fC} \frac{N_f}{N_e} \equiv \sum_{f=e,u,d} (\epsilon_{\alpha\beta}^{fL} + \epsilon_{\alpha\beta}^{fR}) \frac{N_f}{N_e}$ ,  $N_f$  being the number density of  $f$  fermion. The  $\epsilon_{\alpha\beta}$  are real and  $\phi_{\alpha\beta} = 0$  for  $\alpha = \beta$ . We concentrate on flavour non-diagonal NSI ( $\epsilon_{\alpha\beta}$ 's with  $\alpha \neq \beta$ ). Here, we consider single NSI parameter  $\epsilon_{e\mu}$  or  $\epsilon_{e\tau}$  (one at a time) to examine the conversion probability of  $\nu_\mu \rightarrow \nu_e$  for the LBL studies which can be stated

as the sum of three (plus higher order; cubic and beyond) terms in the presence of NSI:

$$P_{\mu e} = P_0 + P_1 + P_2 + h.o. \quad (6.7)$$

the above Eq.(6.7), similar to [114] takes the following form:

$$P_0 = 4s_{13}^2 s_{23}^2 f^2 + 8s_{13}s_{23}s_{12}c_{12}c_{23}rfg \cos(\Delta + \delta_{CP}) + 4r^2 s_{12}^2 c_{12}^2 c_{23}^2 g^2$$

$$P_1 = 8\hat{A}\epsilon_{e\mu}[s_{13}s_{23}[s_{23}^2 f^2 \cos(\Psi_{e\mu}) + c_{23}^2 fg \cos(\Delta + \Psi_{e\mu})] + 8rs_{12}c_{12}c_{23}[c_{23}^2 g^2 \cos \Psi_{e\mu} + s_{23}^2 g \cos(\Delta - \phi_{e\mu})]]$$

and,

$$P_2 = 8\hat{A}\epsilon_{e\tau}[s_{13}c_{23}[s_{23}^2 f^2 \cos(\Psi_{e\tau}) - s_{23}^2 fg \cos(\Delta + \Psi_{e\tau})] - 8rs_{12}c_{12}s_{23}[c_{23}^2 g^2 \cos \Psi_{e\tau} - c_{23}^2 g \cos(\Delta - \phi_{e\tau})]]$$

where,  $f \equiv \frac{\sin[(1-\hat{A})\Delta]}{1-\hat{A}}$ ;  $g \equiv \frac{\sin \hat{A}\Delta}{\hat{A}}$ ;  $\hat{A} = \frac{2\sqrt{2}G_F N_e E}{\Delta m_{31}^2}$ ;  $\Delta = \frac{\Delta m_{31}^2 L}{4E}$ ;  $r = \frac{\Delta m_{21}^2}{\Delta m_{31}^2}$ . Furthermore, here we used:  $\Psi_{e\mu} = \phi_{e\mu} + \delta_{CP}$ ;  $\Psi_{e\tau} = \phi_{e\tau} + \delta_{CP}$ . The  $\phi_{e\mu}, \phi_{e\tau}$  are the non-standard CP phases corresponding to  $e - \mu$  and  $e - \tau$  sector.

### 6.1.3 Simulation Software

For the phenomenological study of the non-standard interactions, we used the software GLoBES (General Long Baseline Experiment Simulator) [115] and its additional public tool that can implement NSI. The extension enables the initialization of non-standard neutrino interactions and sterile neutrinos in GLoBES simulation. GLoBES enables the simulation of experiments with stationary neutrino point sources, assuming that there is only one neutrino source per experiment.

The best-fit values of the standard model parameters and their corresponding uncertainties are taken from nuFIT v5.1 [116] and PDG [117]. For example, the parameter values taken (for normal ordering) are:  $\sin^2 \theta_{12} = 0.304_{-0.012}^{+0.013}$ ;  $\sin^2 \theta_{23} = 0.573_{-0.023}^{+0.018}$ ;  $\sin^2 \theta_{13} = 0.02220_{-0.00062}^{+0.00068}$ ;  $\delta_{CP} = 194_{-25}^{+52}$ ;  $\frac{\Delta m_{21}^2}{10^{-5} eV^2} = 7.42_{-0.20}^{+0.21}$ ; and  $\frac{\Delta m_{3l}^2}{10^{-3} eV^2} = +2.517_{-0.028}^{+0.028}$ . To combine the extracted datasets of NOvA and T2K, We have utilized GLoBES. Using the obtained NSI constraints, we discuss the sensitivity of the CP-violating phase, the standard oscillation parameters, and the oscillation probabilities for the two next-generation LBL experiments: DUNE and T2HK. GLoBES uses AEDL (a comprehensive abstract experiment definition language) files that are available for simulating experiments like T2HK and DUNE. For this analysis, we used DUNE and T2HK running for 3.5 years and 3 years in  $\nu$  mode and 3.5 years and 4 years in  $\bar{\nu}$  mode, respectively.

For the simulation of DUNE and T2HK in GLoBES, we have considered a few specifications of the experiments. In the case of DUNE, we have considered that it will have a

40-kiloton liquid argon detector that will use a 1.2 MW proton beam to generate neutrino and antineutrino beams from in-flight pion decays. The proton beam will originate 1300 kilometers upstream at Fermilab. The neutrino energy ranges will be between 0.5 and 20 GeV, and the flux peak around 3.0 GeV. Meanwhile, the T2HK experiment will have a 225 kt water Cherenkov detector. It will use an upgraded 30 GeV J-PARC beam with a power of 1.3 MW, and its detector will be located 295 km away from the source.

### 6.1.4 Analysis Details

To study the effect of non-standard interactions on the neutrino oscillation parameters like  $\delta_{CP}$  and  $\theta_{23}$ , we will derive the constraints coming from the non-standard parameters magnitude and phase factor, i.e.,  $\epsilon_{e\mu}$ ,  $\epsilon_{e\tau}$ ,  $\phi_{e\mu}$  and  $\phi_{e\tau}$  [118].

To derive the constraints from the non-standard interactions, we scanned the allowed region in the plane that will be spanned by NSI magnitude arising from  $e - \mu$  sector in the presence of the standard CP-phase  $\delta_{CP}$  as well as the non-standard CP phase  $\phi_{e\mu}$ . In Fig. 6.1 (top panel), the constraint plots for the combination of T2K and NO $\nu$ A are displayed. The left panel shows the allowed region in the plane spanned by  $\epsilon_{e\mu}$  and the CP-phase  $\delta_{CP}$ , whereas the right panel displays the allowed region for  $\epsilon_{e\mu}$  and the NSI phase  $\phi_{e\mu}$ . For the left panel plot the non-standard CP-phase  $\phi_{e\mu}$ ,  $\theta_{23}$ , and  $\theta_{13}$  are marginalized away whereas on the right panel plot  $\theta_{23}$ ,  $\theta_{13}$ , and  $\delta_{CP}$  are marginalized. The similar plots for the IO case are displayed in the same Fig. 6.1 bottom panel.

Not just for the  $e - \mu$  sector, we have similar constraint plots for the  $e - \tau$  sector as well. Here in Fig 6.2, the allowed region in the plane that will be spanned by NSI magnitude arising from  $e - \tau$  sector in the presence of the standard CP-phase  $\delta_{CP}$  as well as the non-standard CP phase  $\phi_{e\tau}$  are plotted. The left panel of the Fig. 6.2 depicts the allowed region in the plane spanned by  $\epsilon_{e\tau}$  and the CP-phase  $\delta_{CP}$ , whereas the right panel displays the allowed region for  $\epsilon_{e\tau}$  and the NSI phase  $\phi_{e\tau}$ . In the left panel plot, the non-standard CP-phase  $\phi_{e\tau}$ ,  $\theta_{23}$ , and  $\theta_{13}$  are marginalized away whereas for the right plot  $\theta_{23}$ ,  $\theta_{13}$ , and  $\delta_{CP}$  are marginalized.

The plots in Figs. 6.1 and 6.2 are drawn for both the scenarios of NO as well as IO, and there is a clear preference for non-zero coupling values corresponding to  $|\epsilon_{e\mu}|$  and  $|\epsilon_{e\tau}|$  and their respective phases  $\phi_{e\mu}$  and  $\phi_{e\tau}$ . All the constraint best-fit values are listed in Table 6.1 along with the corresponding  $\chi^2$  values. These obtained NSI parameter values are consistent with the global constraints on neutral current NSI parameters [?]. We found  $\delta_{CP}$  value for  $e - \mu$  sector around  $1.12\pi$  (for NO case) as evident from the top left panel of Fig. 6.1. Interestingly, for  $e - \tau$  sector also we obtained similar value of  $\delta_{CP}$  (Fig. 6.2). For all the cases (SM, SM+NSI from  $e - \mu$  and  $e - \tau$  sectors), nuFIT v5.1 so that in this analysis, we are not being biased to any specific scenario but only to visualize the effect of NSI.

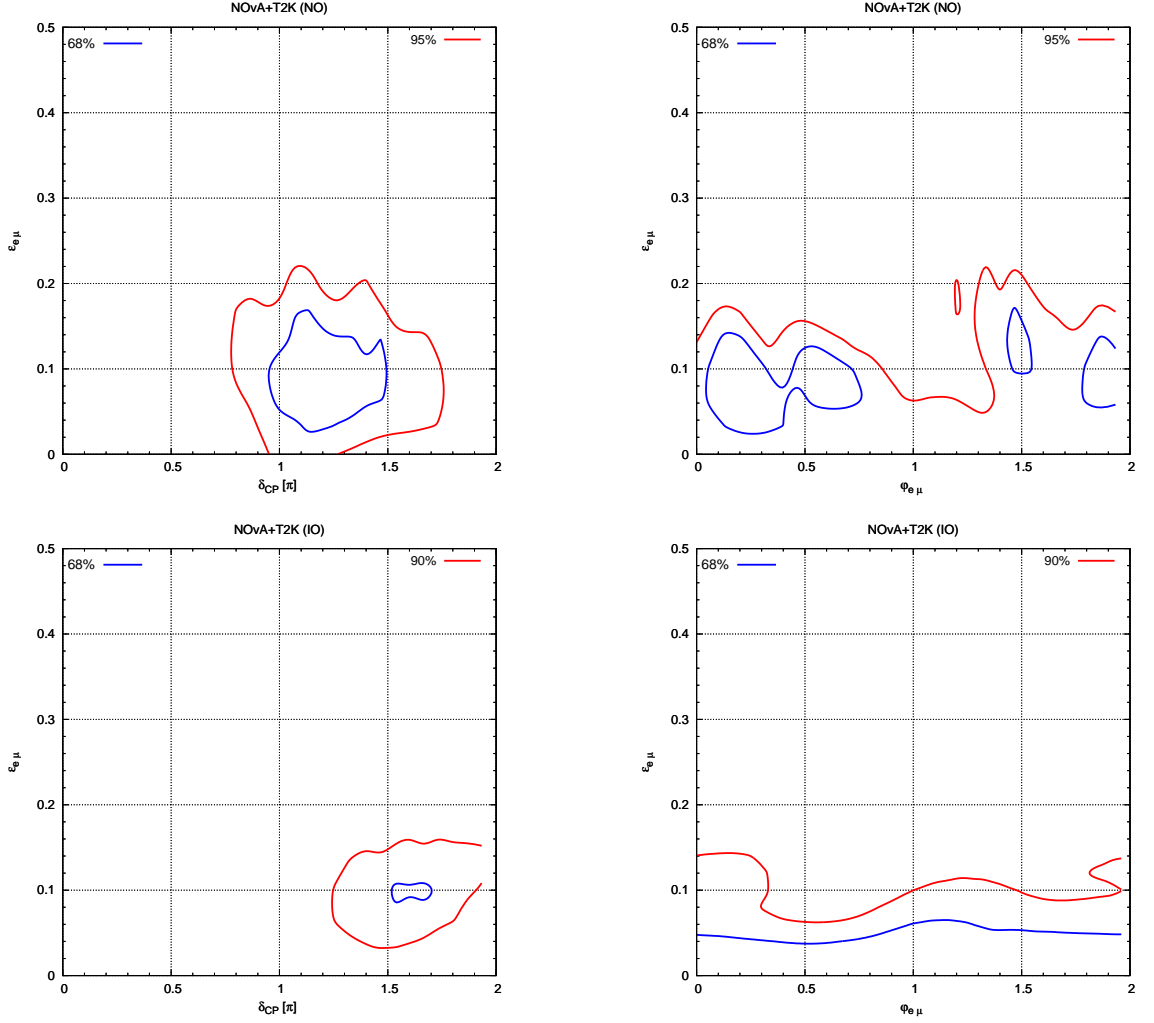


Figure 6.1: Allowed regions for  $\epsilon_{e\mu}$  and the CP phase (left);  $\epsilon_{e\mu}$  and phase  $\phi_{e\mu}$  (right) determined by the combination of T2K and NO $\nu$ A for NO (top panel) and IO (bottom panel). The contours are drawn at the 68% and 90% C.L. for 2 d.o.f.

Table 6.1: From allowed region plots, the best-fit points are listed here. The best-fit points are picked up corresponding to the minimum  $\chi^2$  value. These values are also included in the below table.

| Mass ordering | NSI                | $ \epsilon_{\alpha\beta} $ | $\phi_{\alpha\beta}/\pi$ | $\chi^2$ |
|---------------|--------------------|----------------------------|--------------------------|----------|
| NO            | $\epsilon_{e\mu}$  | 0.1                        | 0.2                      | 0.518    |
|               | $\epsilon_{e\tau}$ | 0.1                        | 1.47                     | 0.385    |
| IO            | $\epsilon_{e\mu}$  | 0.01                       | 1.67                     | 0.533    |
|               | $\epsilon_{e\tau}$ | 0.13                       | 0.8                      | 1.668    |

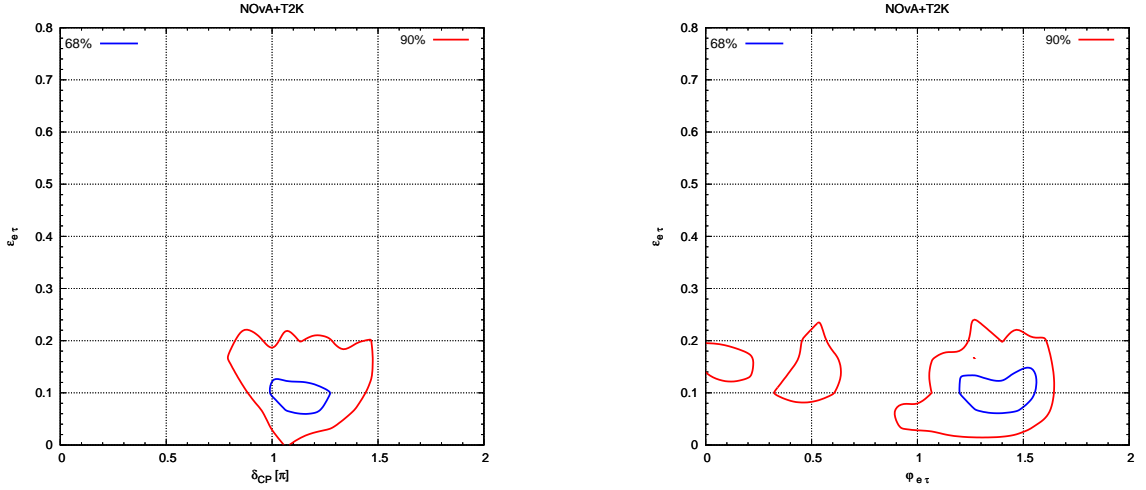


Figure 6.2: Allowed regions for coupling  $\epsilon_{e\tau}$  and CP phase (left);  $\epsilon_{e\tau}$  and phase  $\phi_{e\tau}$  (right) determined by the combination of T2K and NO $\nu$ A for NO. The contours are drawn at the 68% and 90% C.L. for 2 d.o.f.

## DUNE

After obtaining the constraint on the non-standard interaction parameters, we will study their influence on the standard oscillation parameters by plotting the allowed region plots for the standard CP-phase  $\delta_{CP}$  and the atmospheric mixing angle  $\theta_{23}$ . In Fig. 6.3 (top panel), we display the allowed regions in the plane spanned by the standard CP-phase  $\delta_{CP}$  and the atmospheric mixing angle  $\theta_{23}$  for DUNE in the NO scenario. The left panel refers to the SM case, while the middle and right panels show the SM along with NSI arising from the  $e - \mu$  and  $e - \tau$  sectors, respectively. The mixing angle  $\theta_{13}$  and  $\Delta m_{31}^2$  are marginalized away in the SM case whereas along with  $\theta_{13}$  and  $\Delta m_{31}^2$  relevant NSI coupling magnitude ( $\epsilon_{e\mu}/\epsilon_{e\tau}$ ) and non-standard CP-phase ( $\phi_{e\mu}/\phi_{e\tau}$ ) are marginalized in SM with NSI case. We have taken the NSI parameters with their best-fit values from the combined analysis of NO $\nu$ A and T2K in the middle and right panels. To be more specific,  $|\epsilon_{e\mu}| = 0.1$ ,  $\phi_{e\mu} = 0.2\pi$  (middle panel) and  $|\epsilon_{e\tau}| = 0.1$ ,  $\phi_{e\tau} = 1.47\pi$  (right panel).

## T2HK

Next, we discuss the similar allowed region plots for the standard CP-phase  $\delta_{CP}$  and the atmospheric mixing angle  $\theta_{23}$  but now for another long-baseline experiment, T2HK. In Fig. 6.3 (bottom panel), the allowed regions in the plane spanned by  $\delta_{CP}$  and the  $\theta_{23}$  in the NO scenario are displayed. The left panel refers to the SM case, while the middle and right panels concern the SM along with NSI arising from the  $e - \mu$  and  $e - \tau$  sectors, respectively. Comparing the SM scenario with that of SM with NSI arising from  $e - \mu$  sector, in the case of both DUNE and T2HK, we see a clear, distinct parameter space for  $\theta_{23}$ . When

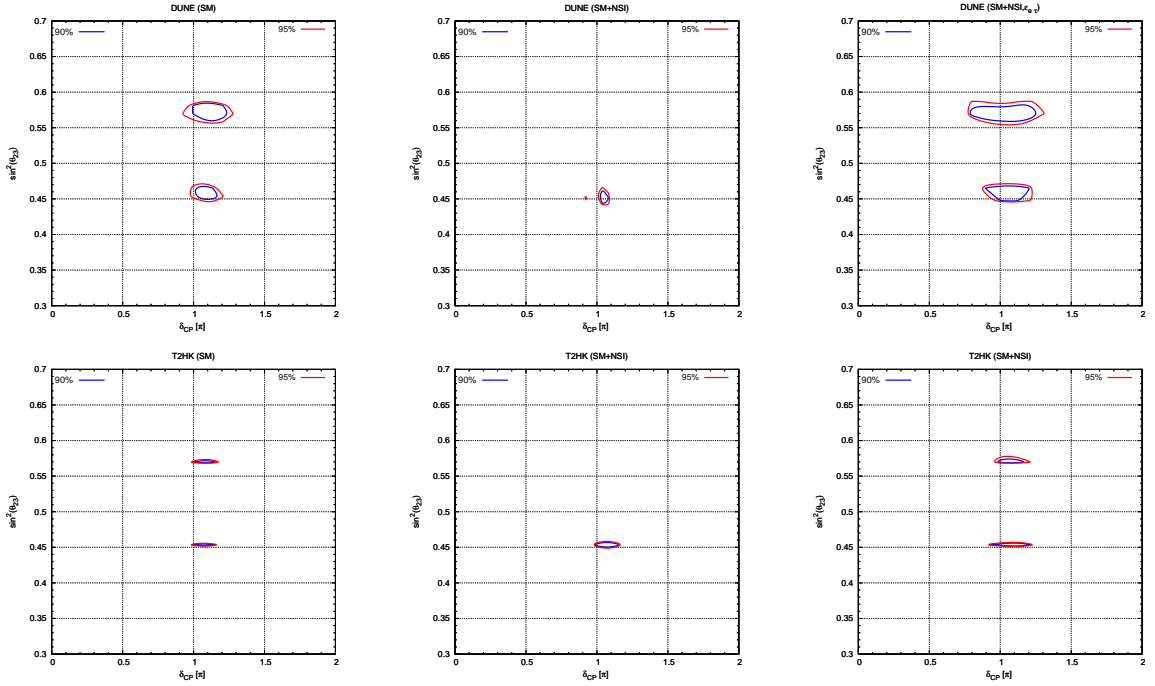


Figure 6.3: Allowed regions determined separately by DUNE and T2HK for NO in the SM case (left panel) and with NSI in the  $e - \mu$  sector (middle panel) and in the  $e - \tau$  sector (right panel). In the middle panel, we have taken the NSI parameters at their best-fit values of  $\text{NO}\nu\text{A}+\text{T2K}$  ( $|\epsilon_{e\mu}| = 0.1$ ,  $|\phi_{e\mu}| = 0.2\pi$ ). Similarly, in the right panel we have taken  $|\epsilon_{e\tau}| = 0.1$ ,  $|\phi_{e\tau}| = 1.47\pi$ . The contours are drawn at the 90% and 95% C.L. for 2 d.o.f.

non-standard interactions are included with SM, the allowed region corresponding to the higher octant disappears, and we are left only with the allowed region from the lower octant. Whereas the situation reverses in the SM along with NSI arising from the  $e - \tau$  sector, as here both lower and the higher octants are allowed for T2HK and DUNE with increased parameter space.

In understanding the preference of the octant for  $\theta_{23}$ , we visualize that in the SM and SM+NSI case arising from  $e - \mu$  sector, there is a clear preference for lower octant in the case of DUNE as well as for T2HK. Corresponding one-dimensional projection plots are given in Figs. 6.4 and 6.5.

## Effect of NSI Parameters on Oscillation Probability

Neutrino propagation through vacuum and matter differ as the neutrinos are subject to interactions with the particles they pass through. Neutrino oscillation in the matter could be affected by the sub-dominant, yet unknown, non-standard interactions. To clearly understand how the non-standard interactions could influence the neutrino oscillations in the long-baseline experiments, like DUNE, and T2HK, we have the corresponding probability

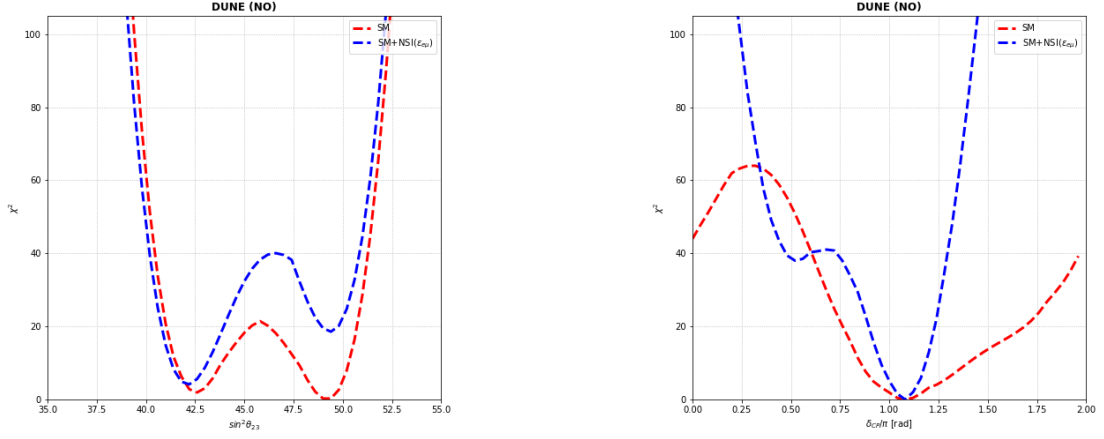


Figure 6.4: One-dimensional projections for the standard parameters  $\theta_{23}$  (left) and  $\delta_{CP}$  (right) for DUNE in the case of NO for SM (red dashed curves) and SM, along with NSI arising from the  $e - \mu$  scenario (blue dashed curves).

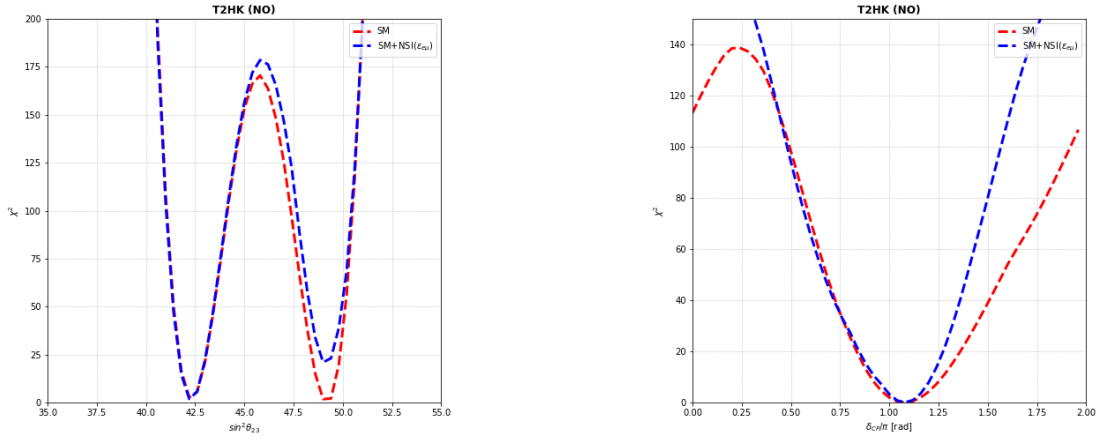


Figure 6.5: One-dimensional projections plots for the standard parameters  $\theta_{23}$  (left) and  $\delta_{CP}$  (right) for T2HK in the case of NO for SM (red dashed curves) and SM, along with NSI arising from the  $e - \mu$  scenario (blue dashed curves).

plots for both neutrino and anti-neutrino modes.

## DUNE

The oscillation probability plots, as given in Fig. 6.6 (top panel), are for DUNE in neutrino mode in the case of SM (left panel), SM along with NSI from the  $e - \mu$  sector (middle panel), and SM along with NSI from the  $e - \tau$  sector (right panel). An appreciable separation between the NO-IO in the SM scenario can be seen for both  $\delta_{CP} = 90^\circ$  and  $\delta_{CP} = -90^\circ$ . In

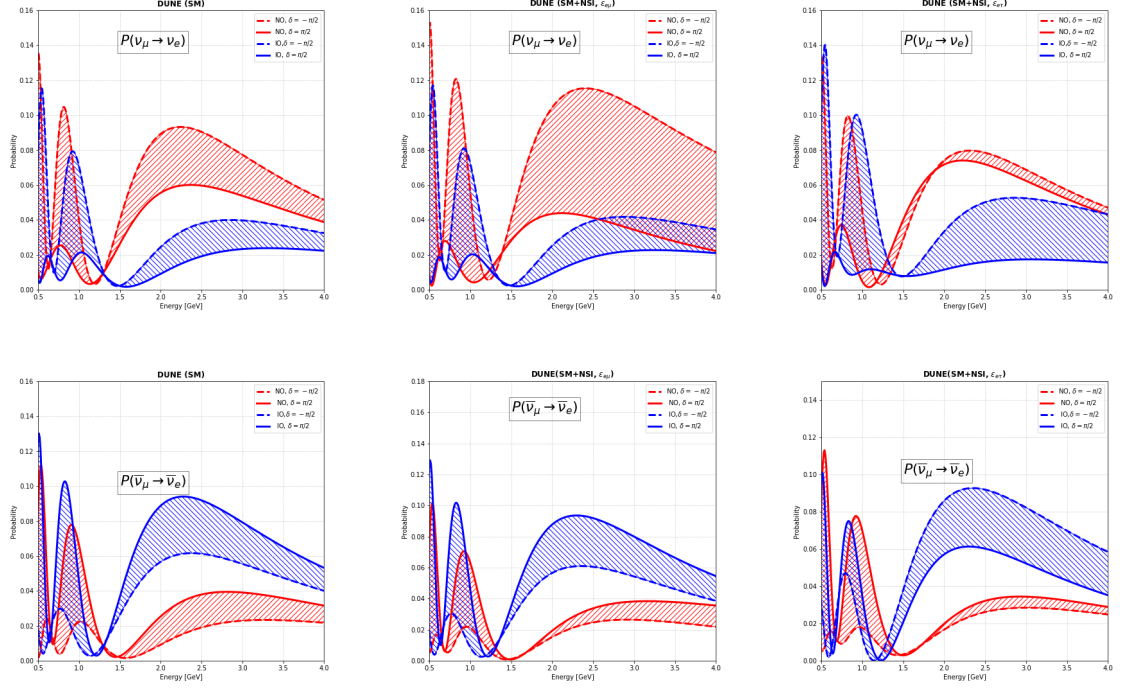


Figure 6.6: Probability Plots for DUNE in SM (left) and SM+NSI scenario with NSI arising from  $e - \mu$  sector (middle) and  $e - \tau$  sector (right) for  $\nu$  (top panel) and  $\bar{\nu}$  (bottom panel) mode

the case of SM, along with the NSI scenario arising from the  $e - \mu$  sector, we still visualize some separation between NO-IO for  $\delta_{CP} = 90^\circ$  in the mid-energy region. Then, around the energy of 4 GeV, they gradually merge. Whereas  $\delta_{CP} = -90^\circ$  has good NO-IO separation. For the SM, in addition to the NSI scenario from the  $e - \tau$  sector, we see a reasonable separation between NO-IO for  $\delta_{CP} = 90^\circ$ . In the case of  $\delta_{CP} = -90^\circ$ , there is some NO-IO separation in the mid-energy region, but the separation gradually decreases as energy increases.

## T2HK

In the case of the T2HK experiment, the oscillation probability plots in neutrino mode for the SM (left panel), SM along with NSI arising from the  $e - \mu$  sector (middle panel), and SM in addition to NSI arising from the  $e - \tau$  sector (right panel) are shown in Fig. 6.7. We see a perceptible separation between NO-IO for both  $\delta_{CP} = 90^\circ$  and  $\delta_{CP} = -90^\circ$  until 1 GeV energy in the SM scenario. We see a better separation between NO-IO for the SM+NSI case from  $e - \mu$  sector for  $\delta_{CP} = -90^\circ$ . The NO-IO separation continuously decreases for  $\delta_{CP} = 90^\circ$  crossing each other around 0.7 GeV. For the SM+NSI case, from  $e - \tau$  sector, we see a separation between NO-IO for  $\delta_{CP} = 90^\circ$  until 1.5 GeV, whereas there is no NO-IO

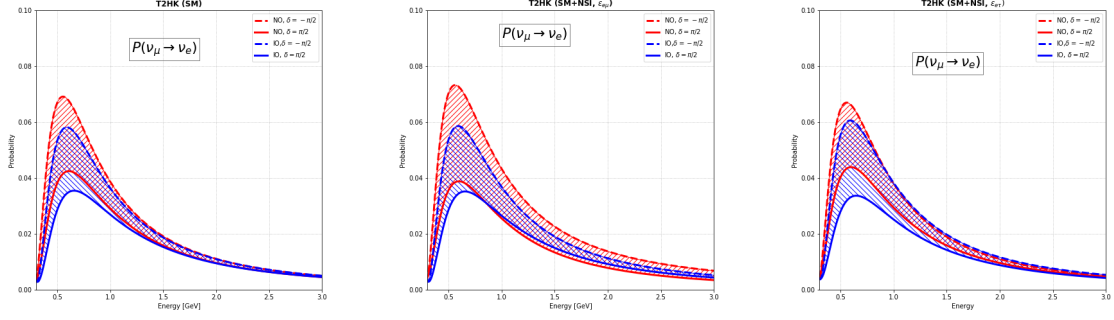


Figure 6.7: Probability Plots for T2HK in SM (left) and SM+NSI scenario with NSI arising from  $e - \mu$  sector (middle) and  $e - \tau$  sector (right).

separation for  $\delta_{CP} = -90^\circ$  after 0.7 GeV energy.

## CP Violation Sensitivity

CP violation in the quark sector has been observed, but it cannot explain the observed baryon asymmetry of the Universe (BAU). Therefore, looking for additional sources of CP violation, including in the lepton sector, is imperative. The lepton mixing matrix contains several CP-violating phases that may impact the standard neutrino oscillations. The parameter that explains CP violation in neutrino oscillations is the angle  $\delta_{CP}$ . One of the most important objectives of the current and upcoming long-baseline neutrino experiments is to determine the CP phase  $\delta_{CP}$  as precisely as possible. Here, we discuss the CP violation in the standard framework of three neutrino oscillations. The signal indicating CP violation in the lepton sector will be seen if the true values of  $\delta_{CP}$  differ from the CP conserving values by a considerable amount [119, 120, 121, 122, 123].

$$\Delta\chi_{CPV}^2 = \text{Min}[\Delta\chi_{CP}^2(\delta_{CP}^{test} = 0), \Delta\chi_{CP}^2(\delta_{CP}^{test} = \pi)]$$

In Fig 6.8, we see that for both DUNE and T2HK, there is an appreciable difference in the sensitivities for the standard model as well as the standard model with the inclusion of non-standard interactions coming from  $e - \mu$  sector. It's worth noting that due to the various baselines and energy of DUNE and T2HK, they are responsible for differences in terms of their sensitivity to non-standard interactions.

### 6.1.5 CP Asymmetry and Mass Hierarchy

As discussed in the above section, CP symmetry violation has already been observed in the quark sector and has been incorporated into the theory of quark mixing. During the Big Bang, without the presence of CP asymmetry, an equal amount of matter and antimatter

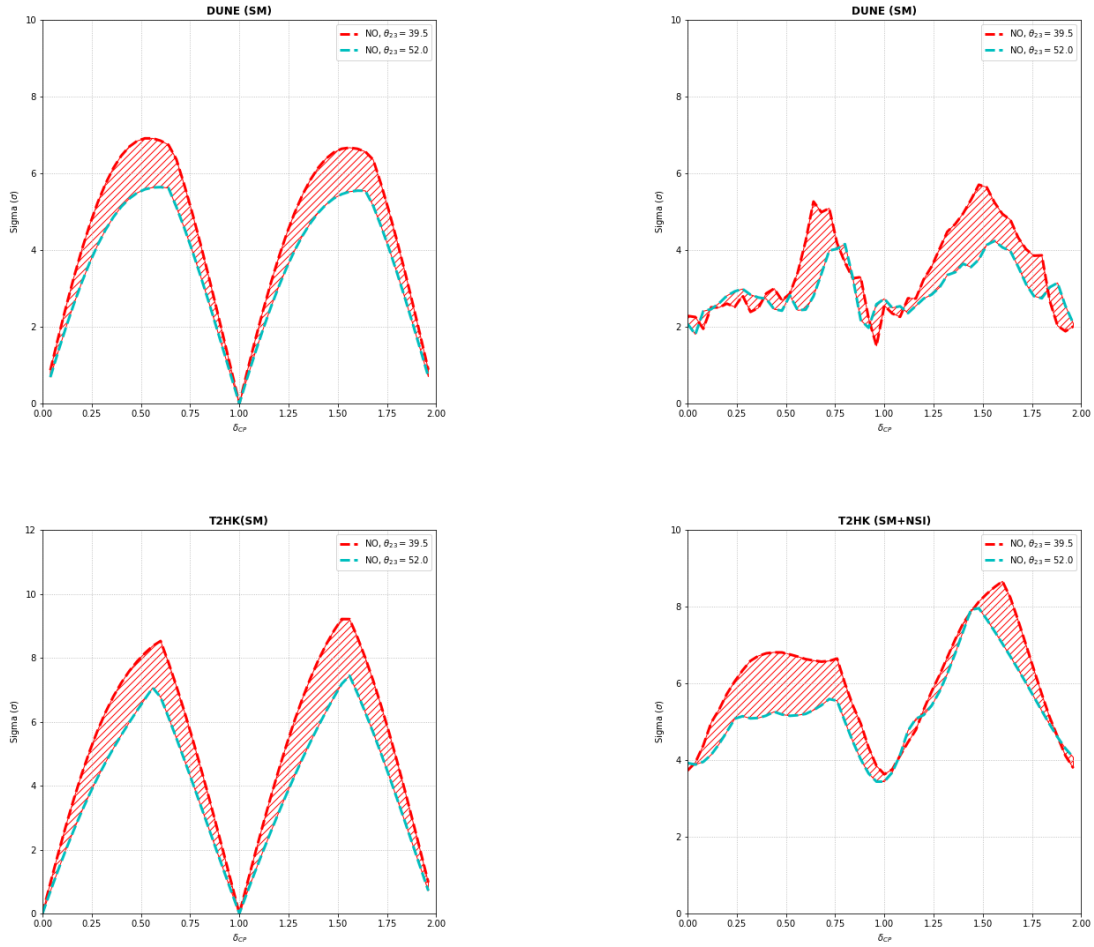


Figure 6.8: CP discovery potential for DUNE (top panel) and T2HK (bottom panel) as a function of the true value of the leptonic CP phase for NO in SM scenario(left panel) and SM+NSI scenario (right panel). The bands represent the range in sensitivity obtained under the two different assumptions of  $\theta_{23}$  value.

would have been created, which would then have annihilated, leaving behind a Universe filled with radiation. In this section, we will investigate the CP violation and understand their possible implications on the neutrino mass ordering. The determination of Neutrino's mass hierarchy is quite challenging. Here, we study the CP asymmetries to decipher the puzzle related to neutrino mass ordering and understand any plausible new physics effect. The CP asymmetry observable can be used to assess CP violation since it measures the change in oscillation probabilities when the sign of the CP phase changes. CP-asymmetry is defined as:

$$A_{CP} \equiv \frac{P(\nu_\alpha \rightarrow \nu_\beta) - P(\bar{\nu}_\alpha \rightarrow \bar{\nu}_\beta)}{P(\nu_\alpha \rightarrow \nu_\beta) + P(\bar{\nu}_\alpha \rightarrow \bar{\nu}_\beta)},$$

CP asymmetry versus energy is shown in Fig 6.9; the top panel is plotted in the presence of NSI arising from the  $\epsilon_{e\mu}$  sector for the DUNE (left) and T2HK (right) experimental setup. An energy band ranging from 2.4 GeV to 2.8 GeV is considered, spanning the DUNE flux peak, i.e., 2.6 GeV. Similarly, for T2HK, the energy band ranges from 0.4 GeV to 0.8 GeV, which is around the T2HK flux peak: 0.6 GeV. The main motivation behind restricting ourselves to the energy range around the peak neutrino beam is for the sake of illustration. Henceforth, the  $A_{CP}$  parameter value obtained is around the peak neutrino energy of their respective experiments.

In the case of DUNE, we observe that the inverted mass ordering (IO) scenario prefers a negative  $A_{CP}$  value of 21%, and the normal mass ordering (NO) shows a positive  $A_{CP}$  value of 76%. We consider here  $\delta_{CP} = 276^\circ$  for the IO scenario and  $\delta_{CP} = 232^\circ$  for the NO case [taken from nuFIT v5.2]. In contrast, in the T2HK energy window, both normal mass ordering and inverted mass ordering show positive  $A_{CP}$  values of 36% and 16%, respectively. Now, we change the NSI effect, and in the bottom panel, we show similar CP asymmetry values, but now with the inclusion of NSI arising from  $\epsilon_{e\tau}$  sector. Here in the DUNE energy window, the NO prefers a positive  $A_{CP}$  value of 58%, whereas IO prefers a negative  $A_{CP}$  value of 18%. Similar to the  $\epsilon_{e\mu}$  case, T2HK in  $\epsilon_{e\tau}$  scenario also prefers a positive  $A_{CP}$  values of 32% and 16% for NO and IO, respectively. Regardless of the NSI sector we consider, NO and IO always prefer the opposite  $A_{CP}$  sign in the DUNE energy window and the same  $A_{CP}$  sign in the T2HK energy window. Thus, in the presence of NSI in DUNE's experimental setup, we can clearly differentiate between the mass hierarchies if we measure the  $A_{CP}$ , which is not observed in the T2HK case.

The measurements related to CP violation asymmetries may help us understand the question of neutrino mass ordering in the neutrino sector. The upcoming LBL experiments will aid in resolving the question of mass ordering along with the discovery of CP violation.

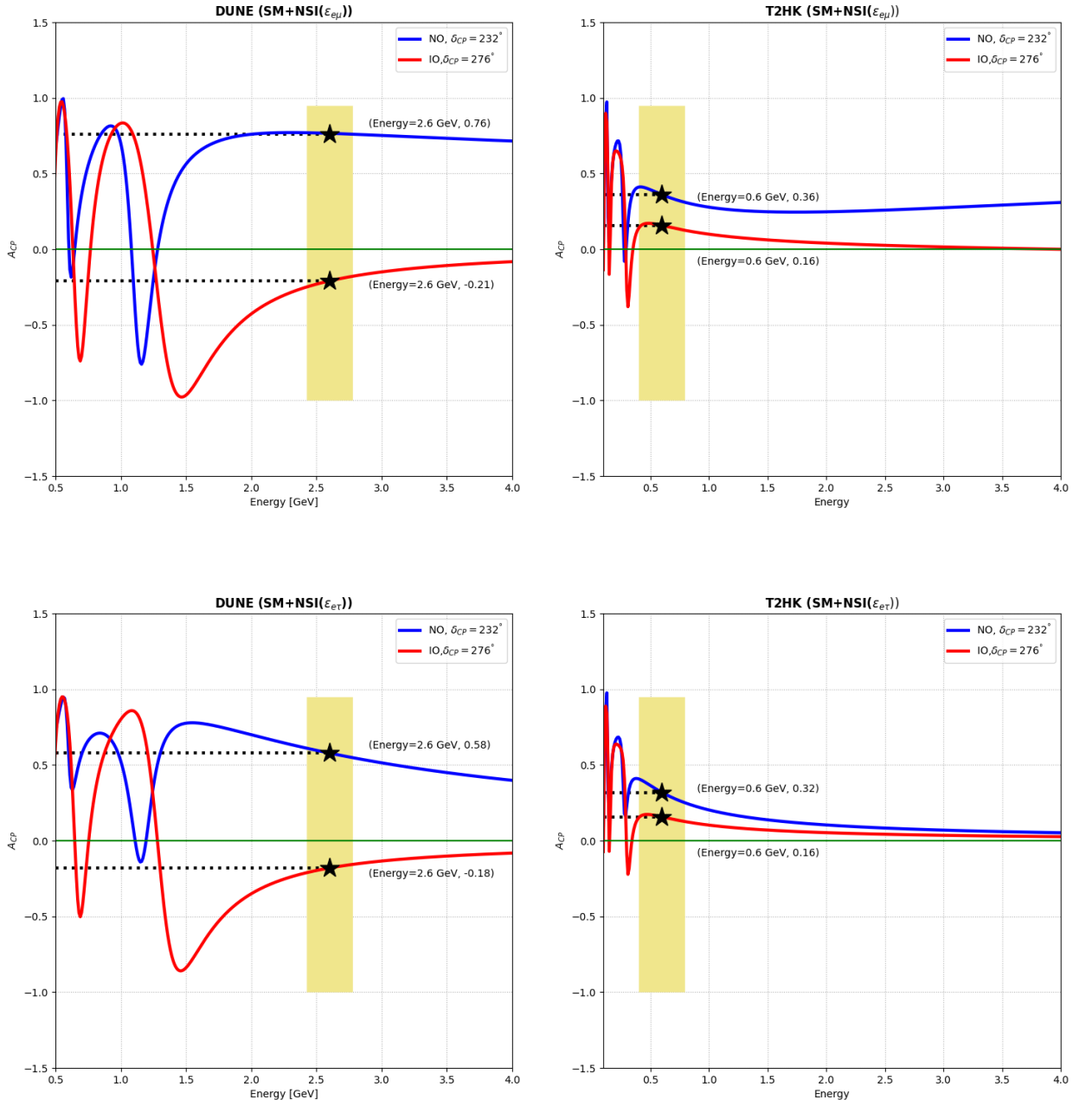


Figure 6.9: CP asymmetry  $A_{CP}$  versus energy [in GeV] in the presence of NSI arising from the  $\epsilon_{e\mu}$  (top) and  $\epsilon_{e\tau}$  (bottom) sector in case of DUNE (left) and T2HK (right) experimental setup. The colored yellow band indicates an energy band around 2.6 GeV for DUNE and 0.6 GeV for T2HK, which we use for illustration in this work. The star points at the obtained  $A_{CP}$  value for the corresponding energy and is also mentioned within the brackets.

# Chapter 7

## Dual Non-Standard Interactions Effects in Long-baseline Neutrino Experiments

As discussed in the previous chapters, the sub-dominant non-standard interactions can affect the neutrino oscillations in the matter. Future long baseline (LBL) neutrino experiments are sensitive to these effects and may provide information on unknown values of oscillation parameters. In this chapter, we investigate the parameter degeneracies that can occur in DUNE and T2HK experiments when non-standard interactions (NSIs) arise simultaneously from two different diagonal sectors, i.e.,  $e - \mu$  and  $e - \tau$ . We derive limits for both NSI sectors using the combined NOvA and T2K data. In the previous chapter, we explored the degeneracy issue for the standard model parameter  $\theta_{23}$  in the presence of NSI arising individually from both  $e - \mu$  and  $e - \tau$  sectors for DUNE and T2HK. In this chapter, our analysis shows the predominant effect that the two NSIs simultaneously can have on the  $\theta_{23}$  sensitivity, which is the atmospheric mixing angle at normal mass ordering. Furthermore, when the interaction of the  $e - \mu$  and  $e - \tau$  sectors is included, we see significant changes in the DUNE and T2HK probabilities. Also, the presence of two NSIs affects the CP sensitivity as well as the CP asymmetry.

### 7.1 Analysis Overview

#### 7.1.1 Formalism

Here, we focus on the dual NSI parameter  $\epsilon_{e\mu}$  and  $\epsilon_{e\tau}$  (simultaneously) to examine the conversion probability of  $\nu_\mu \rightarrow \nu_e$  for the LBL studies. As in Chapter 6 Section 6.1.2, we have set the basis for NSI formalism. Here, with NSI arising from  $e - \mu$  and  $e - \tau$  sector

simultaneously, the probability can be stated as the sum of four (plus higher order, cubic and beyond) terms:

$$P_{\mu e} = P_{SM} + P_{\epsilon_{e\mu}} + P_{\epsilon_{e\tau}} + P_{Int} + h.o. \quad (7.1)$$

the above Eq.(2), similar to [114, 124, 125, 123] takes the following form:

$$P_{SM} = 4s_{13}^2 s_{23}^2 f^2 + 8s_{13} s_{23} s_{12} c_{12} c_{23} r f g \cos(\Delta + \delta_{CP}) + 4r^2 s_{12}^2 c_{12}^2 c_{23}^2 g^2$$

$$\begin{aligned} P_{\epsilon_{e\mu}} &= 4\hat{A}\epsilon_{e\mu}[x f^2 s_{23}^2 \cos(\Psi_{e\mu}) + x f g c_{23}^2 \cos(\Delta + \Psi_{e\mu}) + y g^2 c_{23}^2 \cos \phi_{e\mu} \\ &+ y g f s_{23}^2 \cos(\Delta - \phi_{e\mu})] + 4\hat{A}^2 \epsilon_{e\mu}^2 [f^2 s_{23}^4 + g^2 c_{23}^4 + 2f g s_{23}^2 c_{23}^2 \cos \Delta] \end{aligned}$$

$$\begin{aligned} P_{\epsilon_{e\tau}} &= 4\hat{A}\epsilon_{e\tau}[x f^2 s_{23} c_{23} \cos(\Psi_{e\tau}) - x f g s_{23} c_{23} \cos(\Delta + \Psi_{e\tau}) - y g^2 s_{23} c_{23} \cos \phi_{e\tau} \\ &+ y g f s_{23} c_{23} f \cos(\Delta - \phi_{e\tau})] + 4\hat{A}^2 \epsilon_{e\tau}^2 s_{23}^2 c_{23}^2 [g^2 + f^2 - 2f g \cos \Delta] \end{aligned}$$

$$P_{Int} = 8\hat{A}^2 c_{23} s_{23} \epsilon_{e\mu} \epsilon_{e\tau} [g^2 c_{23}^2 + f^2 s_{23}^2 + 2f g c_{23}^2 \cos(\phi_{e\mu} - \phi_{e\tau}) \cos \Delta - f g \cos(\Delta - \phi_{e\mu} + \phi_{e\tau})]$$

where,  $\Delta = \frac{\Delta m_{31}^2 L}{4E}$ ;  $r = \frac{\Delta m_{21}^2}{\Delta m_{31}^2}$ ;  $\hat{A} = \frac{2\sqrt{2}G_F N_e E}{\Delta m_{31}^2}$ ;  $g \equiv \frac{\sin \hat{A} \Delta}{\hat{A}}$ ;  $f \equiv \frac{\sin[(1-\hat{A})\Delta]}{1-\hat{A}}$ ;  $x \equiv 2s_{13}s_{23}$  and  $y \equiv 2rs_{12}c_{12}c_{23}$ . Furthermore, here we used:  $\Psi_{e\mu} = \phi_{e\mu} + \delta_{CP}$ ;  $\Psi_{e\tau} = \phi_{e\tau} + \delta_{CP}$ , where  $\phi_{e\mu}$  and  $\phi_{e\tau}$  are the non-standard CP-phases corresponding to the relevant NSI coupling  $\epsilon_{e\mu}$  and  $\epsilon_{e\tau}$  respectively.

For anti-neutrino probability,  $P \equiv P(\bar{\nu}_e \rightarrow \bar{\nu}_\mu)$ , is given by changing the above expression for  $P_{SM}$ ,  $P_{\epsilon_{e\mu}}$ ,  $P_{\epsilon_{e\tau}}$ ,  $P_{Int}$  with  $\hat{A} \rightarrow -\hat{A}$  (and hence  $f \rightarrow \bar{f}$ ),  $\delta_{CP} \rightarrow -\delta_{CP}$ , and  $\phi_{\alpha\beta} \rightarrow -\phi_{\alpha\beta}$ . For the inverted hierarchy (IH),  $\delta_{CP} \rightarrow -\delta_{CP}$ ,  $y \rightarrow -y$ ,  $\hat{A} \rightarrow -\hat{A}$  (i.e.,  $f \leftrightarrow -\bar{f}$ , and  $g \leftrightarrow -g$ ).

## 7.2 Analysis details and results:

For the analysis [126, 127], we need to simulate the experiment specifications in GLOBES, which remain similar to the ones discussed in the last chapter. Here, also for DUNE and T2HK, we consider that they are running for 3.5 years and 3 years in  $\nu$  mode and 3.5 years and 4 years in  $\bar{\nu}$  mode, respectively. DUNE [?] will have a 40-kiloton liquid argon detector, which will use a 1.2 MW proton beam to generate neutrino and antineutrino beams from in-flight pion decays. The proton beam will originate 1300 kilometers upstream at Fermilab. The energy ranges for neutrinos will be between 0.5 and 20 GeV, with a flux peak of around 3.0 GeV. The T2HK experiment, on the other hand, will use a 225 kt water Cherenkov detector. It will employ an enhanced 30 GeV J-PARC beam with a power of

1.3 MW, with its detector located 295 kilometers from the source. We use the software GLoBES and its supplementary public tool, which considers the non-standard interactions for the analysis. The extension enables non-standard neutrino interactions and sterile neutrinos in GLoBES simulation. The best-fit values of the standard model parameters, as well as their associated uncertainties, are obtained from nuFIT v5.1 [116] and PDG [?] similar to the ones used in the previous chapter. We use GLoBES to combine the extracted datasets of T2K and NO $\nu$ A. The sensitivity and the oscillation probabilities for the two next-generation upcoming long-baseline experiments, DUNE, T2HK, and a combination of both of these experiments, are discussed using the NSI coefficients thus acquired. We use pre-defined AEDL (a comprehensive abstract experiment definition language) files to simulate experiments like T2HK and DUNE.

Fig. 7.1 displays the analysis results for the combination of NO $\nu$ A and T2K. The allowed region plots scan the parameter space to find constraints on the non-standard interaction parameters like  $e - \mu$  and  $e - \tau$ . Here, we are scanning both the magnitudes  $e - \mu$  and  $e - \tau$  simultaneously, unlike how it was done in the previous chapter. This implies that both the parameters' influence are considered at a time and can set themselves at the best-fit values. In nature, we can not control or regulate the NSI effects coming from various sectors. Even though the effect that the presence of NSI can have on the standard model parameter is at the sub-dominant level, we can not completely deny the possibility that there can be interference from all the sectors at once. Keeping this in mind, we have considered the two of the most dominant NSI parameters and explored their influence on each other while deriving the constraints. The left panel shows the allowed region in the plane spanned by the NSI parameters  $\epsilon_{e\mu}$  and  $\epsilon_{e\tau}$ . In contrast, the right panel displays the allowed region for NSI phases  $\phi_{e\mu}$  and  $\phi_{e\tau}$  for NO scenario (top panel) and IO scenario (bottom panel). For the left panel plots,  $\theta_{13}$ ,  $\delta_{CP}$  along with the non-standard CP-phases  $\phi_{e\mu}$ , and  $\phi_{e\tau}$ , are marginalized away whereas for the right plots,  $\theta_{23}$ ,  $\theta_{13}$  along with the non-standard magnitudes  $\epsilon_{e\mu}$ , and  $\epsilon_{e\tau}$  are marginalized. All the constraint best-fit values are listed in Table 8.2 along with the corresponding  $\chi^2$  values.

## DUNE

Utilizing the obtained constraint from Table 8.2, we will explore their influence on similar standard oscillation parameters as was done in the previous chapter. The allowed region as spanned by the standard CP-phase  $\delta_{CP}$  and the atmospheric mixing angle  $\theta_{23}$  in the NO case for DUNE is shown in the Fig. 7.2 top panel. The top left panel refers to the SM case, while the right one depicts the SM along with the NSI scenario, arising simultaneously from the  $e - \mu$  and  $e - \tau$  sectors. The mixing angle  $\theta_{13}$  and  $\Delta m_{31}^2$  are marginalized away in the SM case. In contrast, for the SM with dual NSI,  $\theta_{13}$  and  $\Delta m_{31}^2$ , with the relevant NSI

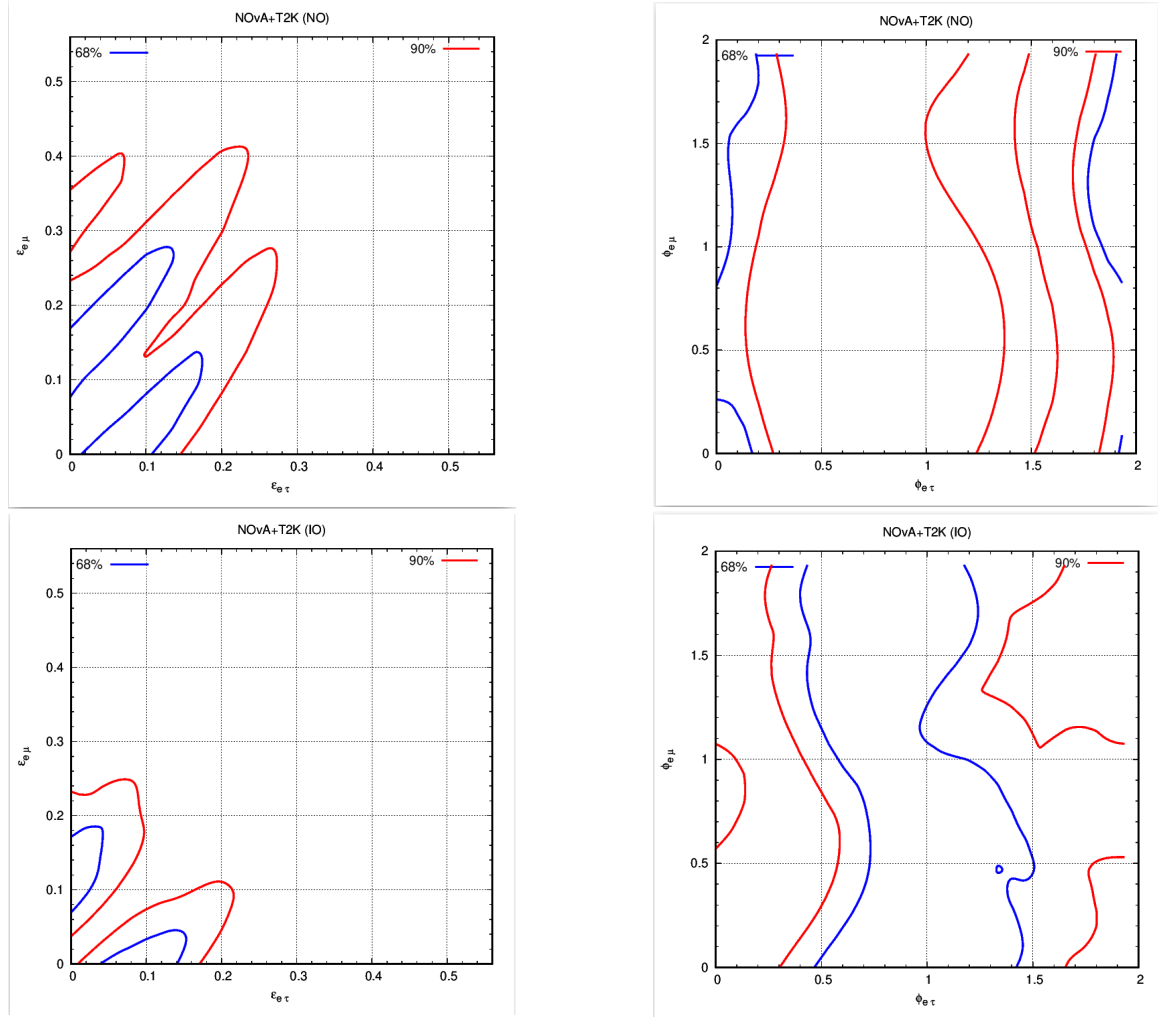


Figure 7.1: Allowed regions in the plane spanned by NSI coupling for  $\epsilon_{e\mu}$  and  $\epsilon_{e\tau}$  (left);  $\phi_{e\mu}$  and phase  $\phi_{e\tau}$  (right) determined by the combination of T2K and NO $\nu$ A for NO (top panel) and IO (bottom panel). The contours are drawn at the 68% and 90% C.L. for 2 d.o.f

couplings ( $\epsilon_{e\mu}$  and  $\epsilon_{e\tau}$ ) and the corresponding non-standard CP-phases: ( $\phi_{e\mu}$  and  $\phi_{e\tau}$ ) are marginalized away. We have taken the NSI parameters with their best-fit values from the combined analysis of NO $\nu$ A and T2K. More specifically,  $|\epsilon_{e\mu}| = 0.1$ ,  $\phi_{e\mu} = 1.06\pi$  and  $|\epsilon_{e\tau}| = 0.033$ ,  $\phi_{e\tau} = 1.87\pi$ . As we include the NSI from the  $e - \mu$  and  $e - \tau$  sectors, the allowed region corresponding to the higher octant disappears, and we are left only with the allowed region from the lower octant.

## T2HK

Similarly, the middle panel of Fig. 7.2 displays the allowed regions in the plane spanned by the standard CP-phase  $\delta_{CP}$  and the atmospheric mixing angle  $\theta_{23}$  in the NO case but now

Table 7.1: From allowed region plots, the best-fit points are listed here. The best-fit points are picked up corresponding to the minimum  $\chi^2$  value. These values are also included in the below table.

| Mass ordering | $ \epsilon_{e\mu} $ | $ \epsilon_{e\tau} $ | $\chi^2$ |
|---------------|---------------------|----------------------|----------|
| NO            | 0.1                 | 0.033                | 0.659    |
| IO            | 0.1                 | 0.02                 | 1.14     |
| Mass ordering | $\phi_{e\mu}/\pi$   | $\phi_{e\tau}/\pi$   | $\chi^2$ |
| NO            | 1.06                | 1.87                 | 0.549    |
| IO            | 1.0                 | 1.73                 | 0.952    |

for another long-baseline experiment T2HK. Comparing the SM scenario (left) with that of SM along with the NSI scenario, arising simultaneously from the  $e - \mu$  and  $e - \tau$  sectors, the allowed region corresponding to the lower octant disappears, and we are left only with the allowed region from the higher octant.

## DUNE+T2HK

The bottom panel of Fig. 7.2 displays the allowed regions in the plane spanned by the standard CP-phase  $\delta_{CP}$  and the atmospheric mixing angle  $\theta_{23}$  in the NO case but for the combination of two long-baseline experiments: DUNE and T2HK. Comparing the SM scenario (left) with that of the SM along with the NSI scenario, arising simultaneously from the  $e - \mu$  and  $e - \tau$  sectors, the allowed region corresponding to the higher octant disappears. We are left only with the allowed region from the lower octant. Comparing all three cases, i.e., DUNE, T2HK, and a combination of DUNE and T2HK, the allowed region corresponding to one of the octants disappears, and we are left only with the allowed region from the other octant.

Concerning the  $\theta_{23}$  octant, we note that in the SM and SM, along with the NSI scenario, arising simultaneously from the  $e - \mu$  and  $e - \tau$  sectors, there is a clear preference for lower octant for DUNE and DUNE+T2HK combination. In contrast, in the case of T2HK, there is a clear preference for a higher octant. Corresponding one-dimensional projection plots for  $\delta_{CP}$  (left) and  $\sin^2 \theta_{23}$  (right) are displayed in Figs. 7.3, 7.4 and 7.5.

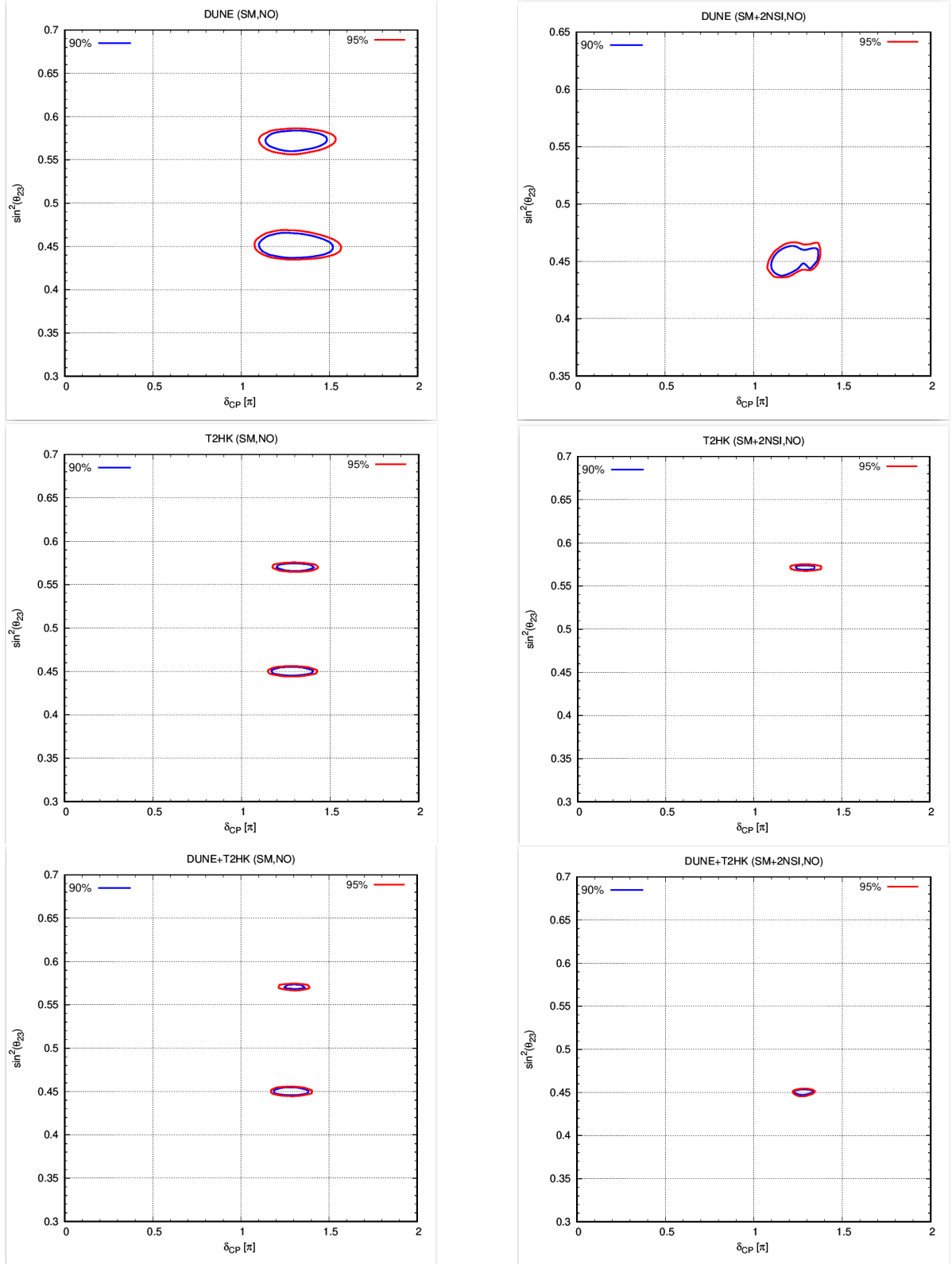


Figure 7.2: Allowed regions determined separately by DUNE (top panel), T2HK (middle panel), and a combination of DUNE and T2HK (bottom panel) for NO in the SM case (left panel) and with dual NSI arising from  $e - \mu$  and  $e - \tau$  sector (right panel). The contours are drawn at the 90% and 95% C.L. for 2 d.o.f.

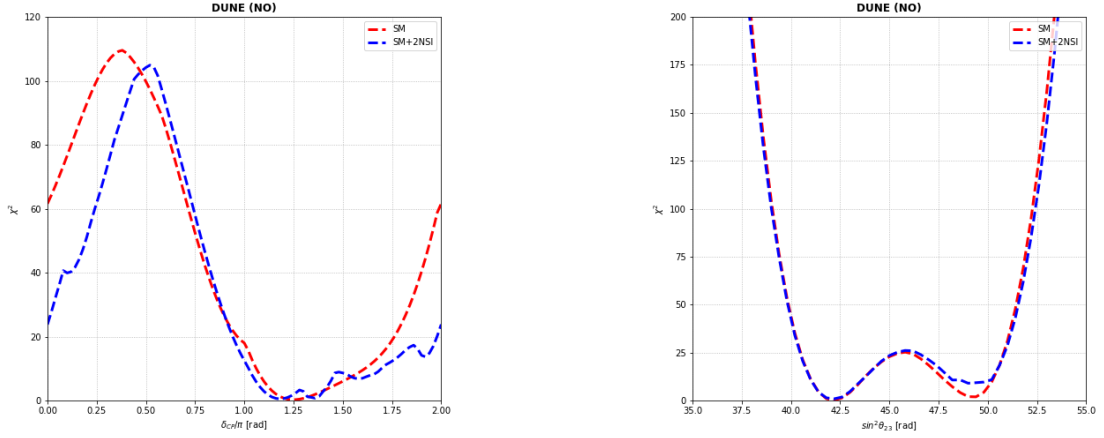


Figure 7.3: One-dimensional projections of the standard parameters  $\theta_{23}$  (left) and  $\delta_{CP}$  (right) determined for DUNE in NO for SM (red dashed curves) and SM, along with the NSI scenario, arising simultaneously from the  $e - \mu$  and  $e - \tau$  sectors. (blue dashed curves).

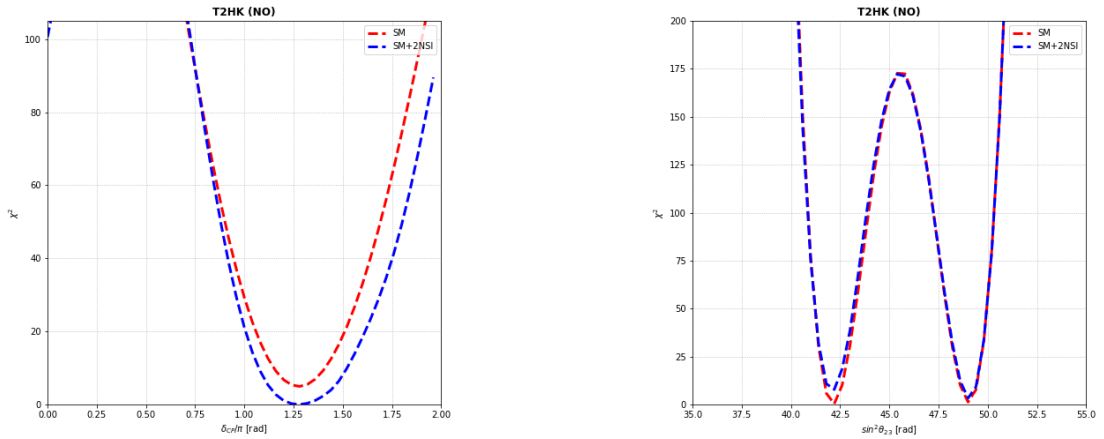


Figure 7.4: One-dimensional projections of the standard parameters  $\delta_{CP}$  determined for T2HK in NO (left) and IO (right) scenario for SM (red dashed curves) and SM, along with the NSI scenario, arising simultaneously from the  $e - \mu$  and  $e - \tau$  sectors. (blue dashed curves).

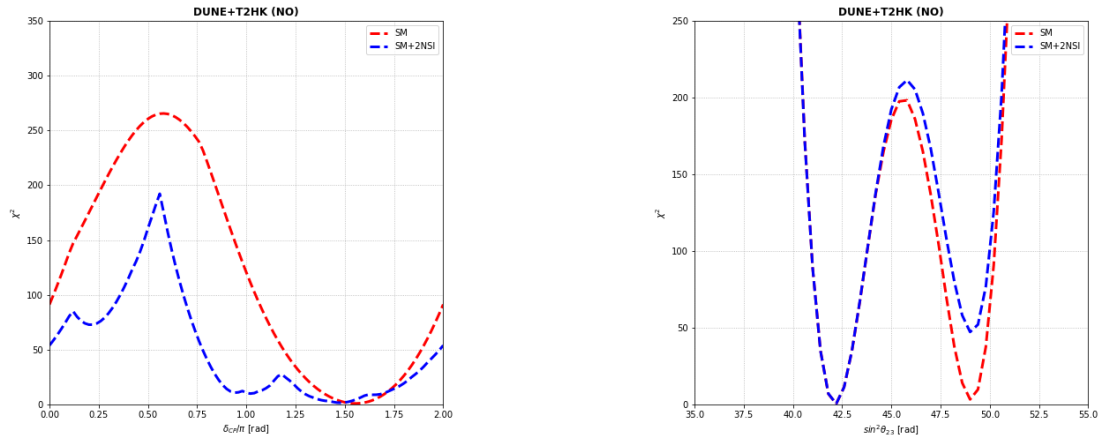


Figure 7.5: One-dimensional projections of the standard parameters  $\theta_{23}$  (left) and  $\delta_{CP}$  (right) determined for DUNE+T2HK in NO for SM (red dashed curves) and SM, along with the NSI scenario, arising simultaneously from the  $e - \mu$  and  $e - \tau$  sectors. (blue dashed curves).

## 7.2.1 Effect of dual NSI Parameters on Oscillation Probability

### DUNE

Similar to the previous chapter, we will study the effect of NSI arising simultaneously from the  $e - \mu$  and  $e - \tau$  sectors on the standard oscillation probabilities. We will discuss the corresponding probability plots for both neutrino and anti-neutrino modes. In Fig. 7.6 (top panel), the oscillation probability plots for DUNE in neutrino mode in the SM (left panel), SM along with the NSI scenario, arising simultaneously from the  $e - \mu$  and  $e - \tau$  sectors (right panel) are shown. In the SM scenario, we see a good separation between NO-IO for both  $\delta_{CP} = 90^\circ$  and  $\delta_{CP} = -90^\circ$ . For the SM along with the NSI scenario, arising simultaneously from the  $e - \mu$  and  $e - \tau$  sectors, we still perceive some separation between NO-IO for  $\delta_{CP} = 90^\circ$  in the mid-energy region. Whereas in the case of  $\delta_{CP} = -90^\circ$ , the NO-IO separation continuously decreases, gradually merging around 4 GeV. For the anti-neutrino scenario, we see a reasonable separation between NO-IO for  $\delta_{CP} = 90^\circ$ , and  $\delta_{CP} = -90^\circ$ , for both SM and SM+2NSI case.

### T2HK

The oscillation probability plots for T2HK are depicted in Fig. 7.7 (top panel) for the neutrino mode in the SM (left panel). The SM, including NSI, arising simultaneously from the  $e - \mu$  and  $e - \tau$  sectors are shown on the right panel. We visualize no separation between NO-IO for  $\delta_{CP} = -90^\circ$  and a feeble separation between NO-IO for  $\delta_{CP} = 90^\circ$  in the SM scenario after 0.6 GeV energy. With the inclusion of dual NSI, we could perceive a feeble separation between NO-IO for  $\delta_{CP} = -90^\circ$  till 0.7 GeV energy and better separation in case of  $\delta_{CP} = 90^\circ$  in the mid-energy region. We have repeated the exercise for the anti-neutrino case in T2HK, which is displayed in Fig. 7.7 (bottom panel).

## 7.3 CP Violation Sensitivity

The important objective of the current and future long-baseline neutrino experiments is to determine the CP phase  $\delta_{CP}$  as precisely as possible. In this context, detecting CP-violation could play an important part in explaining the baryon asymmetry of the universe [?, ?]. The signal indicating CP violation in the lepton sector [?, ?, ?] will be seen if the true values of  $\delta_{CP}$  differ from the CP conserving values by a considerable amount [?].

From the reference Fig.7.8, in the case of DUNE and T2HK, it is clear that there are appreciable differences in the sensitivities for both. The effect on the sensitivity due to the presence of NSI is appreciable in DUNE and DUNE+T2HK combination. In contrast, the

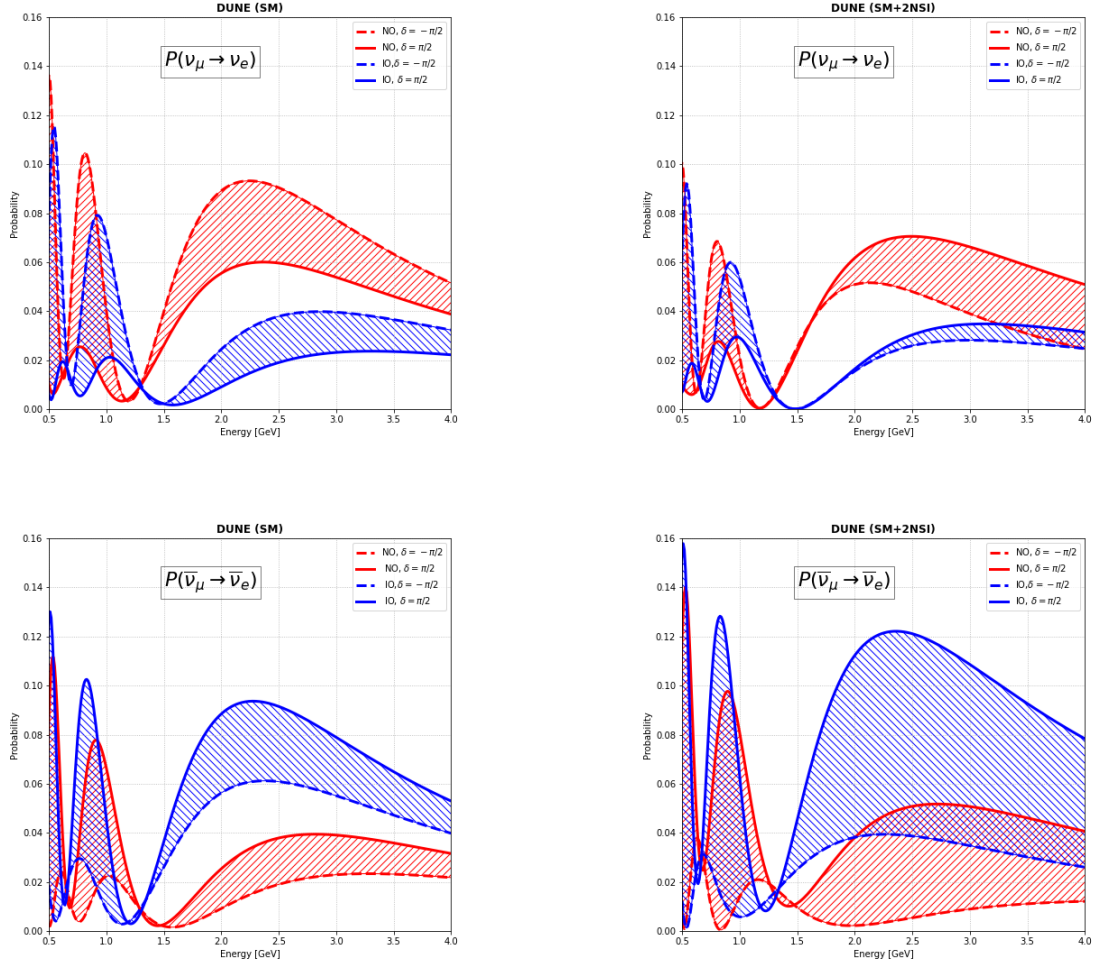


Figure 7.6: Probability Plots for DUNE in SM (left) and SM+2NSI scenario with NSI arising from both  $e - \mu$  sector and  $e - \tau$  sector (right) for  $\nu$  (top panel) and  $\bar{\nu}$  (bottom panel) mode

sensitivity is the least influenced in T2HK due to NSI. In other words, DUNE appears to have better sensitivity to NSI than T2HK.

### 7.3.1 CP Asymmetry

Similarly, in the last section, we investigate the impact that NSI inclusion from  $e - \mu$  and  $e - \tau$  sectors have on the CP measurement potential of two upcoming long-baseline studies, DUNE and T2HK. At the probability level, the CP-asymmetry parameter can be written as follows [?]:

$$A_{CP} = \frac{P(\nu_\mu \rightarrow \nu_e) - P(\bar{\nu}_\mu \rightarrow \bar{\nu}_e)}{P(\nu_\mu \rightarrow \nu_e) + P(\bar{\nu}_\mu \rightarrow \bar{\nu}_e)}$$

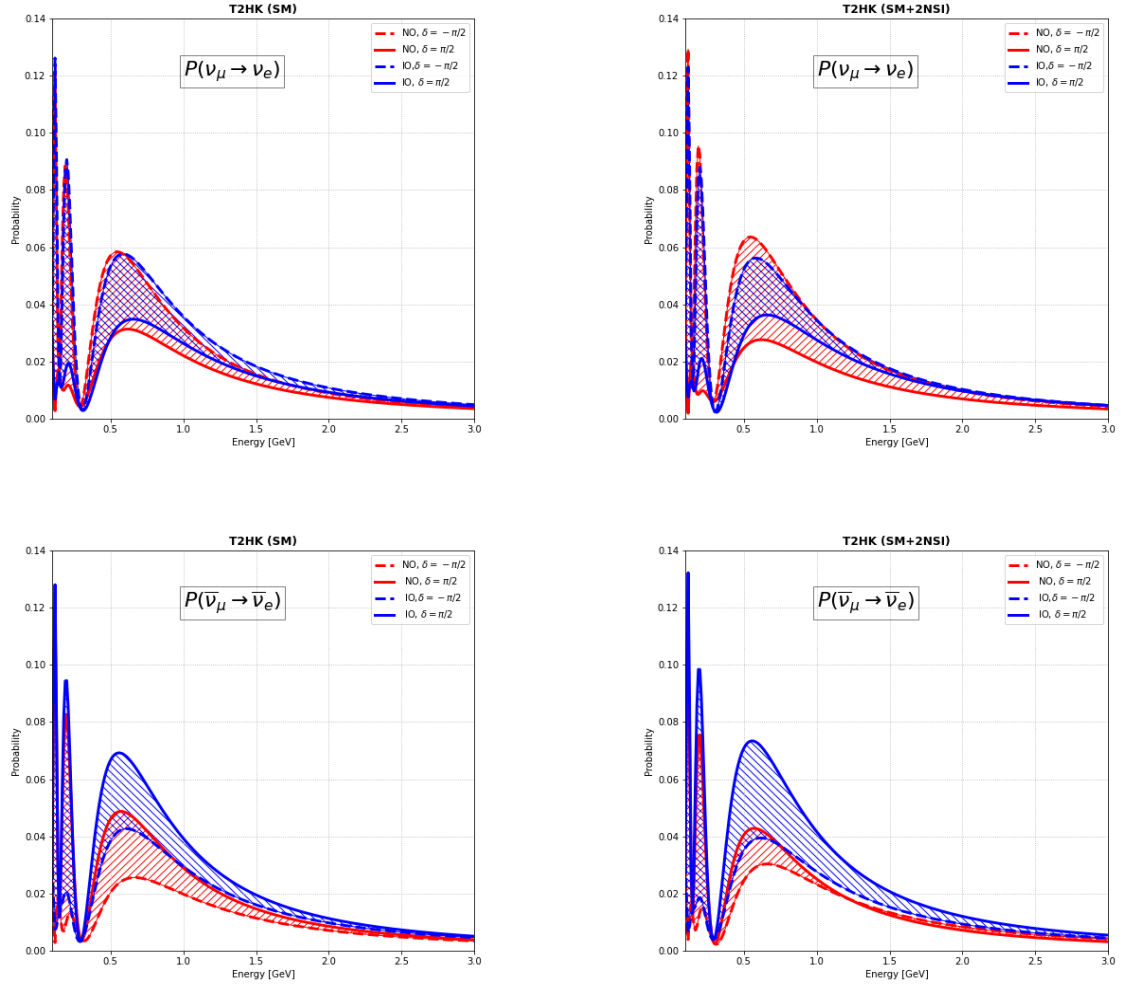


Figure 7.7: Probability Plots for T2HK in SM (left) and SM+2NSI scenario with NSI arising from both  $e - \mu$  sector and  $e - \tau$  sector (right) for  $\nu$  (top panel) and  $\bar{\nu}$  (bottom panel) mode

where,  $P_{\mu e}$  and  $\bar{P}_{\mu e}$  are the appearance probabilities of  $\nu_e$  and  $\bar{\nu}_e$  respectively. The CP asymmetry parameter, ( $A_{CP}$ ), can be used to assess CP violation since it measures the change in oscillation probabilities when the CP phase changes sign. The baseline and energy strongly influence the shape and magnitude of the CP-asymmetry curve. For DUNE and T2HK experiments, the baselines are taken to be 1300km and 295km, respectively, whereas energy is considered to be 2.6 GeV and 0.6 GeV, respectively. In Fig. 7.9, one can visualize the significant separation between the CP asymmetry parameters. This study can help us differentiate between the neutrino mass hierarchies. In Figure 7.9, we have plotted the  $A_{CP}$  parameter for energy varying from 0 to 4 GeV in normal mass and inverted mass hierarchy for the DUNE experiment in the top panel. In these plots, we have plotted CP

asymmetry in the presence of vacuum, matter, and non-standard interaction (NSI) arising from  $\epsilon_{e\mu}$  and  $\epsilon_{e\tau}$  sectors simultaneously. At around DUNE energy, we can see the matter profile and dual NSI scenario probing opposite signs of CP asymmetry for NO and IO cases. Thus, it suggests the possibility of differentiating both mass orderings in the DUNE experimental setup. In the bottom plots, we have the T2HK experimental setup. At around the T2HK's energy window, we can see the matter profile and dual NSI scenario probing more or less similar signs of CP asymmetry for both NO and IO cases. Thus, it is possible that the T2HK experiment might be unable to differentiate between the mass orderings. The average  $A_{CP}$  values for both the mass ordering in the presence of vacuum, matter, and dual NSI are depicted in Table 7.2.

Table 7.2: The average CP asymmetry in the presence of vacuum, matter, and dual NSI scenario for the DUNE energy window (2 GeV - 3 GeV) and T2HK energy window (0.5 GeV - 1 GeV) are included in the table below.

|                      |                  |              |                  |              |
|----------------------|------------------|--------------|------------------|--------------|
|                      | <b>DUNE (NO)</b> | $A_{CP}$ (%) | <b>DUNE (IO)</b> | $A_{CP}$ (%) |
| In<br>Presence<br>of | Vacuum           | 25           | Vacuum           | 26           |
|                      | Matter           | 66           | Matter           | -27          |
|                      | Dual NSI         | 71           | Dual NSI         | -27          |
|                      | <b>T2HK (NO)</b> | $A_{CP}$ (%) | <b>T2HK (IO)</b> | $A_{CP}$ (%) |
| In<br>Presence<br>of | Vacuum           | 21           | Vacuum           | 22           |
|                      | Matter           | 30           | Matter           | 13           |
|                      | Dual NSI         | 2            | Dual NSI         | 14           |

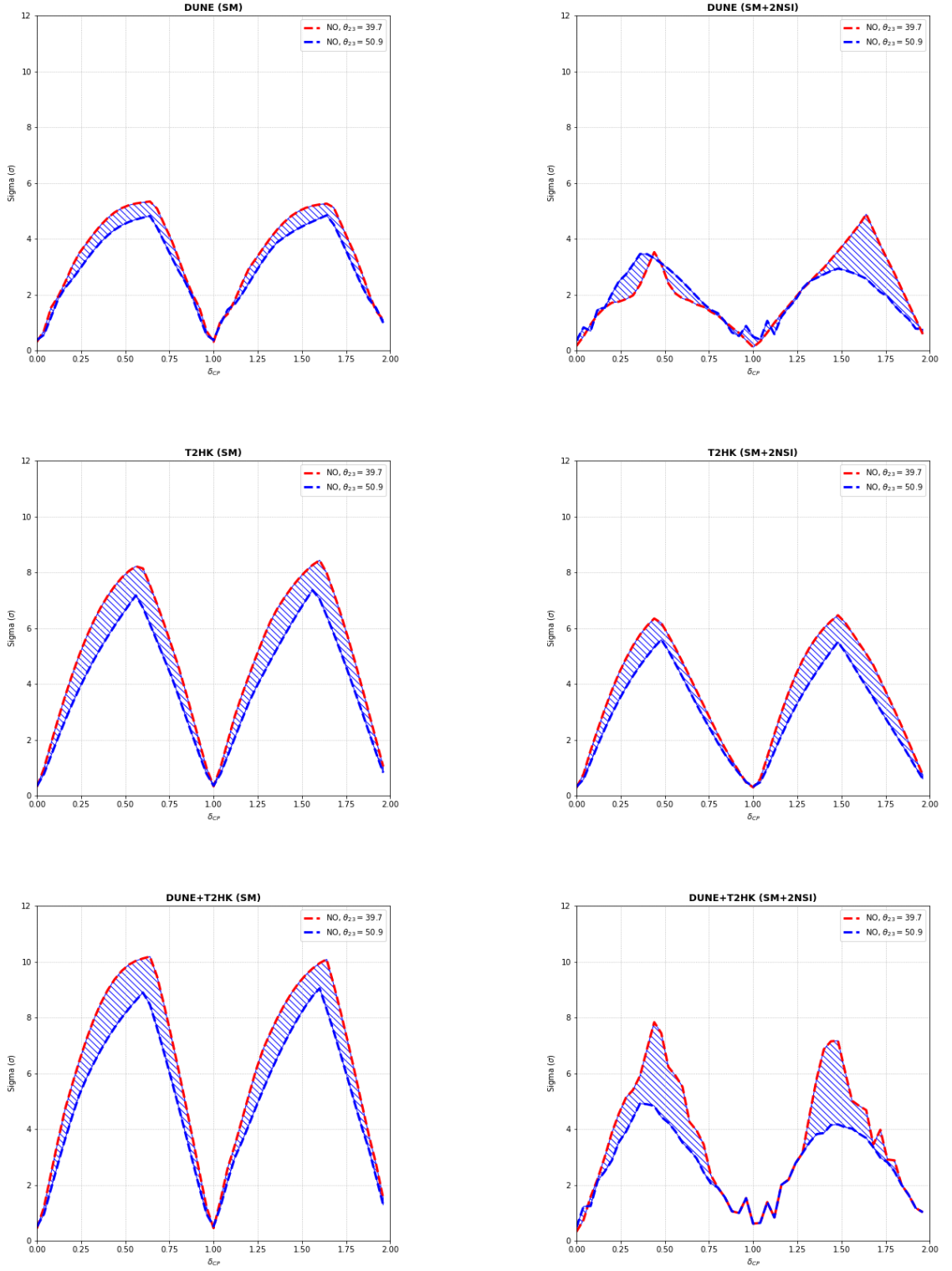


Figure 7.8: CP discovery potential for DUNE (top panel), T2HK (middle panel), and DUNE+T2HK (bottom panel) as a function of the true value of the leptonic CP phase for NO in SM scenario (left panel) and SM+2NSI scenario (right panel). The bands represent the range in sensitivity obtained under the two different assumptions of  $\theta_{23}$  value.

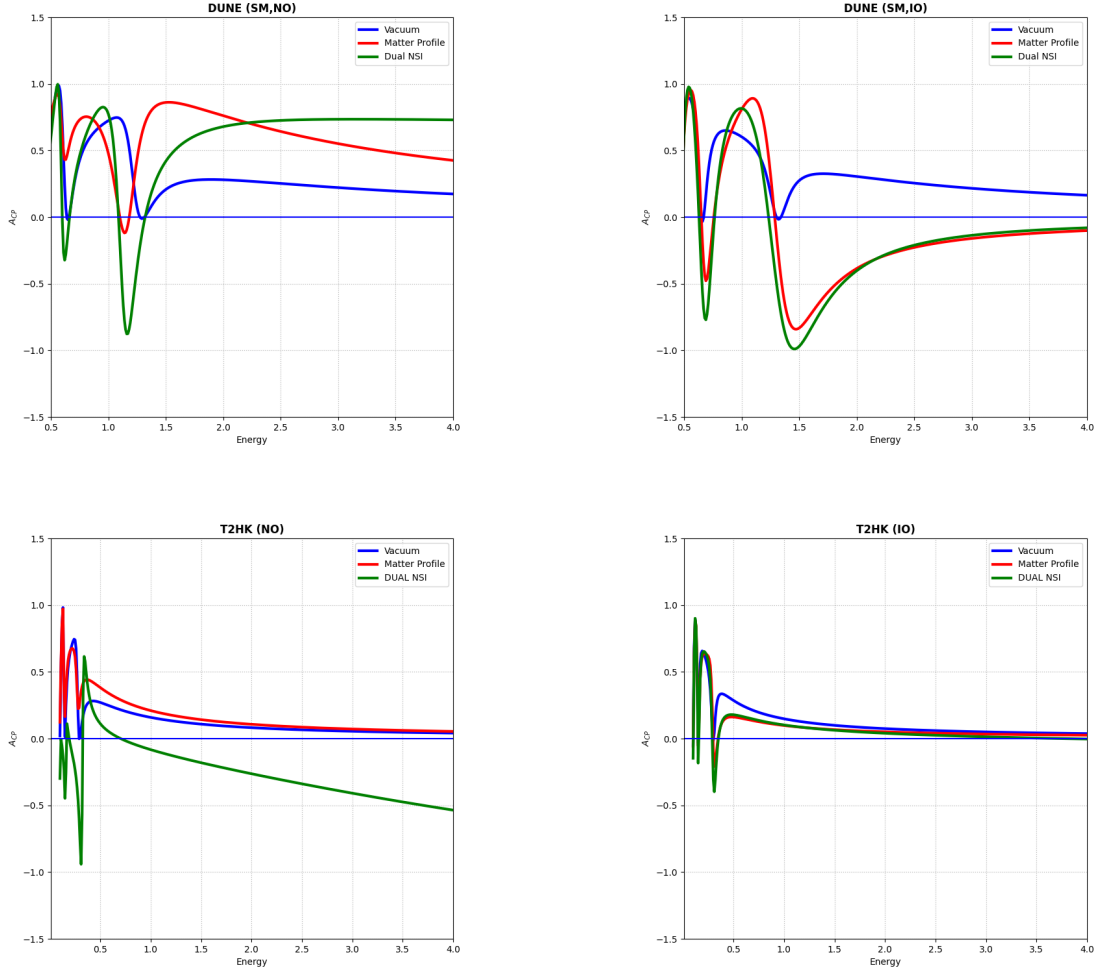


Figure 7.9: CP asymmetry  $A_{CP}$  versus Energy [in GeV] plot for both NO and IO scenarios. In the above plots, we have included vacuum, SM with matter effects, and SM with the inclusion of NSI arising simultaneously from  $\epsilon_{e\mu}$  and  $\epsilon_{e\tau}$  in the T2HK and DUNE experimental setup

# Chapter 8

## Conclusion and Future Directions

This chapter summarizes the results obtained in the light-dark matter analysis using NOvA near detector and the non-standard neutrino interaction study in long-baseline experiments. Both of these studies correspond to beyond standard model physics scenarios.

### 8.1 Light-Dark Matter Analysis

In the dark matter analysis, we preliminary studied DM electron scattering patterns in the NOvA near detector using the simulated MC samples. The leading dark matter candidates in the LDm analysis are the WIMPs (weakly interacting massive particles). We simulate the DM production using the software BdNMC [84]. Specific distribution of recoil energy and scattering angle of single electrons are obtained from the simulation. Normalization of these specific energies provides us with a “generic” energy distribution. The “generic” distributions are provided as input in order to simulate the NOvA detector response to these scattered single electrons using NOvASoft. The generic signal sample can be reweighted to obtain a specific signal pattern for corresponding dark matter masses starting from 5 MeV to 450 MeV.

We perform a raster scan in the concerned parameter space and determine the detector sensitivity utilizing the neutrino background and the systematic uncertainties. Raster scans, in general, can be applied in searches for new particles or new phenomena. In this, we search in the physically interesting region of the parameter space or masses before moving on to the next mass. At each one separately, we try to conclude as to whether we can claim to have a discovery, exclude the existence of the new particle, or be unable to discriminate between them. The signal that we looked for in this analysis is a single EM shower along the beam direction. The most obvious or dominant background we deal with are the  $\nu - e$  elastic scattering and other beam-related interactions in the detector. A preselection is applied to remove the background interactions produced in the detector. The cumulative

efficiency of all the applied selection criteria implies that we have removed the beam-related background appreciably. For the background coming from  $\nu$ - $e$ , the corresponding samples are weighted by `kPPFXFluxCVWgt` and radiative correction `kRadWt`. The beam-related background samples are weighted by `kPPFXFluxCVWgt` and `kXSecCVWgt2020GSFProd51`. Both the components are normalized by POT.

The signal efficiency, the detector simulation, and the POT calculation cause systematic uncertainties in the analysis. Detector systematic uncertainties for the NOvA near detector are calibration, light level, and Cherenkov effects. Beam flux systematic uncertainties on the hadron production. Absolute normalization is a systematic way of addressing the overall normalization while producing signal samples. Cross-section systematic uncertainties to count all the latest NOvA cross-section-related systematic uncertainties. After applying the selection efficiency and the systematic uncertainty study, we scan the DM mass parameter space  $(Y, m_\chi)$  to validate the sensitivity of the NOvA experiment.

Our analysis suggests that in the 5 to 100 MeV DM mass window, NOvA can explore so far unprobed regions of the parameters space  $(Y, m_\chi)$  reaching down to the thermal relic line for the value  $\alpha_D = 1/2$  for a complex scalar DM candidate. This represents a significant improvement over existing experimental measurements, Babar [72], LSND [87, 88], E137 [89], NA64 [90], MiniBooNE [91], and COHERENT [92] as well. We want to apply a similar analysis procedure to check whether we can discover excess single EM showers from the NOvA true dataset. In particular, if a discovery can be made, it would then also be possible to study the properties of this particle.

## 8.2 Non-Standard Neutrino Interactions

To investigate new physics, Neutrino oscillations in matter offer a novel path. One of the main goals of neutrino experiments is to determine the CP phase and the presence of new physics, which can alter the scenario. We assume that the observed difference, if any, in the CP phase is due to the possible non-standard interactions. In our work, we have tried to derive the relevant coupling strengths using the simulated data sets of NOvA and T2K and study their effects in the next-generation long-baseline experiments: T2HK and DUNE. The influence of the presence of NSI on the standard model oscillation parameters is an important study carried out here. Our analysis significantly impacts the sensitivity of atmospheric mixing angle  $\theta_{23}$  in the normal and inverted mass orderings. Also, it exhibits appreciable differences in probabilities for both experiments when non-standard interaction arising from  $e - \mu$  and  $e - \tau$  sectors are included.

When we considered the individual NSI parameters, the constraints we obtained are:

Utilizing the derived constraints, we obtained that with NSI arising from the  $e - \mu$  sector, both DUNE and T2HK prefer the lower octant, whereas the inclusion of NSI arising

Table 8.1: The best-fit points are listed here. The best-fit points are picked up corresponding to the minimum  $\chi^2$  value.

| Mass ordering | NSI                | $ \epsilon_{\alpha\beta} $ | $\phi_{\alpha\beta}/\pi$ | $\chi^2$ |
|---------------|--------------------|----------------------------|--------------------------|----------|
| NO            | $\epsilon_{e\mu}$  | 0.1                        | 0.2                      | 0.518    |
|               | $\epsilon_{e\tau}$ | 0.1                        | 1.47                     | 0.385    |
| IO            | $\epsilon_{e\mu}$  | 0.01                       | 1.67                     | 0.533    |
|               | $\epsilon_{e\tau}$ | 0.13                       | 0.8                      | 1.668    |

from the  $e - \mu$  sector brings back the degeneracy of both the lower and higher octants. We have considered the case for normal ordering here mostly. Moreover, using the same set of constraints, we see striking differences in oscillation probabilities for neutrino channels in DUNE. Future data from NOvA and T2K will decide the existing tension's fate in the  $\delta_{CP}$  parameter and clear the picture.

In chapter 7, NSI arising simultaneously from  $e - \mu$  and  $e - \tau$  sectors are discussed. Here, along with DUNE and T2HK, there is a combination of both experiments, i.e., DUNE+T2HK was studied. The constraints derived are:

Table 8.2: The best-fit points are picked up corresponding to the minimum  $\chi^2$  value for the simultaneous scanning of non-standard parameters:  $\epsilon_{e\mu}$  and  $\epsilon_{e\tau}$

| Mass ordering | $ \epsilon_{e\mu} $ | $ \epsilon_{e\tau} $ | $\chi^2$ |
|---------------|---------------------|----------------------|----------|
| NO            | 0.1                 | 0.033                | 0.659    |
| IO            | 0.1                 | 0.02                 | 1.14     |
| Mass ordering | $\phi_{e\mu}/\pi$   | $\phi_{e\tau}/\pi$   | $\chi^2$ |
| NO            | 1.06                | 1.87                 | 0.549    |
| IO            | 1.0                 | 1.73                 | 0.952    |

When we use NSI arising from both sectors simultaneously, DUNE prefers the lower octant, T2HK prefers the higher octant, and a combination of both DUNE and T2HK prefers the lower octant. One-dimensional projection plots depict the same outcome. Moreover, we observed the striking effects of dual NSI constraints on both neutrino and anti-neutrino channel probabilities in DUNE, T2HK. Here, in our work, the assessment of CP asymmetry reveals that with the inclusion of NSI from  $e - \mu$  and  $e - \tau$  sectors, simultaneously, we visualize a significant separation between SM and SM with the inclusion of NSI from both the sectors in T2HK and than in DUNE. Furthermore, the CP discovery potential showed

that the effect of dual NSI reduces the sensitivity, which is prominent in DUNE compared to T2HK, and a combination of both.

The next era of DUNE and T2HK neutrino experiments will better understand the neutrino sector and help us unravel the CP asymmetry and the long-standing mystery of neutrino mass hierarchies. If the tension persists, as we have shown in this analysis, it could probably signal the existence of new physics. Nonetheless, future studies may enable us to disentangle the NSI effects for cleaner extraction of the neutrino parameters.

# References

- [1] S. Weinberg. A Model of Leptons. *Phys. Rev. Lett.* 19, (1967) 1264–1266. 1
- [2] S. L. Glashow. Partial-symmetries of weak interactions. *Nuclear Physics* 22, (1961) 579–588. 1
- [3] A. Salam. Weak and Electromagnetic Interactions. *Conf. Proc. C* 680519, (1968) 367–377. 1
- [4] G. S. Guralnik, C. R. Hagen, and T. W. B. Kibble. Global Conservation Laws and Massless Particles. *Phys. Rev. Lett.* 13, (1964) 585–587. 1
- [5] Y. Fukuda et al. Evidence for oscillation of atmospheric neutrinos. *Phys. Rev. Lett.* 81, (1998) 1562–1567. 4, 20
- [6] R. N. Mohapatra and P. B. Pal. Massive neutrinos in physics and astrophysics. Second edition, volume 60. 1998. 4
- [7] S. Pakvasa and J. W. F. Valle. Neutrino properties before and after KamLAND. *Proc. Indian Natl. Sci. Acad. A* 70, (2004) 189–222. 4
- [8] J. W. F. Valle. Neutrino masses: evidences and implications. *Journal of Physics: Conference Series* 485, (2014) 012,005. 4
- [9] J. W. F. Valle and J. C. Romao. Neutrinos in high energy and astroparticle physics. Physics textbook. Wiley-VCH, Weinheim, 2015. 4
- [10] S. M. Bilenky. Prehistory of neutrino oscillation. In International Conference on History of the Neutrino: 1930-2018. 2019 . 4
- [11] W. Pauli. Dear radioactive ladies and gentlemen. *Phys. Today* 31N9, (1978) 27. 5
- [12] E. Fermi. An attempt of a theory of beta radiation. 1. *Z. Phys.* 88, (1934) 161–177. 5
- [13] E. Fermi. Trends to a Theory of beta Radiation. (In Italian). *Nuovo Cim.* 11, (1934) 1–19. 5

- [14] J. Chadwick. Possible Existence of a Neutron. *Nature* 129, (1932) 312. 5
- [15] F. Reines and C. L. Cowan. Detection of the free neutrino. *Phys. Rev.* 92, (1953) 830–831. 6
- [16] C. L. Cowan, F. Reines, F. B. Harrison, H. W. Kruse, and A. D. McGuire. Detection of the free neutrino: A Confirmation. *Science* 124, (1956) 103–104. 6
- [17] F. Reines, C. L. Cowan, F. B. Harrison, A. D. McGuire, and H. W. Kruse. Detection of the free anti-neutrino. *Phys. Rev.* 117, (1960) 159–173. 6
- [18] R. E. Carter, F. Reines, J. J. Wagner, and M. E. Wyman. Free anti-neutrino absorption cross-section. 2: Expected cross-section from measurements of fission fragment electron spectrum. *Phys. Rev.* 113, (1959) 280–286. 6
- [19] K. Kodama et al. Observation of tau neutrino interactions. *Phys. Lett. B* 504, (2001) 218–224. 8
- [20] R. Abbasi et al. Observation of Seven Astrophysical Tau Neutrino Candidates with IceCube. *Phys. Rev. Lett.* 132, (2024) 151,001. 8
- [21] P. Lipari. Introduction to neutrino physics. In 1st CERN-CLAF School of High-Energy Physics. 2001 115–199. 9
- [22] R. Davis, Jr., D. S. Harmer, and K. C. Hoffman. Search for neutrinos from the sun. *Phys. Rev. Lett.* 20, (1968) 1205–1209. 10, 20
- [23] B. T. Cleveland, T. Daily, R. Davis, Jr., J. R. Distel, K. Lande, C. K. Lee, P. S. Wildenhain, and J. Ullman. Measurement of the solar electron neutrino flux with the Homestake chlorine detector. *Astrophys. J.* 496, (1998) 505–526. 10
- [24] J. N. Bahcall and M. H. Pinsonneault. Standard solar models, with and without helium diffusion and the solar neutrino problem. *Rev. Mod. Phys.* 64, (1992) 885–926. 10
- [25] R. Davis. A review of the Homestake solar neutrino experiment. *Prog. Part. Nucl. Phys.* 32, (1994) 13–32. 10, 65
- [26] J. N. Bahcall et al. Proposed Solar Neutrino Experiment Using Ga-71. *Phys. Rev. Lett.* 40, (1978) 1351–1354. 10
- [27] T. Kirsten. STATUS REPORT ON THE PROPOSED GALLIUM SOLAR NEUTRINO EXPERIMENT. In 7th International Conference on Neutrinos, Weak Interactions and Cosmology - Neutrino 79. 1979 . 10

- [28] W. Hampel. THE GALLIUM SOLAR NEUTRINO DETECTOR. *AIP Conf. Proc.* 96, (1983) 88–95. [10](#)
- [29] B. T. Cleveland, R. Davis, and J. K. Rowley. Solar neutrino experiments and neutrino oscillators. *AIP Conf. Proc.* 72, (1981) 322–334. [10](#)
- [30] A. I. Abazov et al. Search for neutrinos from sun using the reaction Ga-71 (electron-neutrino e-) Ge-71. *Phys. Rev. Lett.* 67, (1991) 3332–3335. [10](#)
- [31] J. N. Abdurashitov et al. Measurement of the solar neutrino capture rate with gallium metal. *Phys. Rev. C* 60, (1999) 055,801. [10](#)
- [32] J. N. Abdurashitov et al. Solar neutrino flux measurements by the Soviet-American Gallium Experiment (SAGE) for half the 22 year solar cycle. *J. Exp. Theor. Phys.* 95, (2002) 181–193. [10](#)
- [33] B. Pontecorvo. Mesonium and anti-mesonium. *Sov. Phys. JETP* 6, (1957) 429. [12](#)
- [34] B. Pontecorvo. Inverse beta processes and nonconservation of lepton charge. *Zh. Eksp. Teor. Fiz.* 34, (1957) 247. [12](#)
- [35] Z. Maki, M. Nakagawa, and S. Sakata. Remarks on the unified model of elementary particles. *Prog. Theor. Phys.* 28, (1962) 870–880. [12](#)
- [36] C. W. Kim and A. Pevsner. Neutrinos in physics and astrophysics, volume 8. 1993. [12](#)
- [37] C. Giunti and C. W. Kim. Fundamentals of Neutrino Physics and Astrophysics. 2007. [12](#)
- [38] S. Weinberg. Varieties of Baryon and Lepton Nonconservation. *Phys. Rev. D* 22, (1980) 1694. [12](#)
- [39] L. Wolfenstein. Oscillations Among Three Neutrino Types and CP Violation. *Phys. Rev. D* 18, (1978) 958–960. [16](#)
- [40] F. Zwicky. Die Rotverschiebung von extragalaktischen Nebeln. *Helv. Phys. Acta* 6, (1933) 110–127. [19](#)
- [41] F. Zwicky. On the Masses of Nebulae and of Clusters of Nebulae. *Astrophys. J.* 86, (1937) 217–246. [19](#)
- [42] M. Pospelov, A. Ritz, and M. Voloshin. Secluded WIMP dark matter. *Physics Letters B* 662, (2008) 53–61. [19](#)

- [43] Q. R. Ahmad et al. Direct evidence for neutrino flavor transformation from neutral current interactions in the Sudbury Neutrino Observatory. *Phys. Rev. Lett.* 89, (2002) 011,301. [20](#)
- [44] T. Araki et al. Measurement of neutrino oscillation with KamLAND: Evidence of spectral distortion. *Phys. Rev. Lett.* 94, (2005) 081,801. [20](#)
- [45] P. Adamson et al. Measurement of the Neutrino Mass Splitting and Flavor Mixing by MINOS. *Phys. Rev. Lett.* 106, (2011) 181,801. [20](#)
- [46] H. Nunokawa, S. J. Parke, and R. Zukanovich Funchal. Another possible way to determine the neutrino mass hierarchy. *Phys. Rev. D* 72, (2005) 013,009. [20](#)
- [47] Y. Grossman. Nonstandard neutrino interactions and neutrino oscillation experiments. *Phys. Lett. B* 359, (1995) 141–147. [20](#)
- [48] P. Huber and J. W. F. Valle. Nonstandard interactions: Atmospheric versus neutrino factory experiments. *Phys. Lett. B* 523, (2001) 151–160. [20](#)
- [49] M. Blennow, T. Ohlsson, and J. Skrotzki. Effects of non-standard interactions in the MINOS experiment. *Phys. Lett. B* 660, (2008) 522–528. [20](#)
- [50] A. Palazzo and J. W. F. Valle. Confusing non-zero  $\theta_{13}$  with non-standard interactions in the solar neutrino sector. *Phys. Rev. D* 80, (2009) 091,301. [20](#)
- [51] P. Coloma, A. Donini, J. Lopez-Pavon, and H. Minakata. Non-Standard Interactions at a Neutrino Factory: Correlations and CP violation. *JHEP* 08, (2011) 036. [20](#)
- [52] A. Esmaili and A. Y. Smirnov. Probing Non-Standard Interaction of Neutrinos with IceCube and DeepCore. *JHEP* 06, (2013) 026. [20](#)
- [53] P. Adamson et al. Search for flavor-changing non-standard neutrino interactions by MINOS. *Phys. Rev. D* 88, (2013) 072,011. [20](#)
- [54] S. Choubey, A. Ghosh, T. Ohlsson, and D. Tiwari. Neutrino Physics with Non-Standard Interactions at INO. *JHEP* 12, (2015) 126. [20](#)
- [55] Q. R. Ahmad et al. Direct Evidence for Neutrino Flavor Transformation from Neutral-Current Interactions in the Sudbury Neutrino Observatory. *Phys. Rev. Lett.* 89, (2002) 011,301. [20](#)
- [56] V. D. Barger, R. J. N. Phillips, and K. Whisnant. Solar neutrino solutions with matter enhanced flavor changing neutral current scattering. *Phys. Rev. D* 44, (1991) 1629–1643. [20](#)

- [57] O. G. Miranda, M. A. Tortola, and J. W. F. Valle. Are solar neutrino oscillations robust? *JHEP* 10, (2006) 008. [20](#)
- [58] Y. Ashie et al. Measurement of atmospheric neutrino oscillation parameters by Super-Kamiokande I. *Phys. Rev. D* 71, (2005) 112,005. [20](#)
- [59] L. Wolfenstein. Neutrino Oscillations in Matter. *Phys. Rev. D* 17, (1978) 2369–2374. [21](#), [65](#)
- [60] D. S. Ayres et al. The NOvA Technical Design Report . [22](#)
- [61] P. Adamson et al. The NuMI Neutrino Beam. *Nucl. Instrum. Meth. A* 806, (2016) 279–306. [23](#)
- [62] R. M. Zwaska. Accelerator Systems and Instrumentation for the NuMI Neutrino Beam. Ph.D. thesis, Texas U. 2005. [23](#)
- [63] B. Behera. Measurement of the Double Differential Inclusive Muon Neutrino Charged-current Cross-section in the NOvA Near Detector. Ph.D. thesis, Indian Inst. Tech., Hyderabad 2018. [26](#)
- [64] S. Agostinelli et al. GEANT4—a simulation toolkit. *Nucl. Instrum. Meth. A* 506, (2003) 250–303. [33](#), [35](#)
- [65] L. Aliaga et al. Neutrino Flux Predictions for the NuMI Beam. *Phys. Rev. D* 94, (2016) 092,005. [Addendum: *Phys.Rev.D* 95, 039903 (2017)]. [34](#)
- [66] T. M. Lackey. Proton Scattering in NOvA Test Beam. Ph.D. thesis, Indiana U. 2022. [34](#)
- [67] C. Andreopoulos et al. The GENIE Neutrino Monte Carlo Generator. *Nucl. Instrum. Meth. A* 614, (2010) 87–104. [35](#)
- [68] L. A. Fernandes and M. M. Oliveira. Real-time line detection through an improved Hough transform voting scheme. *Pattern Recognition* 41, (2008) 299–314. [36](#)
- [69] N. Arkani-Hamed, D. P. Finkbeiner, T. R. Slatyer, and N. Weiner. A theory of dark matter. *Phys. Rev. D* 79, (2009) 015,014. [39](#)
- [70] E. Izaguirre, G. Krnjaic, P. Schuster, and N. Toro. Analyzing the discovery potential for light dark matter. *Physical Review Letters* 115, (2015) 251,301. [39](#), [41](#)
- [71] N. Arkani-Hamed, D. P. Finkbeiner, T. R. Slatyer, and N. Weiner. A theory of dark matter. *Physical Review D* 79, (2009) 015,014. [39](#)

- [72] J. Lees, V. Poireau, V. Tisserand, E. Grauges, A. Palano, G. Eigen, D. N. Brown, M. Derdzinski, A. Giuffrida, Y. G. Kolomensky et al. Search for invisible decays of a dark photon produced in  $e^+ e^-$  collisions at BaBar. *Physical review letters* 119, (2017) 131,804. [39](#), [63](#), [94](#)
- [73] P. D. Serpico and G. G. Raffelt. MeV-mass dark matter and primordial nucleosynthesis. *Physical Review D* 70, (2004) 043,526. [39](#)
- [74] M. Battaglieri et al. U.S. Cosmic Visions: New Ideas in Dark Matter 2017: Community Report. *arXiv: 1707.04591* . [39](#)
- [75] P. deNiverville and C. Frugiuele. Hunting sub-GeV dark matter with the NO $\nu$ A near detector. *Phys. Rev. D* 99, (2019) 051,701. [39](#)
- [76] P. deNiverville and C. Frugiuele. Hunting sub-GeV dark matter with the NO  $\nu$  A near detector. *Physical Review D* 99, (2019) 051,701. [39](#)
- [77] B. Batell, M. Pospelov, and A. Ritz. Exploring portals to a hidden sector through fixed targets. *Physical Review D* 80, (2009) 095,024. [39](#)
- [78] P. Coloma, B. A. Dobrescu, C. Frugiuele, and R. Harnik. Dark matter beams at LBNF. *Journal of High Energy Physics* 2016, (2016) 1–20. [39](#), [41](#)
- [79] B. A. Dobrescu and C. Frugiuele. GeV-scale dark matter: production at the Main Injector. *Journal of High Energy Physics* 2015, (2015) 1–19. [39](#), [41](#)
- [80] H. Davoudiasl and W. J. Marciano. Running of the U (1) coupling in the dark sector. *Physical Review D* 92, (2015) 035,008. [40](#), [41](#)
- [81] M. Battaglieri, A. Belloni, A. Chou, P. Cushman, B. Echenard, R. Essig, J. Estrada, J. L. Feng, B. Flaugher, P. J. Fox et al. US cosmic visions: new ideas in dark matter 2017: community report. *arXiv preprint arXiv:1707.04591* . [41](#)
- [82] J. A. Formaggio and G. P. Zeller. From eV to EeV: Neutrino cross sections across energy scales. *Reviews of Modern Physics* 84, (2012) 1307. [42](#)
- [83] L. Lyons. Raster scan or 2-D approach? *arXiv preprint arXiv:1404.7395* . [44](#)
- [84] P. deNiverville, C.-Y. Chen, M. Pospelov, and A. Ritz. Light dark matter in neutrino beams: production modelling and scattering signatures at MiniBooNE, T2K and SHiP. *Phys. Rev. D* 95, (2017) 035,006. [45](#), [93](#)
- [85] A. Aurisano, C. Backhouse, R. Hatcher, N. Mayer, J. Musser, R. Patterson, R. Schroeter, and A. Sousa. The NO $\nu$ A simulation chain. In *Journal of Physics: Conference Series*, volume 664. IOP Publishing, 2015 072002. [47](#)

- [86] B. Brahma, W. Mu, A. Himmel, and A. Giri. Light Dark Matter Analysis Using NO $\nu$ A Near Detector. *PoS EPS-HEP2023*, (2024) 138. [62](#)
- [87] L. Auerbach, R. Burman, D. Caldwell, E. Church, J. Donahue, A. Fazely, G. Garvey, R. Gunasingha, R. Imlay, W. Louis et al. Measurement of electron-neutrino electron elastic scattering. *Physical Review D* 63, (2001) 112,001. [63](#), [94](#)
- [88] P. DeNiverville, M. Pospelov, and A. Ritz. Observing a light dark matter beam with neutrino experiments. *Physical Review D* 84, (2011) 075,020. [63](#), [94](#)
- [89] B. Batell, R. Essig, and Z. Surujon. Strong constraints on sub-GeV dark sectors from SLAC beam dump E137. *Physical Review Letters* 113, (2014) 171,802. [63](#), [94](#)
- [90] D. Banerjee, V. Burtsev, A. Chumakov, D. Cooke, P. Crivelli, E. Depero, A. Dermenev, S. Donskov, R. Dusaev, T. Enik et al. Dark matter search in missing energy events with NA64. *Physical review letters* 123, (2019) 121,801. [63](#), [94](#)
- [91] A. Aguilar-Arevalo, M. Backfish, A. Bashyal, B. Batell, B. Brown, R. Carr, A. Chatterjee, R. Cooper, P. Deniverville, R. Dharmapalan et al. Dark matter search in a proton beam dump with MiniBooNE. *Physical Review Letters* 118, (2017) 221,803. [63](#), [94](#)
- [92] D. Akimov, P. An, C. Awe, P. Barbeau, B. Becker, V. Belov, I. Bernardi, M. Blackston, C. Bock, A. Bolozdynya et al. First probe of sub-GeV dark matter beyond the cosmological expectation with the COHERENT CsI detector at the SNS. *Physical Review Letters* 130, (2023) 051,803. [63](#), [94](#)
- [93] M. C. Gonzalez-Garcia, M. M. Guzzo, P. I. Krastev, H. Nunokawa, O. L. G. Peres, V. Pleitez, J. W. F. Valle, and R. Zukanovich Funchal. Atmospheric neutrino observations and flavor changing interactions. *Phys. Rev. Lett.* 82, (1999) 3202–3205. [65](#)
- [94] A. Friedland and C. Lunardini. A Test of tau neutrino interactions with atmospheric neutrinos and K2K. *Phys. Rev. D* 72, (2005) 053,009. [65](#)
- [95] R. N. Mohapatra and G. Senjanovic. Neutrino Mass and Spontaneous Parity Non-conservation. *Phys. Rev. Lett.* 44, (1980) 912. [65](#)
- [96] G. L. Fogli and E. Lisi. Tests of three flavor mixing in long baseline neutrino oscillation experiments. *Phys. Rev. D* 54, (1996) 3667–3670. [65](#)
- [97] H. Minakata and H. Nunokawa. Exploring neutrino mixing with low-energy superbeams. *JHEP* 10, (2001) 001. [65](#)

- [98] F. Capozzi, G. L. Fogli, E. Lisi, A. Marrone, D. Montanino, and A. Palazzo. Status of three-neutrino oscillation parameters, circa 2013. *Phys. Rev. D* 89, (2014) 093,018. [65](#)
- [99] D. V. Forero, M. Tortola, and J. W. F. Valle. Neutrino oscillations refitted. *Phys. Rev. D* 90, (2014) 093,006. [65](#)
- [100] I. Esteban, M. C. Gonzalez-Garcia, M. Maltoni, T. Schwetz, and A. Zhou. The fate of hints: updated global analysis of three-flavor neutrino oscillations. *JHEP* 09, (2020) 178. [65](#)
- [101] K. S. Babu, P. S. Dev, S. Jana, and Y. Sui. Zee-Burst: A New Probe of Neutrino Nonstandard Interactions at IceCube. *Phys. Rev. Lett.* 124, (2020) 041,805. [65](#)
- [102] P. S. Bhupal Dev et al. Neutrino Non-Standard Interactions: A Status Report. *SciPost Phys. Proc.* 2, (2019) 001. [65](#)
- [103] T. Ohlsson. Status of non-standard neutrino interactions. *Rept. Prog. Phys.* 76, (2013) 044,201. [65](#)
- [104] Y. Farzan and M. Tortola. Neutrino oscillations and Non-Standard Interactions. *Front. in Phys.* 6, (2018) 10. [65](#)
- [105] M. Masud and P. Mehta. Nonstandard interactions spoiling the CP violation sensitivity at DUNE and other long baseline experiments. *Phys. Rev. D* 94, (2016) 013,014. [65](#)
- [106] P. B. Denton, A. Giarnetti, and D. Meloni. How to identify different new neutrino oscillation physics scenarios at DUNE. *JHEP* 02, (2023) 210. [65](#)
- [107] Y. Farzan and I. M. Shoemaker. Lepton Flavor Violating Non-Standard Interactions via Light Mediators. *JHEP* 07, (2016) 033. [65](#)
- [108] A. Himmel. New Oscillation Results from the NO $\nu$ A Experiment (2020). Neutrino 2020. [66](#)
- [109] M. A. Acero et al. Improved measurement of neutrino oscillation parameters by the NO $\nu$ A experiment. *Phys. Rev. D* 106, (2022) 032,004. [66](#)
- [110] P. Dunne. Latest Neutrino Oscillation Results from T2K (2020). Neutrino 2020. [66](#)
- [111] K. Abe et al. Improved constraints on neutrino mixing from the T2K experiment with  $3.13 \times 10^{21}$  protons on target. *Phys. Rev. D* 103, (2021) 112,008. [66](#)
- [112] S. S. Chatterjee and A. Palazzo. Nonstandard Neutrino Interactions as a Solution to the NO $\nu$ A and T2K Discrepancy. *Phys. Rev. Lett.* 126, (2021) 051,802. [66](#)

- [113] P. B. Denton, J. Gehrlein, and R. Pestes. *CP* -Violating Neutrino Nonstandard Interactions in Long-Baseline-Accelerator Data. *Phys. Rev. Lett.* 126, (2021) 051,801. 66
- [114] J. Liao, D. Marfatia, and K. Whisnant. Degeneracies in long-baseline neutrino experiments from nonstandard interactions. *Phys. Rev. D* 93, (2016) 093,016. 68, 80
- [115] GLoBES. GLoBES Software 2005. <https://www.mpi-hd.mpg.de/personalhomes/globes/experiments.html>. 68
- [116] NuFIT v5.2, Three-neutrino fit based on data available in November 2022. <http://www.nufit.org/>. 68, 81
- [117] P. A. Zyla et al. Review of Particle Physics. *PTEP* 2020, (2020) 083C01. 68
- [118] B. Brahma and A. Giri. Exploring non standard interactions effects in T2HK and DUNE. *Eur. Phys. J. C* 82, (2022) 1145. 69
- [119] V. D. Barger, K. Whisnant, and R. J. N. Phillips. *CP* Nonconservation in Three-Neutrino Oscillations. *Phys. Rev. Lett.* 45, (1980) 2084. 75
- [120] J. Arafune and J. Sato. *CP* and *T* violation test in neutrino oscillation. *Phys. Rev. D* 55, (1997) 1653–1658. 75
- [121] A. Donini, M. B. Gavela, P. Hernandez, and S. Rigolin. Neutrino mixing and *CP* violation. *Nucl. Phys. B* 574, (2000) 23–42. 75
- [122] H. Nunokawa, S. J. Parke, and J. W. F. Valle. *CP* Violation and Neutrino Oscillations. *Prog. Part. Nucl. Phys.* 60, (2008) 338–402. 75
- [123] D. Meloni, T. Ohlsson, and H. Zhang. Exact and Approximate Formulas for Neutrino Mixing and Oscillations with Non-Standard Interactions. *JHEP* 04, (2009) 033. 75, 80
- [124] T. Kikuchi, H. Minakata, and S. Uchinami. Perturbation Theory of Neutrino Oscillation with Nonstandard Neutrino Interactions. *JHEP* 03, (2009) 114. 80
- [125] J. Kopp, M. Lindner, T. Ota, and J. Sato. Non-standard neutrino interactions in reactor and superbeam experiments. *Phys. Rev. D* 77, (2008) 013,007. 80
- [126] B. Brahma and A. Giri. Discernible NSI Effects in Long-Baseline Neutrino Experiments . 80
- [127] B. Brahma and A. Giri. Probing Dual NSI and *CP* Violation in DUNE and T2HK . 80